Università degli Studi di Ferrara

DOCTORAL COURSE IN

"Physics"

CYCLE 34

COORDINATOR Prof. Eleonora Luppi

DEVELOPMENT OF A FLOATING SENSOR TO MEASURE THE LIGHT SPECTRAL DISTRIBUTION WITHIN A MICROALGAL PHOTOBIOREACTOR

Scientific/Disciplinary Sector (SDS) FIS/01

Candidate

Dott. Gjestila Marinela

_____

(signature)

Supervisor

Prof. Vincenzi Donato

_____

(signature)

Year 2018/2022

Abstract (*English*)

Light is an essential parameter for the growth of photosynthetic microorganisms. For this reason, information on the light spectrum and light intensity distribution within a photobioreactor (PBR) are helpful to develop highly automated growth methods.

In this work, we designed a floating optical sensor to measure the spectral light intensity at different points within the PBR. In addition, the sensor is equipped with a localization algorithm so that a light intensity distribution map within the PBR can be plotted.

Moreover, a model is proposed to simulate the spectral distribution of light inside a photobioreactor with a ray trace software for different wavelengths within the photosynthetically active radiation (PAR) spectrum. The method was designed to obtain quickly and reproducible light distribution simulations within the photobioreactor faster than the other methods proposed in the literature, bypassing the need to determine the radiative properties of the algal cells. This model has been used to assess the accuracy of the optical sensor measurements within the PBR.

Abstract (*Italiano*)

La luce è un parametro importante per la crescita dei microrganismi fotosintetici. Per questo motivo, le informazioni sullo spettro della luce e sulla distribuzione dell'intensità della luce all'interno di un fotobioreattore (PBR) sono utili per sviluppare metodi di crescita altamente automatizzati.

In questo lavoro abbiamo progettato un sensore ottico flottante per misurare l'intensità della luce spettrale in diversi punti all'interno del PBR. Il sensore è dotato di un algoritmo di localizzazione, in modo da poter tracciare una mappa della distribuzione dell'intensità luminosa all'interno del PBR.

Inoltre, viene proposto un modello per simulare con un ray-tracing software la distribuzione spettrale della luce all'interno di un fotobioreattore per diverse lunghezze d'onda all'interno dello spettro della radiazione fotosinteticamente attiva (PAR). Il metodo è stato progettato per ottenere simulazioni di distribuzione della luce facilmente e riproducibili all'interno del fotobioreattore più velocemente rispetto agli altri metodi proposti in letteratura, aggirando la necessità di determinare le proprietà radiative delle cellule algali. Questo modello è stato utilizzato per valutare l'accuratezza delle misurazioni del sensore ottico all'interno del PBR

Contents

List of Figures

Chapter 1

Introduction

1.1 Introduction

As reported by the International Energy Agency, Global Energy Consumption continues to show high growth rates year after year. In their major part, the energy demands are still satisfied by fossil fuels: 86% of the energy consumed worldwide and almost 100% of the energy used in transportation is being produced by fossil fuels. This has led to increased CO_2 and other greenhouse gas emissions in the atmosphere, which has triggered global climate change [1–7].

Some of the most significant energy sources capable of replacing fossil fuels are solar, wind, water energy, and biofuels [4,6,7]. The production and use of biofuels in transportation are considered a solution to the cause-effect problem discussed in the first paragraph.

Based on the origin of production, biofuels can be classified into four generations.

First-generation biofuels include the fuels extracted from edible crops like starch, wheat, corn, soybean, animal oil, etc. However, the first generation of biofuels showed a negative effect on food security in the environment due to the use of fertilizers, and it requires big surfaces of cultivable land for feedstock generation.

The second generation of biofuels is obtained from several trees, grass, bushes, agricultural residues, etc. Unlike the first generation, the second generation of biofuels is produced from non-edible oils and doesn't compete with food. On the other hand, to grow the feedstock for this generation of biofuels is still needed cultivable land or forests. One major concern related to their production is deforestation.

Meanwhile, microalgal species are used as feedstock for the third generation of biofuels. Biofuels produced from the microalgae are considered a possible alternative to fossil fuels due to the advantages it has concerning the other generations: no arable land is

needed; it doesn't have a negative impact on food security; brackish and saline water can be used for their cultivation; feedstock can be grown in rough conditions.
Moreover, genetically modifying the microalgae can produce a new generation of biofuels, which is called the fourth generation of biofuels [8–11].

Despite the effort made to industrialize the cultivation and harvesting of the microalgal biomass, their large-scale cultivation is still restrained. As a result, biofuel production costs are still not competitive with conventional fuels [12,13]. To reduce the costs of biofuel production, a synergic effort must be spent to research the conditions that can enhance algal productivity, discover and test new extraction methods, and simultaneously, strong investments need to be made by companies to develop highly automated growth and harvesting methods.

Presently, the research on microalgae is focused on the design, optimization, and scale-up of algal PBRs to increase their overall productivity [14–16]. The parameters that can be optimized are light transport and distribution, gas exchange, medium supply, and temperature [17]. Among these parameters, light intensity and light spectrum have a crucial effect on the algal growth rate [14,18–25].

The online monitoring of the spectral light distribution within the algal suspension is a key factor in ensuring microalgae growth stability in photobioreactors [26,27].

This study's objective was to develop a floating light sensor (FloSen) to monitor, in real-time, the spectral light intensity and the turbidity within an algal PBR.
We designed a sensor that can float freely within the algal suspension providing real-time information on the spectral irradiance, turbidity, and the 3D position where the measurement was taken. The localization of the sensor is based on the measurement, with an embedded magnetic sensor, of a non-uniform magnetic field generated by a set of anchor coils attached to the PBR in specific positions along its height.

The first prototype of the floating sensor has a cylindrical shape with a height of 36 mm and a diameter of 24 mm. It is equipped with four optical sensors measuring light intensity in four bands of the light spectrum: red, green, blue, and infrared. Moreover, the sensor is also equipped with a Bluetooth module providing point-to-point communication with a PC supervisor. The wireless communication protocol allows the remote measurement of light intensity while the sensor is floating inside the algal suspension. The sensor is also provided with a Li-ion battery recharged without using any external connections by a small array of solar cells embedded on the printed circuit board of the sensor.
The calibration of the sensor was done by measuring the transmitted light intensity by an algal suspension of *Nannochloropsis Oculata* during its growth phase (0.21 g/l to 1.26 g/l).

Meanwhile, to test the sensor, we developed a model that calculates light's spectral distribution at different points within the photobioreactor.

To model the light propagation within an algal suspension, many researchers have used analytic expressions like Lambert-Beer law [17–20] or Cornet's model [28,29]. However, a more accurate approach followed by researchers to deal with this problem has been to use the Radiative Transfer Equation (RTE) for a non-emitting medium.

$$\left(\frac{dI_\lambda(\hat{\boldsymbol{s}})}{ds}\right) = -\kappa_\lambda I_\lambda(\hat{\boldsymbol{s}}) - \sigma_{s\lambda} I_\lambda(\hat{\boldsymbol{s}}) + \frac{\sigma_{s\lambda}}{4\pi}\int_{4\pi} I_\lambda(\hat{\boldsymbol{s}_i})\,\phi_\lambda(\hat{\boldsymbol{s}_i}, \hat{\boldsymbol{s}})\,d\Omega_i \qquad 1\text{-}1$$

Where I_λ is the spectral irradiance expressed in $\frac{W}{m^2\,nm\,sr}$, $\kappa_\lambda\ (m^{-1})$ is the spectral absorption coefficient, $\sigma_{s\lambda}\ (m^{-1})$ is the spectral scattering coefficient, $\hat{\boldsymbol{s}}$ is the direction of propagation, $\phi_\lambda\left(\hat{\boldsymbol{s}_i}, \hat{\boldsymbol{s}}\right)$ represents the scattering phase function, i.e., the probability that a ray is scattered from the direction $\hat{\boldsymbol{s}_i}$ in direction $\hat{\boldsymbol{s}}$, and $d\Omega_i$ is the solid angle around the direction $\hat{\boldsymbol{s}_i}$ [30]. The RTE parameters depend on the microalgae species and can be determined experimentally [31–34] or theoretically [35–37]. For instance, [33] have developed an experimental method that consists in performing normal-normal and normal-hemispherical transmittance measurements to determine, respectively, the extinction coefficient β_λ, the absorption coefficient k_λ, and nephelometric measurements to retrieve the phase function. Meanwhile, the theoretical method is based on the Lorentz-Mie theory [38]. However, in the models based on the theoretical method, typically, the microalgae cells are considered to be homogeneous with some effective complex index of refraction [31], and their shapes are approximated as volume-equivalent spheres [28], coated spheres [39] or even infinitely long cylinders.

The research results on the microalgae's radiative properties are eventually used to solve the RTE equation. So far, different numerical methods have been exploited to solve the Radiative Transfer Equation (RTE) [40–46]. For example, Pottier et al. [36] apply the two-flux method to solve the RTE for a torus shape photobioreactor after theoretically calculating the radiative characteristics of *Chlamydomonas reinhardtii* microorganisms. Diversely, [44] implements the discrete ordinate finite volume technique.

We developed a new experimental method to simulate the spectral distribution of light within a turbid medium, bypassing the two-step procedure: cell radiative properties calculation and RTE solution, carried out by a significant part of researchers until now.

We conducted several experiments to measure the scattered light from the microalgal suspension within different solid angles at different concentrations and wavelengths. We

wanted to fit the experimental data with a scattering phase function available in different ray trace software to facilitate the reproduction of the method. Based on the literature, it was chosen the *Henyey-Greenstein* (HG) phase function [34,47–49].

Thanks to the method developed, we found the HG parameters of the bulk scattering model provided by **Zemax OpticStudio** software for different concentrations at six wavelengths within the photosynthetically active radiation (PAR) region: 401 nm, 456.7 nm, 523 nm, 543.5 nm, 632.8 nm, and 675.7 nm for a *Nannochloropsis oculata* suspension. This set of HG functions was easily implemented on **Zemax OpticStudio** software to calculate the spectral distribution of light inside the volume of a column internally illuminated PBR. The simulation results were further used to validate the functioning of the floating sensor FloSen.

1.2 Aims and objectives

This study focused on developing a sensor to monitor in real-time the spectral distribution of light within an annular photobioreactor used for algal cultivation. The sensor was designed to float freely within the algal suspension. In addition, a localization method was developed based on the non-uniform magnetic field generated by sequential coils placed along the PBR height.

To test the functioning of the sensor, we needed to have data about the spectral distribution of light within the PBR. Eventually, utilizing the ray trace software **Zemax OpticStudio**, we developed a model to calculate the spectral distribution of light at different points of the PBR. In the context of this model, several optical measurements have been carried out for different samples of algal suspensions. Moreover, experimental measurements and data analysis have also been done during the sensor test.

1.3 Outline of the thesis

Chapter 1 introduces the context of the work and gives a full view of the study.
Chapter 2 reviews the properties of the microalgae species, the photosynthesis process, and the light interaction with algae. The Radiative Transfer Equation, which is derived in the general case and in the specific case for an algal suspension, is in the focus of this chapter. Further, in this chapter, different approximated methods to solve the RTE are discussed, and also the methods used so far to solve it for an algal suspension are studied. Finally, a short overview of the cultivation methods of the microalgae is given at the end of the chapter.

Chapter 3 describes two PBRs developed during the thesis period and the LabView software used to adjust the light intensity.

The model developed to calculate the spectral distribution of light within an algal suspension is explained in Chapter 4. This model is applied to the PBRs described in Chapter 3. Further, also the results of the simulations are discussed.

The block diagram, the circuit, and the floating sensor software are described in Chapter 5. This chapter also presents the localization algorithm.

Chapter 6 contains the experimental part of the thesis: the experimental measurements and the tests of the sensor.

The main results of the research are summarized in Chapter 7.

Chapter 2

Radiative Transfer Equation

Currently, 86 % of the global energy produced in a year comes from the combustion of fossil fuels. Due to the direct carbon combustion for energy are generated more than 24 gigatons of CO_2 annually, resulting in an increase in the atmospheric CO_2 concentration from 300 ppm to 380 ppm over the last 100 years. This has triggered a global climate change and has contributed to biological extinctions [2–5,50–52]. The solution to this problem can be using alternative energy sources like solar, water, wind energy, and biofuels. Based on production, there exist four generations of biofuels: the first generation of biofuels is produced from edible crops, the second generation of biofuels is produced from non-edible crops, the third generation of biofuels is produced from microalgae biomass, the fourth generation of biofuels is made from genetically modified microalgae [8–11]. *Photobioreactors (PBRs) are systems used to grow microalgae by controlling their life parameters: salinity, temperature, CO_2, light, and pH. Many studies claim that the* ***radiative light transfer*** *inside the PBR is of paramount importance as it can be used to determine the kinetic rates, energetic yield, biomass composition, and pigment contents* [29,37,53–57]. *As a result, the study and the radiative transfer equation's solution within the PBR are required. This equation is characterized by three parameters: the absorption and scattering cross-section and the phase function. Therefore, any radiative analysis of a photobioreactor starts with determining these three parameters* [58].

2.1 Microalgae

Microalgae are prokaryotic or eukaryotic oxygen-evolving photosynthetic autotrophs that can live in harsh conditions due to their unicellular or simple multicellular structure [59–61]. They are found worldwide, mainly in waters, but they can also be found on all types of soils [62]. Even though only 30000 species have been studied, it is estimated that more than 50000 microalgae species exist on Earth [60,61].

Microalgae species are essential for Earth's ecosystem as they produce nearly half of the atmospheric oxygen via the photosynthesis process, playing a prominent role in the global carbon cycle [60–63]. Moreover, lately, a great interest has risen in using the microalgae feedstock to produce third-generation biofuels. Many research reports and articles describe the advantages of the third generation of biofuels with respect to the other generations. Indeed, the production of microalgae doesn't require arable land, microalgae-based biofuel doesn't compete with food, and it is estimated that microalgae produce two to tenfold more biomass per unit land area than the best terrestrial systems. It is reported that microalgae have higher photosynthetic efficiency than other plants due to their greater ability to capture light and convert it to chemical energy. [13,50,60,64–76].

2.1.1 The ultrastructure of microalgae

The microalgae cell comprises several organelles of different sizes and shapes embedded in the cytosol: chloroplasts (eucaryotic cells), nucleus, nucleolus, mitochondria (eucaryotic cells), lipid vesicles, gas or fluid-filled vacuoles, and pyrenoids. A complex cell wall and the cell membrane, which have different characteristics for eucaryotic and procaryotic cells, surround the cell content.

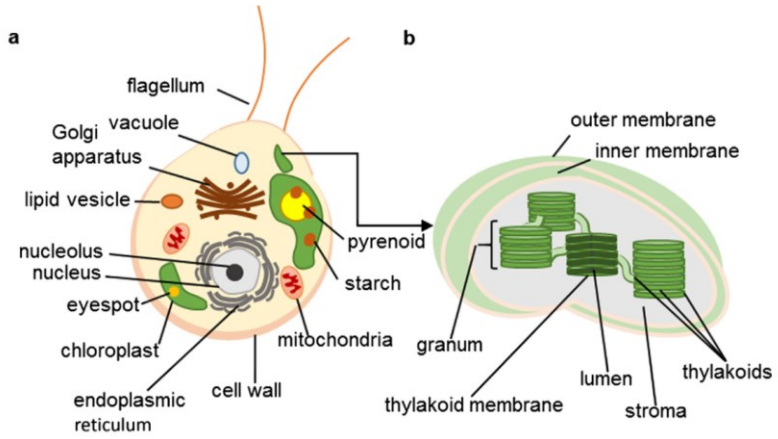

Figure 2-1: *Sketch of an algal ultrastructure (a) and of the chloroplast (b) for an eucaryotic cell [61]*

In the case of procaryotic cells, thylakoids lie free in the cytoplasm and contain the photosynthetic organism. They appear as flattened sacs and may be arranged in concentric rings, in parallel bundles, dispersed, etc. In eucaryotic cells, the thylakoids are placed in the chloroplast and contain the chlorophylls and a surrounding matrix called stroma [61,62].

Moreover, additional compartments could be developed as metabolites microalgae can synthesize such lipid and starch bodies during nitrogen starvation [77,78].

How will light interact with the microalgae cells? When light rays hit a microalgae cell, they will partly get scattered and partially absorbed. The ray lights' energy that gets absorbed is partly used for the photosynthesis process. The rest of the energy is dissipated either in the form of heat or by fluorescence. Meanwhile, the energy used during the photosynthesis process is converted into biochemical energy used for respiration, growth, and other metabolic processes (Figure 2-2). The following sections will discuss the physics behind these interaction phenomena in general and specifically for microalgae cells.

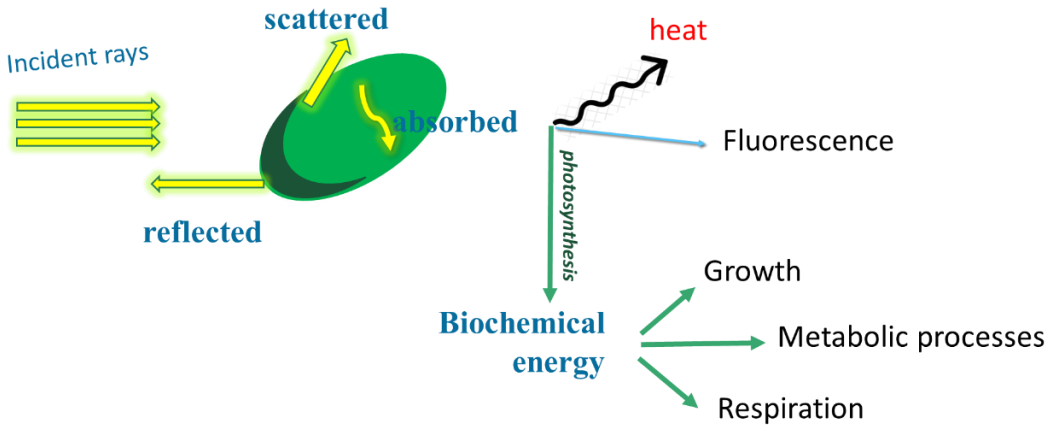

Figure 2-2: *Light interaction with the microalgae cell*

2.1.2 The oxygenic photosynthesis

Life on Earth is entirely dependent on the photosynthesis process. Photosynthesis is a photo-biochemical process that transforms light energy into chemical energy. Oxygenic photosynthesis is the form of photosynthesis that produces molecular oxygen from the oxidation of water [79,80]. This form of photosynthesis is carried out by microalgae and cyanobacteria [79]. The reaction of oxygenic photosynthesis in microalgae occurs within the chloroplast (Figure 2-1). Two types of reactions occur during photosynthesis: light reactions and dark reactions. The light reactions, which consist of converting light energy into chemical bonds, occur in the thylakoid membrane. In specific, during these reactions the energy of the photons absorbed from the pigments is used from the photosystems for the reduction of the NADP+ to NADPH and the phosphorylation of the ADP. NADPH and ATP are then utilized during dark reactions, consisting of CO_2 fixation. The stroma is the place where the dark reaction occurs [81].

2.1.3 Absorption of light from the pigments

There are three types of pigments: *chlorophylls* (Chls), *carotenoids* (Cars), and *phycobilins*. The most common chlorophylls are *Chl a*, *Chl b*, and *Chl c*. Carotenoids can be β – *carotene*, *fucoxanthin,* and *peridinin.* Finally, the most common *phycobilins* are *phycoerythrobilin*, *phycocyanobilin,* and *allophycocyanin* [82]. The relative pigment composition of the microalgal species depends on different environmental parameters such as temperature, quantity and quality of light, photoperiods, pH, nutrient limitation, nitrogen supplements, salinity, pesticides, and heavy metal stress. Light intensity plays an essential role in controlling chlorophyll (Chls) and β – *carotene* accumulation in algal cells. There is an inverse relationship between the Chls content and light intensity; on the other hand, the β – *carotene* content per cell increases with light intensity [83].

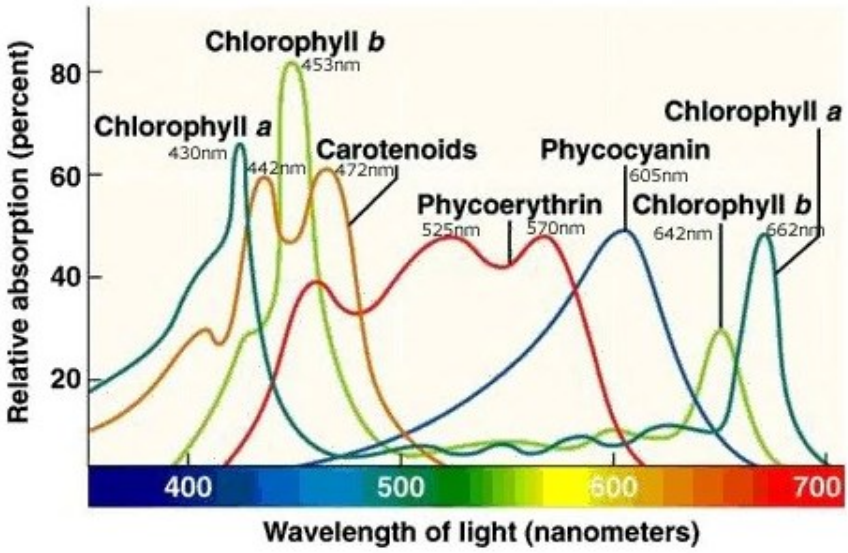

Figure 2-3: *Relative absorption curve as a function of wavelength for different types of pigments [84].*

Pigments are crucial elements in photosynthesis. The first step in photosynthesis is the absorption of light by pigments. A photon with sufficient energy will excite the chlorophyll molecule during this process, going from the ground state to the excited state.

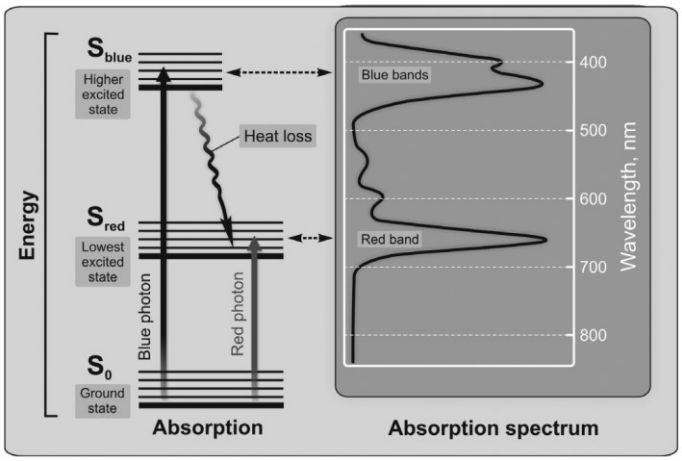

Figure 2-4*: A Jablonski-Perrin diagram of the energy levels in a Chl a molecule and the absorption spectrum corresponding to these levels [79]*

Figure 2-4 shows the Jablonski – Perrin diagram of the energy levels in *Chl a*. There are three electronic states: the ground state, the first excited state, and the second excited state. Each electronic state is composed of several substates corresponding to molecular

vibrational and rotational energy. It can be deduced that blue photons will take the molecule to the nth excited state while red photons will take it to its first excited state. The highest excited state is very unstable, and the molecule will soon pass to the first excited state. The critical fact is that no matter the energy of the absorbed photon, the photochemical process starts from the lowest exited state [79,81]. De Mooji et al. [155] reports no essential difference in the absorption cross-section of the microalgae grown under different light colors. On the other hand, as mentioned above, the pigments on the microalgae depend on the perceived light intensity. So the pigment content correlates to the biomass-specific light absorption rate.

The absorbed energy from the pigments is funneled then into *chlorophyll a* molecule, in the reaction center (RC) of the two photosynthetic units: photosystem I (PSI) and photosystem II (PSII) [79,85]. In the reaction center of PSII, two *chl a* molecules form a dimer called P680 with an absorption peak at 680 nm. In the same way, a dimer is formed in the PSI reaction center but with an absorption peak at 700 nm [61]. After trapping the excitation energy by special photoactive Chl molecules in the RCs of these two photosystems, light energy is converted into chemical energy due to the Linear and Cyclic Electron Transfer (LET and CET, respectively).

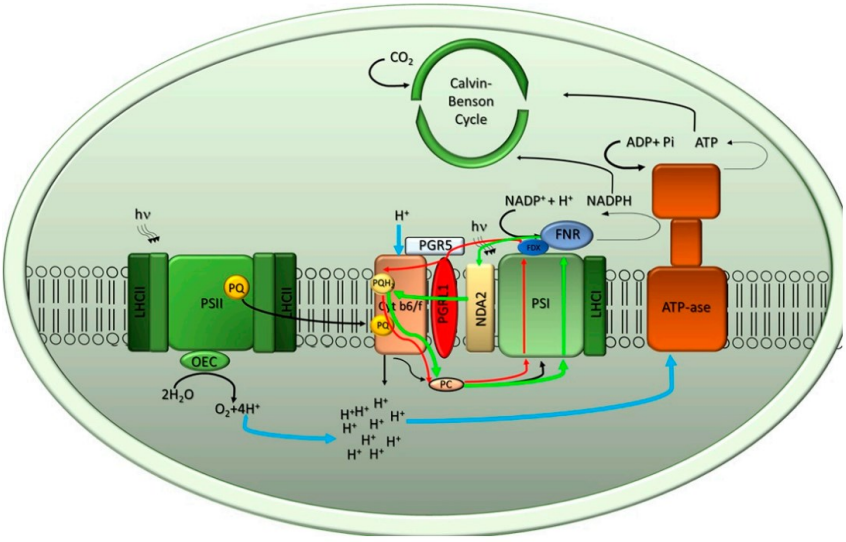

Figure 2-5: *Schematic representation of photosynthetic electron transport [86] .*

The first step in the LET reaction is water–splitting from the PSII, which captures the photon and utilizes excitation energy to oxidize water molecules into protons and molecular oxygen O2. The electrons removed from the oxidation of water molecules are transported via

Plastoquinone (PQ) pool (see ***Figure 2-5***) to the Cytochrome b6f complex. Then they are used to translocate protons across the thylakoid membrane. On the other hand, the reaction center P700 will be oxidized due to the absorption of photons by PSI. As a result, electrons from PC (plastocyanin) fill the electron-hole $P700^{+}$. The electrons removed by the oxidation reduce ferredoxin (FDX). At the same time, on the stromal side, the $NADP^{+}$ reductase transfers the electron from FDX to $NADP^{+}$ to form NADPH. Due to the electron transport, a proton gradient is built up across the thylakoid membrane [86,87].

2.1.4 Fluorescence

Nearly 100% of the excitation energy absorbed by a light-harvesting pigment, rather than *Chl a*, is transferred to *Chl a*. The energy transferred to *Chl a* or absorbed directly by *Chl a* may be: i) dissipated as heat, ii) used for re-emission of a red photon, or iii) sent to PSII for the process of photosynthesis. The photon re-emission process due to the transition of the *Chl a* from the first excited state to the ground state is called fluorescence [61,81]. Fluorescence, heat, and photosynthesis are complementary processes. As a result, by measuring the fluorescence, one could retrieve photosynthesis and heat dissipation information [88]. As stated before, fluorescence occurs due mainly to the de-excitation of the molecule from the first excited state to the ground state because the energy of the molecule in the second excited state will be dissipated through internal conversion and vibrational relaxation in heat. As a result, the fluorescence spectrum of the *Chl a* doesn't depend on the incident spectrum. But on the other hand, the strength of the fluorescence signal depends on the excitation spectrum [61].

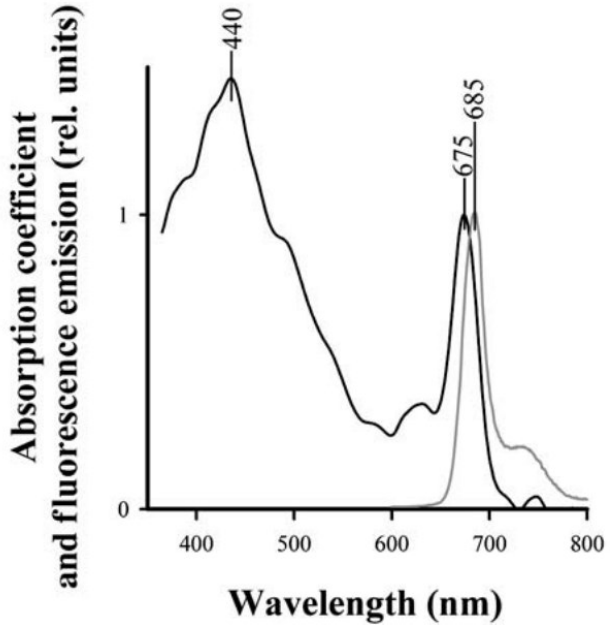

Figure 2-6: *In vivo absorption spectrum (black line) and fluorescence emission spectrum (grey line) for the diatom Thalassiosira pseudonana [81].*

2.2 Light interaction with particles

When interacting with a medium containing small particles, light intensity distribution may change due to absorption and/or scattering. The interaction of the electromagnetic wave with the particle will depend on:

a) The shape of the particle
b) The complex index of refraction of the particle's material
c) The relative size of the particle concerning the wavelength of the EM, $x = \frac{2\pi a}{\lambda}$, where a is the diameter of the particle
d) The clearance between particles

The complex refractive index m of a medium is called the ratio between the light phase velocity in vacuum and its velocity in that medium:

$$m = n + ik, \qquad 2\text{-}1$$

where n characterizes the effect of the medium on the phase and k on the amplitude of the electromagnetic wave.

The absorption coefficient is related to the imaginary part of the refractive index:

$$\sigma_a = \frac{4\pi}{\lambda} k \qquad 2\text{-}2$$

where λ is the wavelength of the wave in vacuum [30,89,90].

For the first time, the interaction of light with single particles was studied by Lord Rayleigh. His solution was obtained for particles of spherical shape with a diameter much smaller than the wavelength of the electromagnetic wave (EM) [30,91,92]. Meanwhile, the Lorenz-Mie theory describes the interaction of the electromagnetic wave with a spherical particle that is too large to apply the Rayleigh theory but too small to employ geometric optics. A detailed derivation of this theory can be found in the books of Bohren and Huffman [93], van de Hulst [94], and Kerker [79]. In this thesis, some equations derived by Mie starting from Maxwell's equations will be given to give a general hint of the work that was done in this field.

The absorption and scattering of light by a particle are characterized by absorption cross-section C_{abs} and scattering cross-section C_{sca}, respectively. The sum of these two quantities is called the extinction cross-section:

$$C_{ext} = C_{abs} + C_{sca} \qquad 2\text{-}3$$

The absorption, scattering, and extinction cross-section have the dimensions of the area, and generally, they are functions of the particle's orientation and of the polarization state of the incident light. Often, they are nondimensionalized with the projected surface area of the spherical particle, obtaining like this the efficiency factors:

$$Q_{abs} = \frac{C_{abs}}{\pi a^2}, Q_{sca} = \frac{C_{sca}}{\pi a^2}, Q_{ext} = \frac{C_{ext}}{\pi a^2} \qquad 2\text{-}4$$

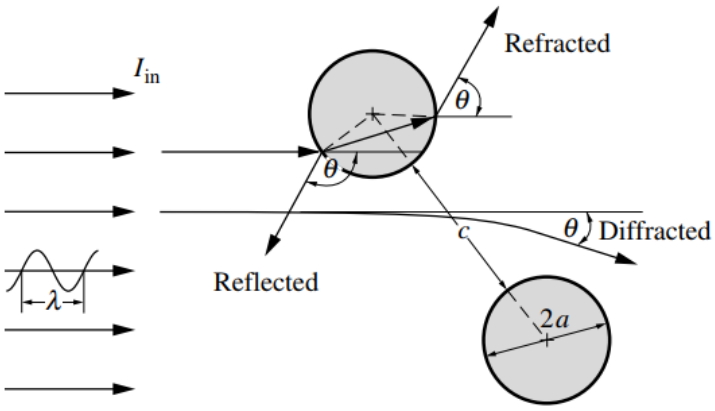

Figure 2-7: *Interaction of light with spherical particles [30]*

Radiation, when encountering a spherical particle may be scattered by an angle θ. Due to the spherical particle symmetry, an azimuthal angle is not needed to describe the scattering of light by the particle. On the other hand, the intensity of the wave scattered is proportional to two complex amplitude functions $S_1(\Theta)$ and $S_2(\Theta)$ which represent two perpendicular polarizations. The ratio between the scattered light intensity at the angle θ and the incident unpolarized light intensity is described by the relation [30,94,95] :

$$\frac{I_{sca}(\theta)}{I_{in}} = \frac{1}{2}\frac{i_1 + i_2}{x^2} \qquad 2\text{-}5$$

Where x = $\frac{2\pi a}{\lambda}$, and i_1, i_2 represent the nondimensional polarized intensities: $i_1(x, m, \theta) = \|S_1\|^2$, $i_2(x, m, \theta) = \|S_2\|^2$. From the definition of the scattering cross-section [94], one may write down the relation regarding the scattering efficiency:

$$Q_{sca} = \frac{C_{sca}}{\pi a^2} = \frac{1}{\pi a^2} a^2 \int_{4\pi} \frac{I_{sca}}{I_{in}} d\Omega = \frac{1}{x^2} \int_0^{\pi} (i_1 + i_2) \sin\theta \, d\theta \qquad 2\text{-}6$$

A significant physical quantity used to describe the scattering of light from particles is the scattering phase function $\Phi(\hat{s}_i,\hat{s})$. The scattering phase function represents the fraction of the energy that is scattered from the incident direction $\hat{s}_i$ to any given direction $\hat{s}$ and it is normalized over the solid angle:

$$\Phi(\Theta) = \frac{1}{4\pi}\int_{4\pi} \Phi(\hat{s}_i, \hat{s}) d\Omega = 1 \qquad 2\text{-}7$$

Based on the definition of the scattering phase function and using equation *2-5* together with equation *2-7*, we could express the phase function as below:

$$\Phi(\Theta) = \frac{i_1 + i_2}{\int_{4\pi}(i_1 + i_2) d\Omega} = 2\frac{i_1 + i_2}{x^2 Q_{sca}} \qquad 2\text{-}8$$

So, the scattering properties of light by a spherical particle can be expressed as a function of the complex amplitude functions $S_1(\Theta)$ and $S_2(\Theta)$. These two functions are derived from the Lorentz-Mie theory for the general case of arbitrary values of the complex index of refraction m and the size parameter x, and in the book of van de Hulst [94], derived as below:

$$S_1(\Theta) = \sum_{n=1}^{\infty} \frac{2n+1}{n(n+1)} [a_n \pi_n(\cos\Theta) + b_n \tau_n(\cos\Theta)] \qquad 2\text{-}9$$

$$S_2(\Theta) = \sum_{n=1}^{\infty} \frac{2n+1}{n(n+1)} \left[a_n \, \pi_n(cos\,\Theta) + \, b_n \, \tau_n(cos\,\Theta)\right] \qquad 2\text{-}10$$

Where the functions π_n and τ_n are related to the Legendre polynomials [96]:

$$\pi_n(cos\,\Theta) = \frac{dP_n(cos\,\Theta)}{d\,cos\,\Theta} \qquad 2\text{-}11$$

$$\tau_n(cos\,\Theta)] = cos\,\Theta\,\pi_n(cos\,\Theta) - sin^2\,\Theta\,\frac{d\,\pi_n\,(cos\,\Theta)}{d\,cos\,\Theta} \qquad 2\text{-}12$$

The coefficients a_n , b_n are called Mie scattering coefficients and are complex functions of x and y = mx:

$$a_n = \frac{\psi'_n(y)\psi_n(x) - m\psi_n(y)\psi'_n(x)}{\psi'_n(y)\zeta_n(x) - m\psi_n(y)\zeta'_n(x)} \qquad 2\text{-}13$$

$$b_n = \frac{m\psi'_n(y)\psi_n(x) - \psi_n(y)\psi'_n(x)}{m\psi'_n(y)\zeta_n(x) - \psi_n(y)\zeta'_n(x)} \qquad 2\text{-}14$$

The functions ψ_n, $\zeta_n(x)$ are called Riccati-Bessel functions [96].

This way, the determination of the characteristic quantities of light interaction with a spherical particle is reduced to the problem of the determination of the Mie scattering coefficients. The calculation of the Mie scattering coefficients is not trivial. Before developing electronic computers, there were no papers on computing scattering problems using Mie theory. At present, several computations algorithms are available. A significant step forward was the program MIEV0 written by Wiscombe [97,98]. He compared the accuracy of some Lorenz-Mie scattering numeric solution routines and discussed the efficiency of different calculation methods. From various studies, it is concluded that Mie's theory can be applied in the case of size parameters up to 10 [99,100]. On the other hand, this theory is still used as a standard reference to validate methods for more complex scattering problems [101,102]. Several other issues were studied, starting from Mie's theory. Aden and Kerker [103] published a theory for a coated dielectric sphere. Further, Kaiser and Schweiger [104] created an algorithm for a sphere having two coatings, and Li Kai [95] studied the case of spherical particles consisting of multiple layers.

Besides Lorentz-Mie theory, there were developed several other light scattering theories, like the Separation of Variables Method (SVM), T-Matrix, Generalized Multipole Technique (GMT), Null-Field Method with Discrete Sources (NFM-DS), Finite Difference Time Domain Method (FDTD), Finite Element Method (FEM), Method of Moments (MOM), Volume Integral Equation Method (VIEM) [96,97].

2.2.1 Henyey-Greenstein phase function

Strong forward-scattering peaks characterize large particles. An approximate phase function that could model the strong scattering peaks of the large particles is called Henyey-Greenstein (HG) phase function:

$$HG(\Theta) = \frac{1-g^2}{[1+g^2+2\,g\,cos\,\theta]^{3/2}}\,, \qquad 2\text{-}15$$

Where g is the asymmetry parameter and takes value in the segment [-1, 1]. Henyey-Greenstein phase function can also be written in the form of the Legendre polynomial series:

$$\mathrm{HG}(\Theta) = 1 + \sum_{n=1}^{\infty}(2n+1)\,g^n\,P_n\,(\cos\theta) \qquad 2\text{-}16$$

Van de Hulst [94] and Hansen [106] have shown that the HG phase function gives accurate results when the particles are non-dielectric [30]. Even though the microalgae are dielectric particles, this thesis shows that the HG bulk scattering model can give a very good approximation of the light scattered from a microalgal suspension.

The n-th order phase function, which would describe the scattering of light after n-scattering events, is given:

$$HG^{(n)}(\alpha) = \frac{1}{4\,\pi}\,\frac{1-{g_n}^2}{\left(1+{g_n}^2-2\,g_n\,cos(\alpha)\right)^{\frac{3}{2}}} \qquad 2\text{-}17$$

The mean cosine of the scattering angle after n-scattering events is $g_n = g^n$ [107,108].

2.2.2 Microalgae cell models

The composition of the microalgae cell, with several size scales and shapes of its components, makes the optical modeling of it a challenging task. However, according to [109], the molecular medium can be considered effectively homogeneous, leaving us with the task of considering only the cell organelles and the cell itself while dealing with the problem of modeling the microalgae interaction with light.

A forward and straightforward approach to model the interaction of light with the microalgal cells is to consider the latter as a homogeneous sphere with an effective complex index of refraction [110,31,36,111,112]. The imaginary part of the effective complex refractive index was retrieved from measurements of the spectral absorption coefficient by [110]; meanwhile, [58] asset it from measurements of pigment concentrations. The real part of the complex index of refraction was estimated using the relations of Kramers-Kronig [37,110,113]. The retrieved of the real part refractive index values are found to be in the interval (1.35-1.41), and the imaginary part of the refractive index assumes values in the interval (0.000-0.01), depending on the wavelength and the algal species [114,115]. This result is because microalgae cell is mainly made of water, which has a refractive index of 1.33; meanwhile, the organelles' refractive index changes from 1.36 in the case of cytoplasm to 1.51 for the chloroplast [37,77].

On the other hand, the refractive index of proteins, carbohydrates, and fates are 1.6, 1.53, and 1.46, respectively [90]. Meanwhile, for most organelles, the complex part of the index is close to zero, except for the pigments that absorb light, which have two peaks in the blue and red regions of the PAR [116]. This is why monitoring the algal growth is done mainly by measuring the Optical Density (OD) at 750 nm. Measuring at this wavelength avoids the absorption by the pigments, i.e., this is treated as pure light scattering measurement [117].

This model is not very accurate. It can be used to model light absorption from the cells, but it fails to accurately predict the scattering phase function and the spectral backscattering ratio [77,118]. Moreover, the model is not sufficient to describe the polarization properties of the scattered field. Quirantes and Bernard [39] modeled the cell as a coated sphere to address these problems. The outer coating represented the optical properties of the chloroplast, and the inner coating described the optical properties of the cytoplasm and other organelles. On the other hand, Bhowmik and Pilon [77] modeled the heterogenous nature of the microalgae cell using the T-matrix method. They compared the results with the volume-equivalent homogeneous sphere model and with the coated sphere

approximation and concluded that both approximations failed to give accurate results of the scattering phase function.

Another approach followed by the researchers was to consider the shape of the cells and not approximate them as spherical [58].

Until now, a model was not developed that considers both the heterogeneous nature of the cell and its shape.

2.3 Derivation of RTE for a non-absorbing medium

So far, we have discussed the optical properties of the microalgae cells individually. An algal suspension is a random distribution of discrete absorbing scatters and can be described by the radiative transfer equation for a non-emitting medium. In the paragraph below, we will write the radiative transfer equation in the general case for an emitting medium, deriving it step by step. Then, we will simplify it for a non-emitting medium in a second moment.

Let's denote I_λ the radiative energy flow per unit of time per unit solid angle per unit wavelength and unit area normal to the rays. In an absorbing medium, the absolute amount of absorption is directly proportional to the magnitude of the incident intensity:

$$(dI_\lambda)_{abs} = -\kappa_\lambda I_\lambda ds, \qquad 2\text{-}18$$

Where, κ_λ (m^{-1}) is the absorptions coefficient, and *ds* is the distance light has traveled through the medium.

If we consider the attenuation of light by out-scattering (scattering away from the direction that is considered), we may write:

$$(dI_\lambda)_{sca} = -\sigma_{s\lambda} I_\lambda ds, \qquad 2\text{-}19$$

Where, $\sigma_{s\lambda}$ (m^{-1}) is the scattering coefficient.

As a result, the total attenuation of the light intensity will be characterized by the extinction coefficient:

$$\beta_\lambda = \sigma_{s\lambda} + \kappa_\lambda \qquad 2\text{-}20$$

On the other hand, apart from the attenuation of light intensity due to absorption and out-scattering, light intensity augmentation also occurs due to in-scattering.

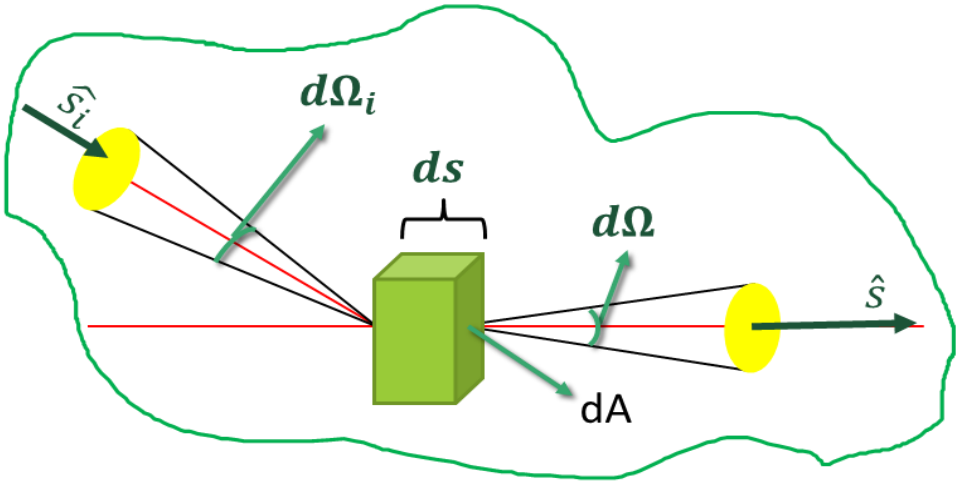

Figure 2-8: *A pencil of rays within the algal suspension scattered from the direction $\hat{s}_i$ in the direction $\hat{s}$*

Let's consider an infinitesimal pencil of rays impinging on a volume element $dV = dA\ ds$, in the direction $\hat{\boldsymbol{s}}_{\boldsymbol{i}}$ as shown in Figure 2-9. From the definition of the light intensity at the beginning of this section, the spectral radiative heat flux, impinging on the area dA, within the solid angle $d\Omega_i$ can be written as below:

$$I_\lambda(\hat{\boldsymbol{s}}_i)(dA\,\hat{\boldsymbol{s}}_i \cdot \hat{\boldsymbol{s}})\,d\Omega_i\,d\lambda$$

From a simple geometrical analysis, one can find that this flux travels through the volume dV for a distance $\frac{ds}{\hat{\boldsymbol{s}}_{\boldsymbol{i}} \cdot \hat{\boldsymbol{s}}}$. As a result, according to equation 2-19, the total amount of the flux of energy scattered away from the direction $\hat{\boldsymbol{s}}_i$ will be:

$$\sigma_{s\lambda}(I_\lambda(\hat{\boldsymbol{s}}_i)(dA\,\hat{\boldsymbol{s}}_i \cdot \hat{\boldsymbol{s}})\,d\Omega_i\,d\lambda)\left(\frac{ds}{\hat{\boldsymbol{s}}_{\boldsymbol{i}} \cdot \hat{\boldsymbol{s}}}\right) = \sigma_{s\lambda}\,I_\lambda(\hat{\boldsymbol{s}}_i)\,dA\,d\Omega_i\,d\lambda\,ds \qquad 2\text{-}21$$

Not all the amount of the flux scattered in the direction $\hat{\boldsymbol{s}}_{\boldsymbol{i}}$, will be scattered into the cone $d\Omega$ around the direction $\hat{\boldsymbol{s}}$. Indeed, the fraction of the flux scattered into the cone dΩ can be described with the phase function $\Phi_\lambda\,(\hat{\boldsymbol{s}}_i, \hat{\boldsymbol{s}})$ help:

$$\sigma_{s\lambda}\,I_\lambda(\hat{\boldsymbol{s}}_i)\,dA\,d\Omega_i\,d\lambda\,ds\frac{\Phi_\lambda(\hat{\boldsymbol{s}}_i, \hat{\boldsymbol{s}})}{4\pi}\,d\Omega \qquad 2\text{-}22$$

Where $\frac{1}{4\pi}$ is the normalization constant for the phase function, so that equation *2-7* is satisfied. By integrating over the total solid angle, we can calculate the energy flux scattered into the direction $\hat{\boldsymbol{s}}$ from all the incoming directions $\hat{\boldsymbol{s}}_{\boldsymbol{i}}$:

$$(dI_\lambda)_{sca}(\hat{\boldsymbol{s}})\, dA\, d\Omega\, d\lambda = \int_{4\pi} \left(\sigma_{s\lambda}\, I_\lambda(\hat{\boldsymbol{s}}_i)\, \mathrm{dA}\, d\lambda\, ds \frac{\Phi_\lambda(\hat{\boldsymbol{s}}_i, \hat{\boldsymbol{s}})}{4\pi}\right) d\Omega\, d\Omega_i$$

Which can be written:

$$(dI_\lambda)_{sca}(\hat{\boldsymbol{s}}) = \frac{\sigma_{s\lambda}}{4\pi}\, ds \int_{4\pi} (\, I_\lambda(\hat{\boldsymbol{s}}_i)\, \Phi_\lambda(\hat{\boldsymbol{s}}_i, \hat{\boldsymbol{s}}))\, d\Omega_i \qquad 2\text{-}23$$

Another process that we should consider before preparing to write the RTE is the emission. The change of intensity due to emission will be given:

$$(dI_\lambda)_{em} = j_\lambda\, ds, \qquad 2\text{-}24$$

Where j_λ is called emission coefficient. At local thermodynamic equilibrium, the intensity everywhere must be equal to black body intensity. As a result:

$$j_\lambda = \kappa_\lambda\, I_{b\lambda} \qquad 2\text{-}25$$

So, substituting equation *2-30* into equation *2-30*, we have:

$$(dI_\lambda)_{em} = \kappa_\lambda\, I_{b\lambda}\, ds \qquad 2\text{-}26$$

Now taking into consideration equations 2-18, *2-19*, *2-23*, *2-26*, we can make an energy balance on the radiative flux of energy traveling in the direction $\hat{\boldsymbol{s}}$ within a small pencil of rays as depicted in Figure 2-9:

$$I_\lambda(s+ds, \hat{\boldsymbol{s}}, t+dt) - I_\lambda(s, \hat{\boldsymbol{s}}, t) = \kappa_\lambda\, I_{b\lambda}\, ds - \kappa_\lambda I_\lambda(s, \hat{\boldsymbol{s}}, t) ds - \sigma_{s\lambda} I_\lambda(s, \hat{\boldsymbol{s}}, t) ds + \frac{\sigma_{s\lambda}}{4\pi}\, ds \int_{4\pi} (\, I_\lambda(\hat{\boldsymbol{s}}_i)\, \Phi_\lambda(\hat{\boldsymbol{s}}_i, \hat{\boldsymbol{s}}))\, d\Omega_i \qquad 2\text{-}27$$

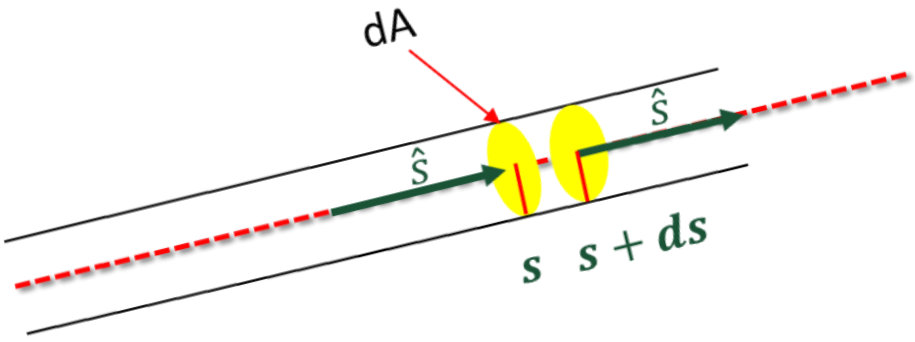

Figure 2-9*: A pencil of rays inside the suspension in the direction ŝ*

The outgoing intensity can be expanded into Taylor series:

$$I_\lambda(s+ds,\hat{\mathbf{s}},t+dt) = I_\lambda(s,\hat{\mathbf{s}},t) + dt\,\frac{\partial I_\lambda}{\partial t} + ds\,\frac{\partial I_\lambda}{\partial s} \qquad 2\text{-}28$$

This way, substituting relation 2-28 in relation 2-27 and keeping in mind that ds = c dt we have:

$$\frac{1}{c}\frac{\partial I_\lambda}{\partial t} + \frac{\partial I_\lambda}{\partial s} = \kappa_\lambda I_{b\lambda} - \kappa_\lambda I_\lambda - \sigma_{s\lambda} I_\lambda + \frac{\sigma_{s\lambda}}{4\pi}\int_{4\pi}\left(I_\lambda(\hat{\boldsymbol{s}}_i)\,\Phi_\lambda(\hat{\boldsymbol{s}}_i,\hat{\mathbf{s}})\right) d\Omega_i \qquad 2\text{-}29$$

This equation results from several assumptions, i.e., the medium is homogeneous, and at rest, the medium is nonpolarizing, and the medium has a constant index of refraction. The RTE for a medium with a varying refractive index has been derived by Pomraning [119]. However, for most engineering applications, like in our case, the speed of light is very large compared to local time and length scales. As a result, the first term in equation *2-34* can be neglected:

$$\left(\frac{dI_\lambda(\hat{\boldsymbol{s}})}{ds}\right) = \hat{\mathbf{s}}_i \cdot \nabla I_\lambda = \kappa_\lambda I_{b\lambda} - \kappa_\lambda I_\lambda - \sigma_{s\lambda} I_\lambda + \frac{\sigma_{s\lambda}}{4\pi}\int_{4\pi} I_\lambda(\hat{\boldsymbol{s}}_i)\,\phi_\lambda(\hat{\boldsymbol{s}}_i,\hat{\boldsymbol{s}})\,d\Omega_i \qquad 2\text{-}30$$

2.3.1 Methods to solve the RTE

Before discussing different methods studied to solve the RTE, let's derive the formal solution. For this, we need to write the RTE in terms of nondimensional optical coordinates, so let's introduce:

$$\tau_\lambda = \int_0^s \kappa_\lambda + \sigma_{s\lambda}\,ds = \int_0^s \beta_\lambda\,ds \qquad 2\text{-}31$$

And on the other hand, we will also define the single scattering albedo as:

$$\omega_\lambda = \frac{\sigma_{s\lambda}}{\sigma_{s\lambda} + \kappa_\lambda} = \frac{\sigma_{s\lambda}}{\beta_\lambda} \qquad 2\text{-}32$$

As a result, using relations *2-31* and *2-37* in the RTE, the latter can be written in the form:

$$\frac{dI_\lambda}{d\tau_\lambda} = -I_\lambda + (1-\omega_\lambda) I_{b\lambda} + \frac{\omega_\lambda}{4\pi}\int_{4\pi} I_\lambda(\hat{\boldsymbol{s}}_i)\,\phi_\lambda(\hat{\boldsymbol{s}}_i,\hat{\boldsymbol{s}})\,d\Omega_i \qquad 2\text{-}33$$

The last two terms in equation *2-33* are called the source function for the radiative intensity:

$$S_\lambda(\tau_\lambda, \hat{\boldsymbol{s}}) = (1 - \omega_\lambda) I_{b\lambda} + \frac{\omega_\lambda}{4\pi} \int_{4\pi} I_\lambda(\hat{\boldsymbol{s_i}})\, \phi_\lambda(\hat{\boldsymbol{s_i}}, \hat{\boldsymbol{s}})\, d\Omega_i \qquad 2\text{-}34$$

Finally, the RTE will be written in the form:

$$\frac{dI_\lambda}{d\tau_\lambda} + I_\lambda = S_\lambda(\tau_\lambda, \hat{\boldsymbol{s}}) \qquad 2\text{-}35$$

A formal solution to this equation will be:

$$I_\lambda(\tau_\lambda) = I_\lambda(0)\, e^{-\tau_\lambda} + \int_0^{\tau_\lambda} S_\lambda(\tau'_\lambda, \hat{\boldsymbol{s}}) e^{-(\tau_\lambda - \tau'_\lambda)} d\tau'_\lambda \qquad 2\text{-}36$$

The first term in equation *2-41* is the contribution to the local intensity by the intensity entering at s = 0, which decays exponentially due to extinction. The integrand is related to emission from the medium.

Analytical exact solutions to the radiative transfer equation are complex. Researchers have followed two approaches to solving the RTE:

i) Develop exact solutions for idealized situations

ii) Develop approximate solution methods for more real situations

Most exact solutions are limited to gray media. The media are isothermal or at radiative equilibrium, and the scattering is usually considered isotropic.

There exist several approximate methods for the one – dimensional problem. Schuster [120] and Schwarzschild individually developed a simple solution for a one-dimensional, plane-parallel slab. They assumed the radiative intensity isotropic but different over the upper and lower hemisphere and derived the solution for a non – scattering media. Since this method divides the intensity into two constant components for two directions, is often called the *two-flux approximation method [30]*.

Another method for the one-dimensional plane-parallel slab is the *Milne-Eddington approximation method* (moment method), developed independently from Milne and Eddington [30,121,122].

The spherical harmonics method permits finding an approximate solution of an arbitrarily high order to equation 2.33 in the case of the grey medium by transforming it in a set of partial differential equations (PDEs). The disadvantage of this method is that low order approximations are accurate only in media with near isotropic radiative intensity, and

the high order approximations are characterized by mathematical complexity [30]. Descriptions of this method can be found in the books of Kourganoff [123], Davison [124] and Murray [125], and Modest [30].

Another method to solve the RTE is the *Discrete Ordinate Method (*DOM). Like the spherical harmonics method, DOM is a tool to transform the RTE into a set of partial differential equations and can be carried out to any arbitrary order. In this method, the transfer equation is solved for a set of discrete directions spanning the total solid angle range of 4π. In other words, integrals over the solid angle are approximated by numerical quadrature as below:

$$\hat{s}_i \cdot \nabla I(\boldsymbol{r}, \widehat{\boldsymbol{s}_i}) = \kappa(\boldsymbol{r}) I_b(\boldsymbol{r}) - \beta(\boldsymbol{r}) I(\boldsymbol{r}, \widehat{\boldsymbol{s}_i}) + \frac{\sigma_s(\boldsymbol{r})}{4\pi} \sum_{j=1}^{n} \omega_j I\left(\boldsymbol{r}, \widehat{\boldsymbol{s}_j}\right) \Phi(\boldsymbol{r}, \hat{\boldsymbol{s}}_i, \hat{\boldsymbol{s}}_j) \qquad 2\text{-}37$$

Where ω_j are the quadrature weights associated with directions $\widehat{\boldsymbol{s}_j}$.

Nowadays, instead of finite differences, like in the DOM, solving the RTE is also being used finite volumes, and the method is called *Finite Volume Method* (FVM). Both methods are prevalent, and some versions are incorporated in most commercial *Computational Fluid Dynamics* (CFD) codes. A description of these methods was done by Coelho [126]. Furthermore, *Monte Carlo Method* is another technique used to solve the RTE for a gray medium. This method consists of tracing the photons from their point of emission to their point of absorption. Details about this method can be found in the books of Modest [30] or Howell [127].

Another method for which the interest is increasing is the *Lattice Boltzmann Method* (LBM). This method originates from fluid dynamics problems [126], but lately, it has been successfully implemented in heat transfer problems.

All the methods mentioned until now are used in the case of a gray medium, i.e., the absorption coefficient, the scattering coefficient, the emission coefficient, and the phase function are considered constant over the electromagnetic spectrum.

2.3.2 Radiative Transfer Equation for microalgae suspension

The microalgal suspension is a non-emitting medium. As a result, for this case, the emission coefficient will be zero, $j_\lambda = 0$. So, the RTE will have the form:

$$\left(\frac{dI_\lambda(\hat{\boldsymbol{s}})}{ds}\right) = \hat{\boldsymbol{s}}_i \cdot \nabla I_\lambda = -\kappa_\lambda I_\lambda - \sigma_{s\lambda} I_\lambda + \frac{\sigma_{s\lambda}}{4\pi}\int_{4\pi} I_\lambda(\hat{\boldsymbol{s}_i})\,\phi_\lambda(\hat{\boldsymbol{s}_i}, \hat{\boldsymbol{s}})\,d\Omega_i$$

The methods used to solve the RTE by the researchers in the field of microalgae growth are the ones mentioned in section 1.

In the study of [128], *Monte Carlo Method* was coupled with an optimization algorithm. The optimization algorithm was used to determine the algal suspension's radiative parameters, which were used later to solve the RTE utilizing the *Monte Carlo Method*. This method allowed them to calculate the local monochromatic energy density at any position inside the algal suspension. The species for which the experimental measurements and the simulations were carried out in their work were *Chlorella sp.* and *Scenedesmus quadricauda*.

McHardy [43] instead used the *Lattice Boltzmann Method* to solve the RTE for a suspension of microalgae. He coupled fluid dynamics with the RTE in his work, considering the gas bubbles like this. The solution was carried out for monochromatic radiation. The radiative properties of the cells used in McHardy's study were taken from Kandilian [127]. In another study, McHardy [42] tried to solve the problem of the lack of information related to polychromatic light inside the PBR. This way, he solved the RTE by applying the LBM for monochromatic wavelengths, then used the Newton Cote formulas to integrate over the whole spectrum. As a result, in this work were obtained polychromatic light intensity profiles within the algal suspension.

Kong and Vigil [44] used the *Discrete Ordinate Method* to solve the RTE for a microalgae suspension. They implemented a non-gray DOM method by dividing the radiation spectrum into N wavelength bands, where each was treated in the same manner as for the gray model. To facilitate the multidimensional spectral implementation of the DOM method for solving the RTE, they used the open-source finite volume CFD toolbox OpenFOAM [130].

2.4 Spectral light intensity for microalgae growth

2.4.1 Light intensity

Light intensity plays a prominent role in microalgae growth. Since photochemical reactions during the photosynthesis process depend on the number of photons, the quantity

of light shined on the microalgae culture is described by photon flux density (PFD), whose units are ($\mu mol\ photons/m^2s$) or ($\mu\ E/m^2s$). The intensity of light of a specific wavelength can be converted into pfd using the relation:

$$\mathrm{PFD}_\lambda = \frac{\mathrm{I}_\lambda}{\mathrm{E}_{\mathrm{ph},\lambda} * \mathrm{N}_\mathrm{A}} \left(\mu\mathrm{mol}\,\frac{\mathrm{photons}}{\mathrm{m^2 s}}\right), \qquad 2\text{-}38$$

Where I_λ (W/m^2) is the intensity of light, $E_{ph,\lambda}$ represents the energy of the photon of a specific wavelength λ, and N_A is the Avogadro number.

To convert the intensity of light in the photosynthetically active radiation (PAR) region I (λ), in PFD, firstly, we should consider that light intensity corresponding to the interval of wavelengths ($\lambda, \lambda + \Delta\lambda$) may be given:

$$\Delta I = \mathrm{I}(\lambda)\Delta\lambda \qquad 2\text{-}39$$

Further, the number of photons per square meter per second in the interval ($\lambda, \lambda + \Delta\lambda$) is calculated:

$$\text{photons/ m}^2\text{s} = \frac{\lambda}{hc} I(\lambda)\Delta\lambda \qquad 2\text{-}40$$

Integrating from 400 nm to 700 nm is obtained the number of photons per square meter per second in the PAR region. Further, dividing this result by the Avogadro number is calculated the PFD in the PAR region.

$$\mathrm{PFD} = \frac{1}{\mathrm{N_A hc}} \int_{4\mathrm{x}10^{-9}}^{7\mathrm{x}10^{-9}} \lambda\, \mathrm{I}(\lambda)\mathrm{d}\lambda \qquad 2\text{-}41$$

In practical situations, the intensity of light in the PAR region can be measured in ($\mu mol\ photons/m^2s$) units via a LiCor Li-250 Light Meter provided with a Li-190 quantum sensor.

One of the most essential facts about the quantity of light used for microalgae cultivation is that a uniform illumination of the microalgae culture must be provided. Uniform illumination is difficult to achieve in dense cultures because of self-shading [131].

The photosynthetic activity of microalgae is described based on measurements of oxygen evolution (the rate of oxygen production during the photosynthesis process) as a function of light intensity. A representation of the effect of the light quantity on the photosynthetic process is given by the light–response curve, which is a typical curve that shows how the rate of photosynthesis ($\mu mol\ O_2/m^2s$) changes with the increase of light intensity.

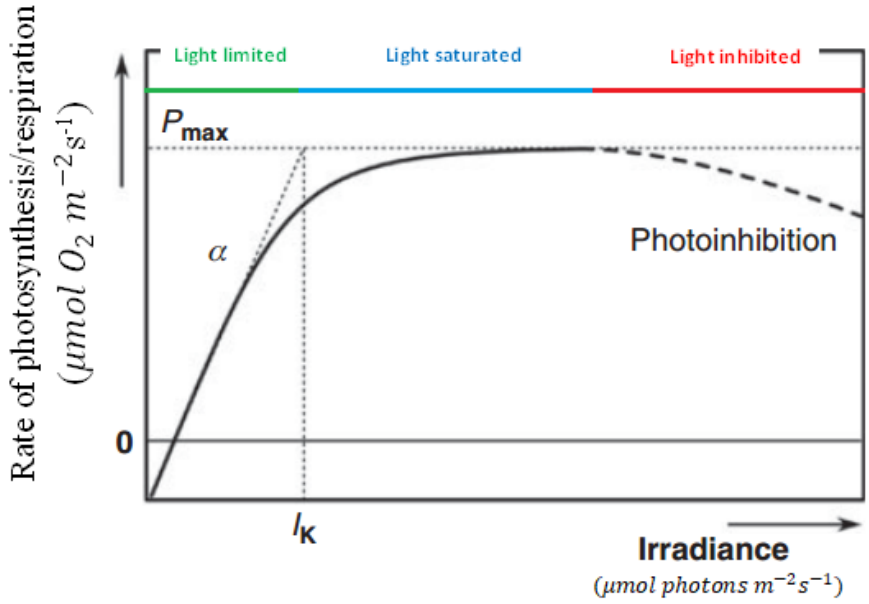

Figure 2-10: *Schematic representation of the rate of the photosynthesis as a function of irradiance [62]*

In **Figure *2-10*** can be noticed that there is a net consumption of oxygen for low intensities because of respiration (the negative part of the curve). It is possible to highlight three regions:

- The light-limited region: It is evident from the graph that for small values of intensity, the rate of photosynthesis increases linearly with the increase of light intensity. In this region, irradiance is used with maximum efficiency. The slope α is a measure of the maximum photosynthetic efficiency of light conversion. The interception of α with the maximum rate of photosynthesis P_{max} represents the saturation irradiance I_K.
- The saturation region: When the intensity of light used for microalgae growth is greater than the saturation irradiance I_K, the photosynthesis rate becomes independent of light intensity.
- The light inhibited region: The process of photosynthesis becomes less and less efficient with the increase of intensity. This phenomenon is called photoinhibition of photosynthesis. [62,132]

2.4.2 Spectral composition of light

Photosynthetic organisms have different light-harvesting mechanisms, allowing them to use only specific wavelengths. This is why the management of incident light is crucial to increasing the productivity of microalgae.

For example, *Nannochloropsis oculata* contains only one type of chlorophyll, *chl a*, and the other pigments found in this species of microalgae are the carotenoids: *violaxanthin, astaxanthin, antheraxanthin, vaucheriaxanthin, zeaxanthin, canthaxanthin, and β-carotene*. The absorption spectrum of *Nannochloropsis oc.* is characterized by two peaks corresponding to blue and red wavelengths. However, not all the absorbed photons are photosynthetically efficient. The action spectrum, which measures the rate of photosynthesis across PAR region based on oxygen evolution, gives information about the most photosynthetically efficient wavelengths.

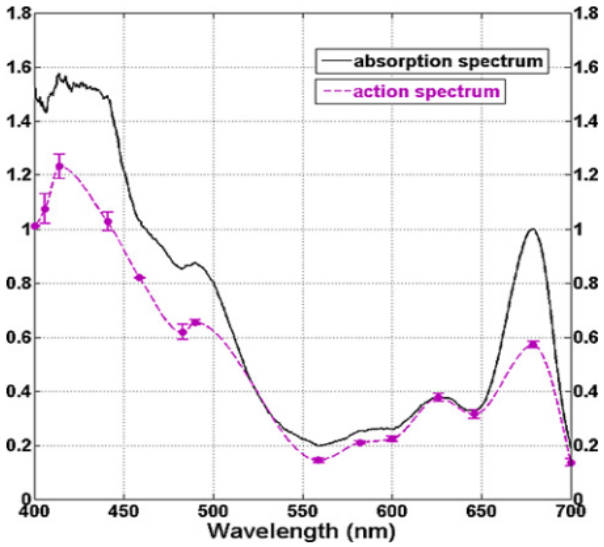

Figure 2-11: *The absorption spectrum and the action spectrum of Nannochloropsis oculata [133].*

The most interesting conclusion that can be pointed out from **Figure *2-11*** is that green photons, even if they are absorbed in small quantities, are photosynthetically efficient [133]. The light source needed for microalgae growth can be provided naturally or artificially.

2.5 Cultivation methods

Microalgae can be cultivated in open tanks or closed vessels called photobioreactors (PBR). Opens systems are classified into natural open systems like lagoons, lakes, and artificial open systems called open ponds.

2.5.1 Open ponds

Nowadays, open ponds are the most widespread microalgae cultivation systems. They have a variety of shapes and sizes and are preferable for large-scale growth of microalgae because of their low-cost construction, simplicity of design, and high production capacity. However, these systems have a low-efficiency production because of the impossibility of controlling growth parameters and the high probability of contamination of microalgae culture.

Open ponds can be classified into circular ponds, raceway ponds, and inclined systems based on their shape.

- Circular ponds, as the name indicates, have a circular form. A rotating agitator mixes the culture. These systems can't have an area greater than 10000 m^2 because otherwise, the mixing wouldn't be effective [134].

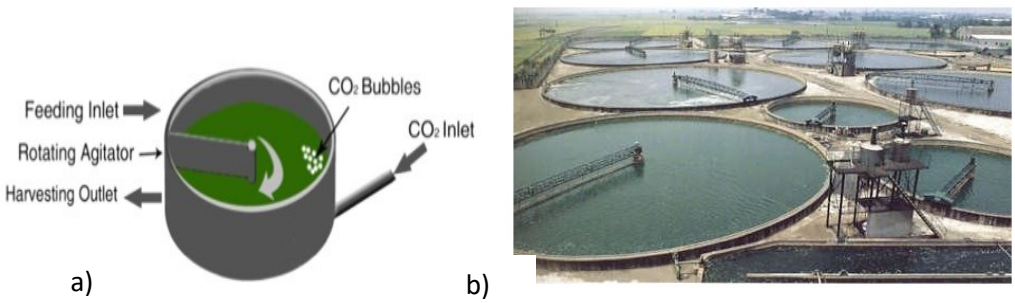

Figure 2-12: *a) A schematic circular open pond with the main elements; b) A circular open pond for spirulina cultivation [134,135].*

- Raceway ponds have a raceway shape, and they are provided with an agitating arm that serves for mixing and circulation.

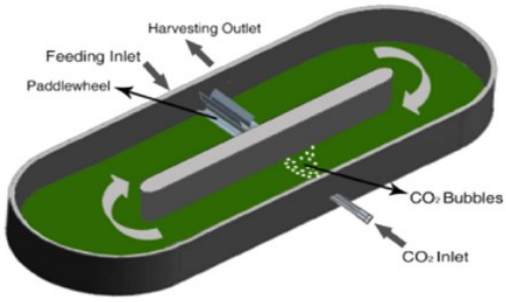

a)

b)

Figure 2-13: *a) A schematic presentation of a raceway pond; b) Raceway Pond for biodiesel production [134,135].*

2.5.2 Photobioreactors

Photobioreactors are closed systems where life parameters for microalgae growth, like light, CO_2, pH, and temperature, are kept under control. Compared with open ponds, these systems are characterized by higher values of photosynthetic efficiency, biomass productivity, and biomass concentration. These higher values are related to the fact that the key growth parameters for microalgae inside a photobioreactor can be controlled. Moreover, the PBR prevents the contamination of the culture [136].

The requirements that a photobioreactor should fulfill to be called efficient are:

1) Channel and distribute the light into the cultivation vessel in such a way that a uniform illumination of the culture can be achieved
2) Allow convenient and precise control of important operational parameters so that a high growth rate of microalgae culture can be achieved
3) Minimize the capital costs and operational costs
4) Minimize energy consumption during the operation

There exist a variety of photobioreactors. Based on their geometrical structure, photobioreactors can be categorized into: flat-plate photobioreactors, tubular photobioreactors, vertical column photobioreactors [136].

- A Flat – Plate photobioreactors has the form of a regular parallelepiped, whose width is small compared with its length and height.

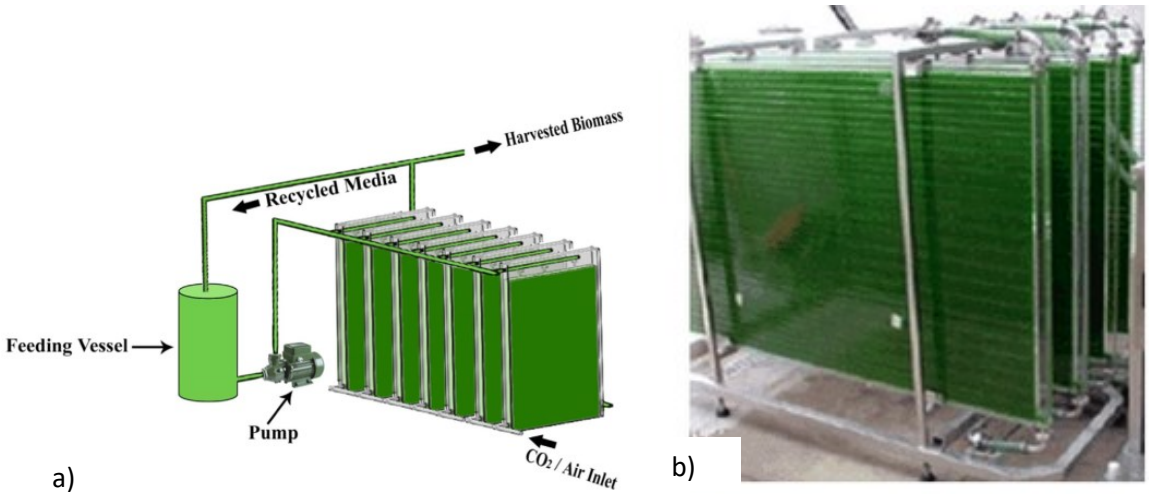

Figure 2-14: *a) Schematic view of a Flat – Plate photobioreactor; b) Flat plate photobioreactor [4,137].*

Flat – Plate photobioreactors have received a great interest in research due to their high surface-to-volume ratio, which favors a good illumination of the culture. High cell densities also characterize this type of photobioreactor. Mixing is achieved mechanically using a motor or bubbling air through a perforated tube.

- A tubular photobioreactor has a tubular geometry with horizontal, inclined, and vertical orientations. A large surface-to-volume ratio characterizes these photobioreactors, making the culture's uniform illumination easier. On the other hand, the geometrical shape of tubular photobioreactors leads to gradients of pH, dissolved O_2, and CO_2 along the tubes, which negatively affects the microalgae growth.

-

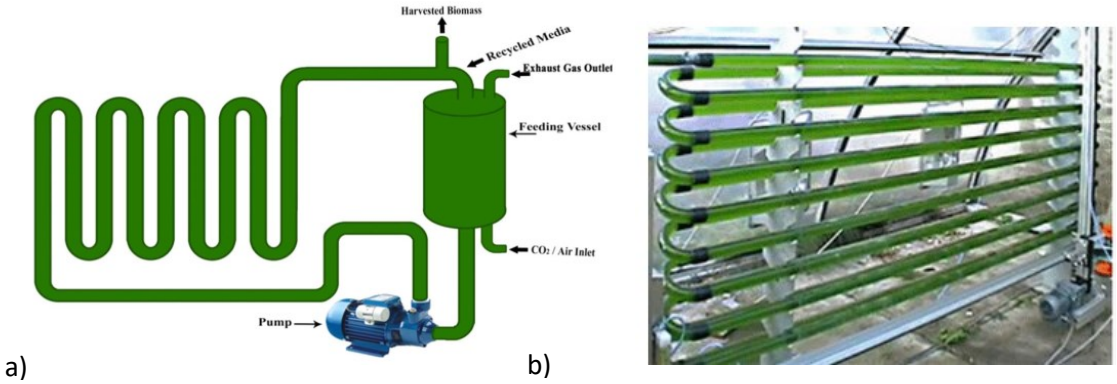

Figure 2-15*: a) Schematic view of a tubular photobioreactor; b) Tubular photobioreactor [134,137].*

- The vertical Column Photobioreactor has a cylindrical shape characterized by a small radius compared with its height to achieve a good surface to volume ratio. Mixing of the culture is achieved by bubbling air or air enriched with CO_2 gas. This way, mixing is more efficient because it is gentle enough not to damage the microalgae culture. Vertical Column Photobioreactors that are provided with an internal column are called airlift PBR. In this case, the velocity of air rising is greater than the downcoming air, which results in a better mixing and a better illumination of the culture (we are considering the case when microalgae culture is illuminated from the outer surface of the cylinder).
- Meanwhile, the vertical column PBR that is split into two columns is called split-column airlift PBR. These vertical columns PBRs were created to better mix the microalgae culture without damaging them. Schematic views of these photobioreactors are shown in the figure below [136].

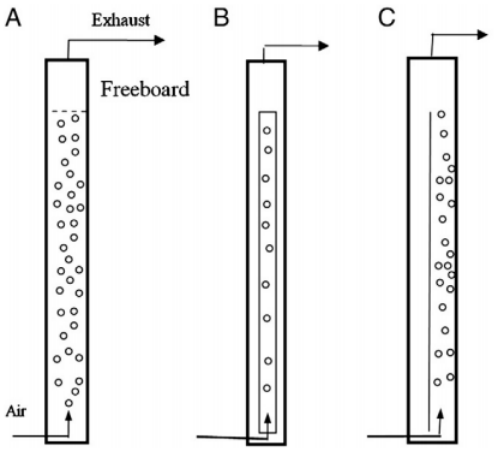

Figure 2-16: *Schematic representation of A) vertical column PBR; B) airlift PBR; C) split-column airlift PBR [136].*

Chapter 3

Photobioreactors

During this thesis were developed two photobioreactors for microalgae cultivation: a multiple tube photobioreactor and an annular photobioreactor. This chapter will describe the photobioreactors and the software designed for their illumination.

3.1 Multiple tube photobioreactor

3.1.1 The construct of the multiple tube PBR

The multiple tube PBR is an internally illuminated, vertical column photobioreactor with a capacity of about 5000 l. The height of the PBR is 5000 mm. The mixing process is achieved by bubbling air enriched with CO_2 through an aeration membrane placed on the bottom of the photobioreactor.

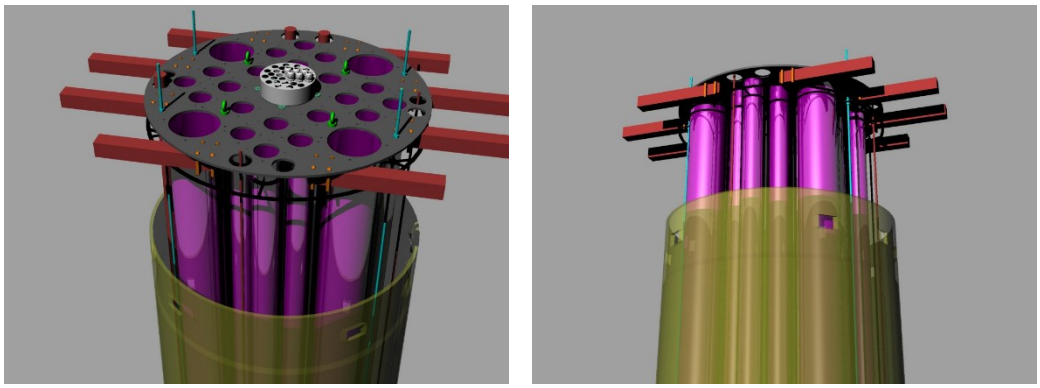

Figure 3-1: *Rendering of the multiple tube PBR developed by the University of Ferrara*

3.1.2 Illumination of the multiple tube PBR

Sun light, concentrated via Solar Lens Panels, is used to illuminate the multiple tube PBR. The Solar Lens Panel (SLP) is a Fresnel concentrator, which is comprised of 25 groups of Fresnel lenses with dimensions of (27x27) cm. Each group of lenses contains 100 Fresnel lenses divided into four subgroups with dimensions of (13.5x13.5) cm with 25 lenses each. The size of the lenses is 2.7 cm in diameter.

Every subgroup of lenses is fixed on a PMMA structure found behind them called a backplate. The backplate itself is set on the aluminum structure of the solar concentrator via four screws. On the PMMA, at the focal length of the lenses, are positioned the optical fibers. They are placed on some structures of the PMMA called fiber holders. It is essential to underline that the entry surface of the optical fibers is embedded inside the material of the fiber holders. The optical fibers corresponding to each block of Fresnel lenses are grouped into bundles of optical fibers. So, every concentrator results in 25 bundles, each containing 100 optical fibers.

The Fresnel lenses and the PMMA back-plate, together with the holders of the optical fibers, are arranged in a closed system with a transparent cover on one side and an aluminum foil on the other side. The purpose of the transparent cover is to protect the lenses and the holders of optical fiber from impurities, trying to prevent a possible burn of the optical fibers' holders.

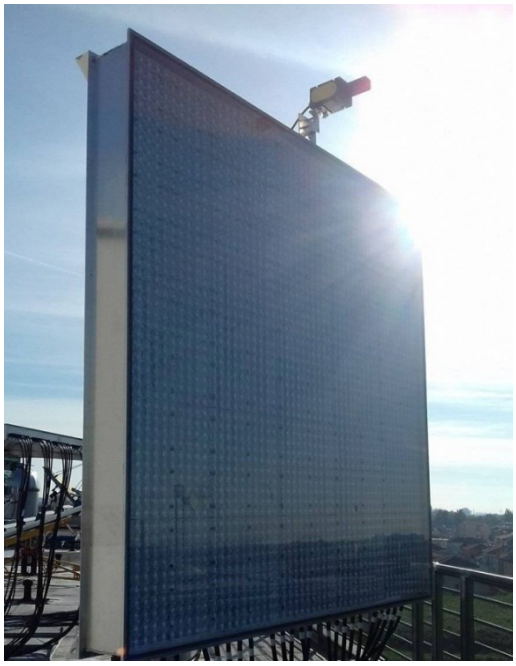

Figure 3-2: *The Solar Lens Panel (SLP) equipped with a sun tracking sensor developed by University of Ferrara*

To achieve a uniform distribution of the concentrated light within the photobioreactor are used 15 light diffusers. The bundles of optical fibers are inserted in the top part of the light diffusers and held in place with cable glands.
The light diffuser is similar to a light pipe: It has a cylindrical shape, and its inner surface is partially covered by stripes of an optical light film (OLF). The OLF has triangle-shaped apertures, whose width is engineered in such a way to spill a quasi-uniform light intensity along the whole height of the PBR.
OLF is a transparent optic film with a smooth surface on one side and a prismatic structure on the other side. This structure enables OLF to be reflective at some angles of incidence and transparent at some different angles. In this case, it is utilized the reflective ability of OLF because it enables the transportation of light through the light diffusor. Meanwhile, in the parts of the light diffusor where the OLF is missing, light escapes. The bases of the OLF - triangles are chosen to be on the upper side of the diffusor because the light intensity is higher in this part. Meanwhile, at the end of the diffusor, light intensity is low due to attenuation. That's why a greater area through which light can escape is needed to have a uniform distribution of light through the length of the diffusor.
To put out the residual light, at the end of the light diffusor, is installed an object in the form of a cone, which is covered with a Light Extract Film (LEF) that enables light extraction
A LabVIEW® software is used to activate the SLP number needed to provide the light within the PBR based on the concentration of the algal suspension.

3.2 Annular photobioreactor

3.2.1 The construct of the annular PBR

The annular photobioreactor is a property of Biosyntex srl. It is composed of an inner polymethyl methacrylate (PMMA) tube with a diameter of 400 mm and an outer PMMA tube with a diameter of 500 mm. The height of the PBR is 2000 mm. The thickness of the PMMA tubes is 5 mm. The mixing process is achieved by bubbling air enriched with CO_2 through an aeration membrane placed at the bottom of the photobioreactor.

3.2.2 Illumination of the annular PBR

The PBR is illuminated artificially. Eight LED bars with 60 LEDs each, equally spaced, are placed around the PBR. The LEDs are of three types: white (**GW CSSRM2.PM**), blue (**L1F3 – U410200014000**), and red (**GH CSSRM2.24**), and are placed in an alternated mode along the height of the PBR. Meanwhile, on the cover of the PBR are placed 250 LEDs, still in an alternated mode. The light produced by the LEDs of the cover is uniformly distributed along the PBR height using OLF, as explained in section 3.1.2.

The red LED has a peak at 660 nm and is characterized by a radiant flux of 1.3 W at a current of 1 A. The blue LED has a peak at 410 nm, and a radiometric power of 1.4 W characterizes it at 1A. Meanwhile, the white LED has a radiometric power of 1.359 W. The distance between the LEDs is 96 mm; meanwhile, the distance of the LED bar from the outer tube of the PBR is 70 mm.

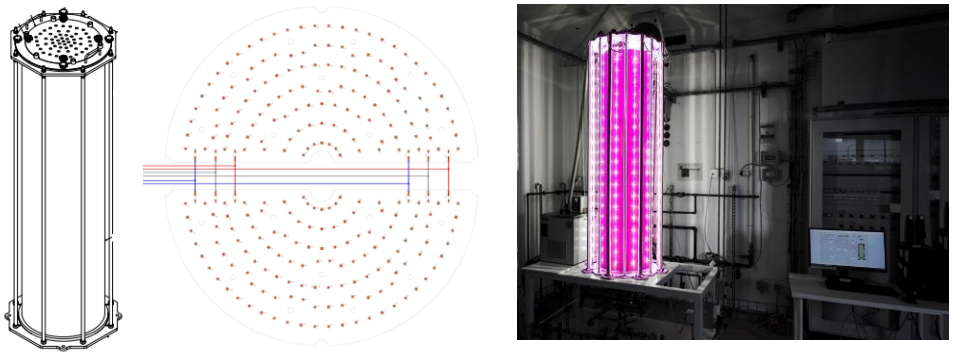

Figure 3-3*: Schematic design of the annular PBR (left); Schematic representation of the LEDs in the cover of the PBR (middle); Picture of the annular PBR with the LEDs turned on (right)*

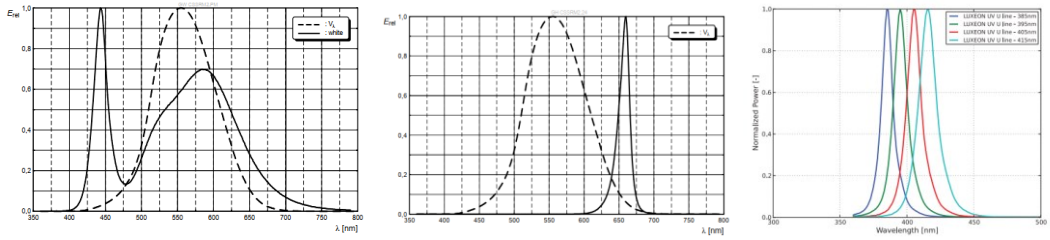

Figure 3-4: *Relative spectral emission curves of white LED (left), red LED (middle), blue LED (right, cyan plot)*

The choice of the red and blue LEDs is consistent with the absorption spectrum of a-type chlorophyll. Meanwhile, the white LEDs have been chosen because, as shown in ***Figure 2-3***, they can be used to cultivate different species, not only *N. Oculata.*

LEDs of the same type have been connected in series to emit the same optical power. In addition, LEDs with different chemistry are connected to other channels to tune the light intensity and spectrum within the PBR.

The LED power supply **MEAN WELL HLG-120H-C1050B** has been used to dim the LEDs. An external module (MR-AO-1) connected with the PC supervisor carried out the power supply control. This module has four analog voltage outputs 0-10V, and the values of the output voltages can be set or read via RS-485, using the MODBUS RTU protocol. It is essential to underline that the LED drivers (**MEAN WELL HLG-120H-C1050B)** are voltage-controlled using the module (MR-AO-1). Meanwhile, the LEDs themselves are controlled in current by the LED driver.

Furthermore, each type of LED is connected with one module's output. As a result, the light intensity of each LED color can be controlled separately. Moreover, a different dimmer is used for the LEDs of the cover. This way, the user can choose if he wants to use only lateral illumination, only the illumination from the top of the PBR, or both of them.

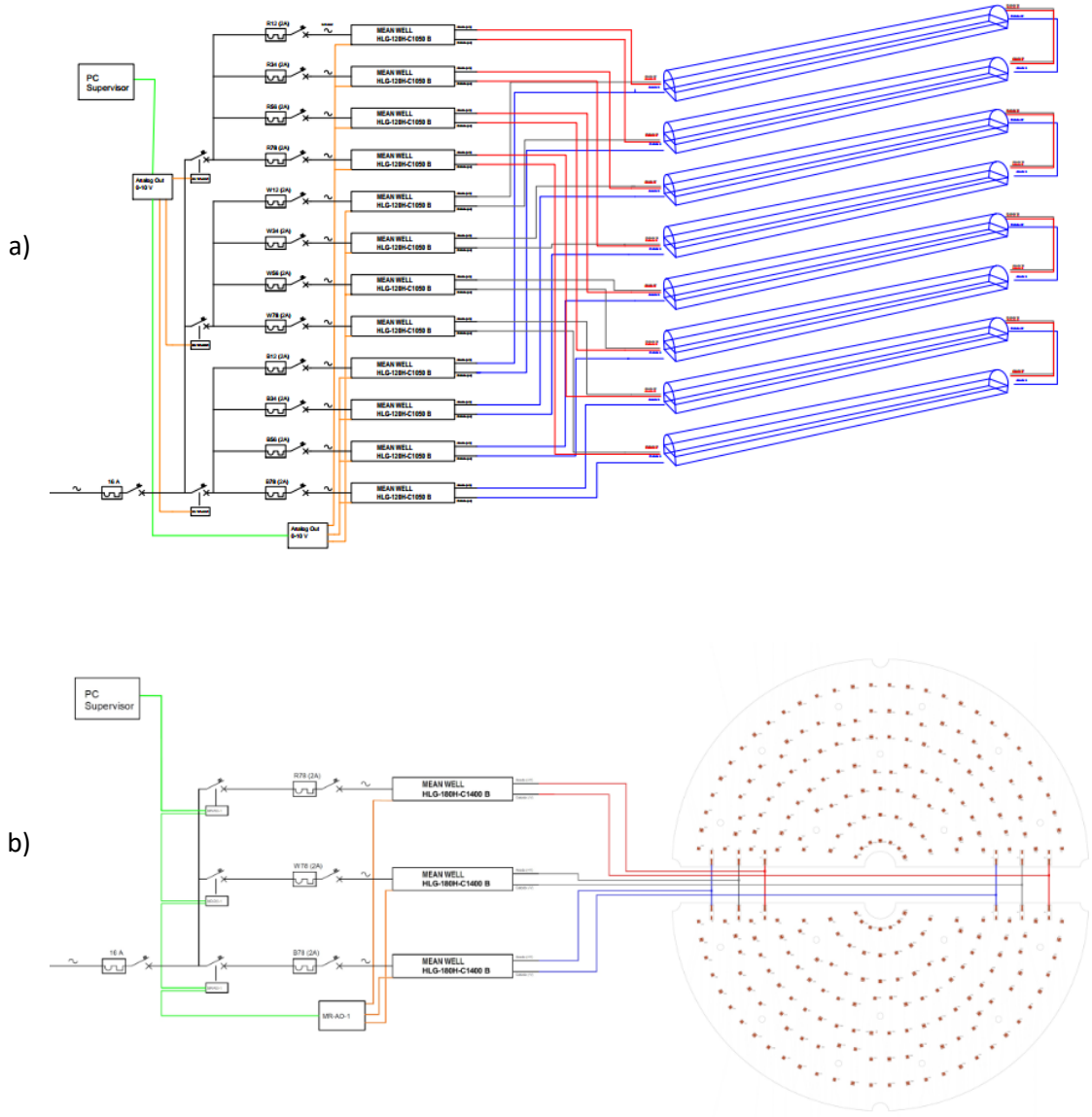

Figure 3-5: *a)Electric scheme of the connection of the LED bars to the LED power supplies, where red lines correspond to the powering up of the red LEDs, blue lines to powering up the blue LEDs, and the grey lines to the powering up of the white LEDs of each LED bar; b) Electric scheme of the connection of the LEDs of the cover*

3.2.3 Software for the control of the intensity of LEDs

The Photon Flux Density produced by the LEDs can be changed by commanding the dimmer connected to the power supply of the LEDs through a LabVIEW® software. As stated before, the communication protocol used is MODBUS RTU.

Two sensors, one facing the lateral LEDs and one facing the cover LEDs, are placed outside the liquid at the top of the PBR and are used to control the total lateral PFD and the PFD

from the top of the PBR. In principle, the user can acquire the desired PFD using the desired spectrum via this software. How does the algorithm for the control of the spectral light intensity work?

Practically, in the first place, it is initialized the communication with the module **(MR-AO-1)** and the optical sensors by setting their properties like the communication speed and the serial port. After that, inside a while loop, the commands are placed to read the PAR actual value by the sensors and the **MR-AO-1** module's output voltages. Based on the difference between the target PAR set by the user and the actual PAR read by the optical sensors, it is determined a multiplication coefficient is used to correct the output voltages of the **MR-AO-1** modules. It should be underlined that the user can choose between three different modes of illuminating the PBR: only cover LEDs, only lateral LEDs, both cover and lateral LEDs simultaneously.

The software is also equipped with a photoperiod option according to which the user can set the period when the PBR illumination is switched on.

The algorithm of light control of the PBR is described briefly in **Figure *3-6***

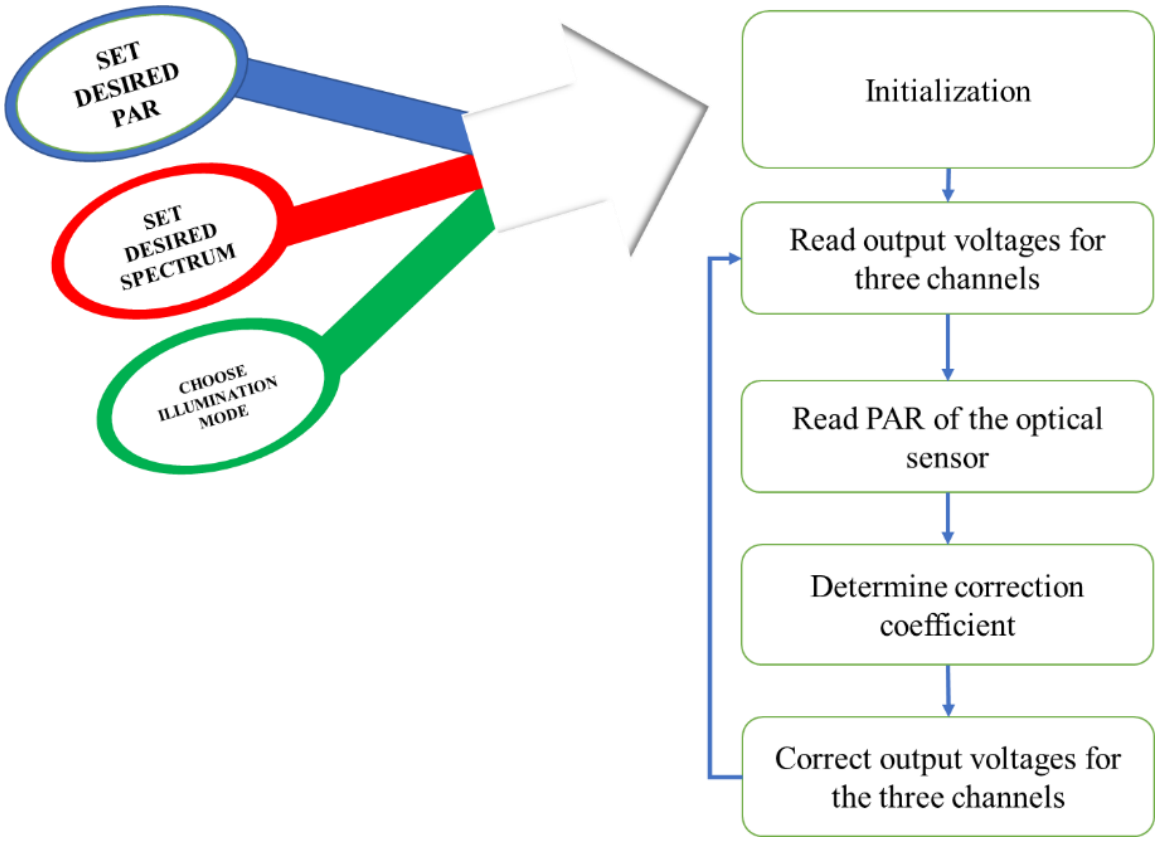

Figure 3-6: *Schematic representation of the algorithm for the control of spectrum light intensity inside the PBR*

Chapter 4

Simulation of light transfer within two photobioreactors of different geometries

We coupled an optimization algorithm with an optical simulation to simulate light propagation within the algal suspension. The optimization algorithm was used to determine the parameters of the algal suspension needed by the software to carry out the simulation. Based on the literature, the Henyey – Greenstein phase function was chosen to approximate the scattering phase function of the algal suspension and the ray trace software Zemax OpticStudio to simulate the light transfer within the two PBRs we described in chapter 3.

4.1 Zemax OpticStudio Software

Zemax OpticStudio is a ray–trace software that can model, analyze, and assist in designing optical systems. This software provides two types of ray tracing modes: sequential and non-sequential. During the sequential ray tracing, rays are traced from surface to surface in a predefined sequence, i.e., a ray will start at surface 0, then be traced to surface 1, then to surface 2, etc. Meanwhile, non – sequential ray tracing means that rays are traced along a physically realizable path. In this case, rays may strike any group of objects in any order or hit the same object several times.

In the case of the non – sequential mode, **Zemax OpticStudio** software provides several different objects, sources, and detectors that allow the user to design and simulate his optical system. Moreover, it also supports its programming language: Zemax Programming Language (ZPL), a macro language similar to BASIC programming language. So, if the user needs to perform a particular calculation or a graphical display that is not “built-in,” he can write his own *ZPL* macro.

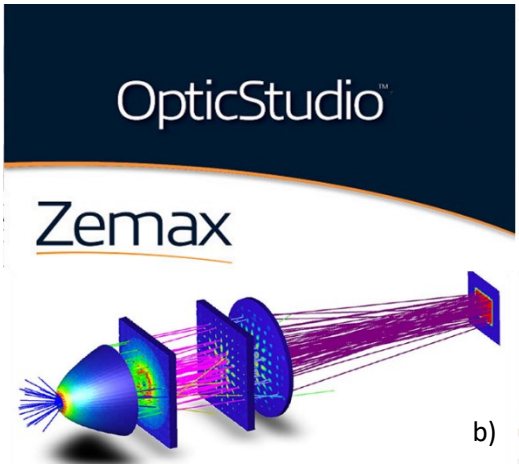

a)

b)

```
File  Modifica  Formato  Visualizza  ?
        VEC3 15, 0.961
        VEC3 17, 0.961
        VEC3 18, 0.961



        power_DETECTOR = 0.333

        SETNSCPARAMETER 1, 4, 4, wavenumber

FOR i, 1, 18, 1

        SETNSCPROPERTY 1, 9, 82, 0, VEC1(i)
        SETNSCPROPERTY 1, 9, 85, 2, VEC2(i)
        SETNSCPROPERTY 1, 9, 85, 1, VEC3(i)

        SETNSCPARAMETER 1, 4, 3, power_DETECTOR

        mf = MFCN()           # gives the value of merit function
        value3 = OPER(3,10)
        value4 = OPER(4,10)
        value5 = OPER(7,10)
        value6 = OPER(8,10)
        FORMAT 12.6  EXP
        PRINT wavenumber, " ",value3, " ",value4, " ",value5, " ",value6

NEXT
```

Figure 4-1: *a) Logo of Zemax OpticStudio software; b) Part of a macro written in ZPL*

This software offers the possibility of modeling the scattering of rays via an Angle Scattering model**.** According to this model, rays travelling a distance x within the medium have an integrated probability of having been scattered given by:

$$p(x) = 1 - e^{-\mu x}, \qquad 4\text{-}1$$

Where μ is the inverse of the mean free path in lens units (in this case, in mm).

However, if this model is insufficient, the user may create more complex bulk scattering functions via an external program called *Dynamic Link Library (DLL).* Some DLLs already provided by Zemax OpticStudio are: ***Poly_bulk_scat.DLL, Henyey-Greenstein-bulk.DLL, Rayleigh.DLL, Mie.DLL, Phosphor. DLL.*** Each of these DLLs requires specific parameters of the medium.

Henyey-Greenstein-bulk.DLL is the DLL we used to model the absorption and scattering by the algal suspension. As mentioned earlier, this model's choice was based on several studies [34,49]. To utilize this model, the user needs to provide the software with three parameters of the medium: *mean free path, transmission, and the asymmetry parameter of the Henyey – Greenstein phase function, g.* The following sections will explain how these parameters were determined in this work [138].

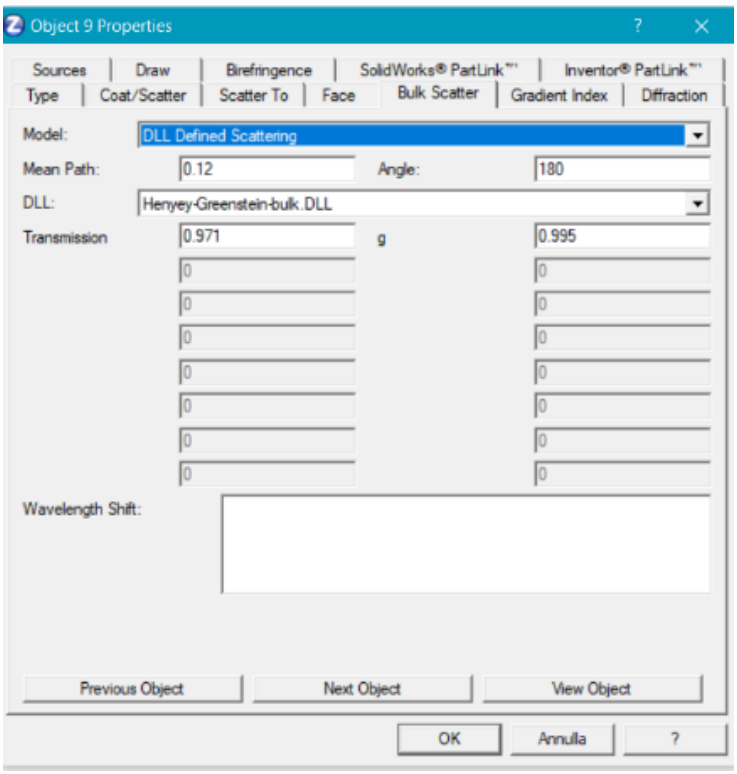

Figure 4-2: *Image is taken from Zemax OpticStudio Software with the parameters required from the Henyey-Greenstein phase function*

4.2 Determination of HG bulk scattering parameters

4.2.1 Microalgae strain and culture conditions

This study used the marine unicellular microalgae Nannochloropsis oculata that Biosyntex s.r.l, Imola, Italy supplied. *Nannochloropsis oc.* was cultivated in F medium using synthetic marine water (Top Mix Sea Salt), initially in 0.25-1 L flask and after in 0.5 and 1-L glass tubes with an enriched air carbon dioxide, 98%/2%; pH 7.80 at a temperature of 25°C. According to culture concentration, artificial light was maintained between 50 and 300 $\mu mol\ photons\ m^{-2}s^{-1}$ with a photoperiod of 12 h light:12 h dark cycle.

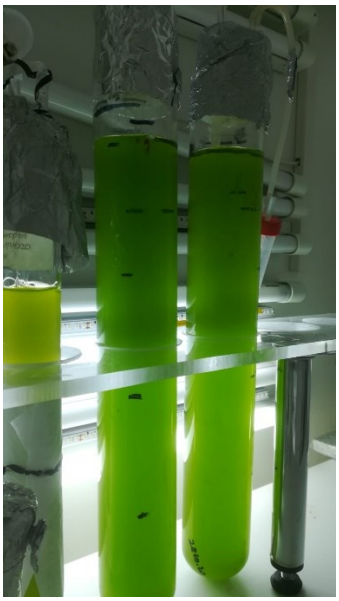

Figure 4-3: *Picture of the light tubes where the Nannochloropsis oculata used for the measurements was cultivated*

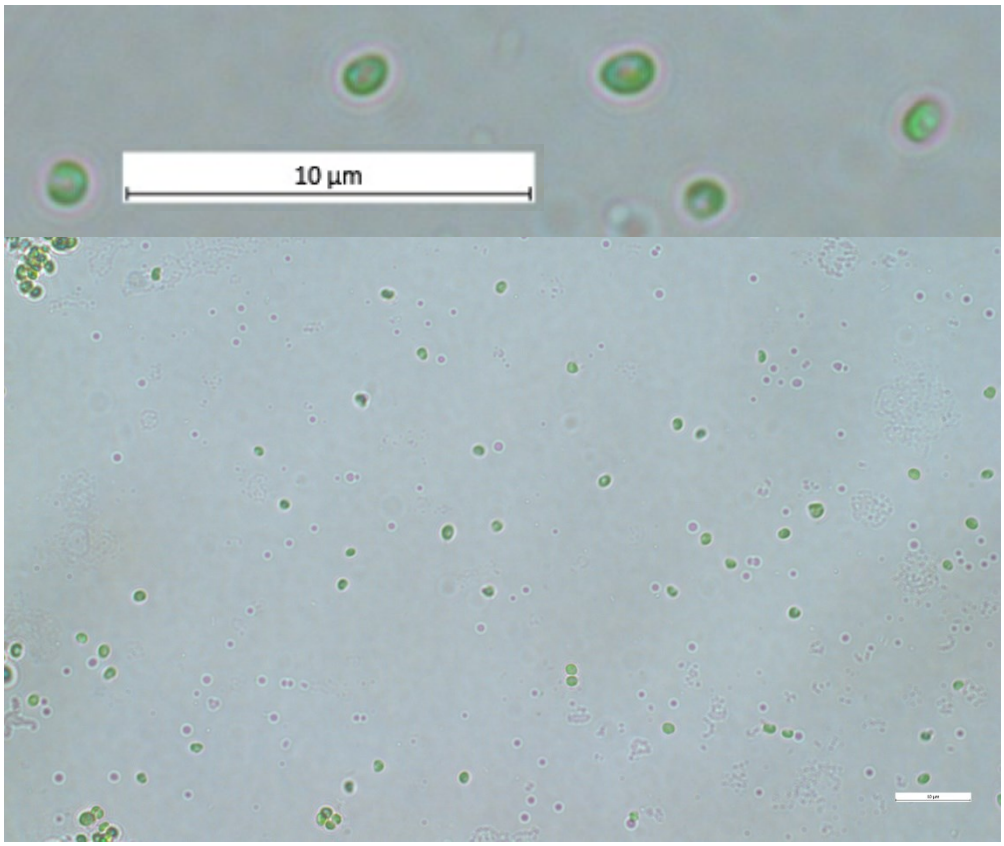

Figure 4-4: *Micrograph of Nannochloropsis Oculata*

The cell size distribution has been quantified using Image J's image processing and analyzing software. The software approximates the cells with an ellipsoid. On average, the minor diameter resulted in 1.393 μm, and the major diameter resulted in 1.73 μm with the standard

deviation respectively 0.19 μm and 0.2 μm. **Figure *4-5*** shows the number frequency of the major and minor diameters with bins of 0.1 μm in width.

a)

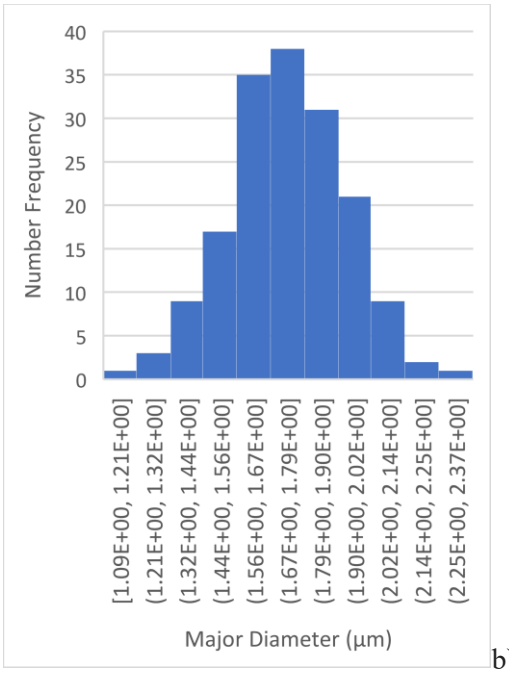

b)

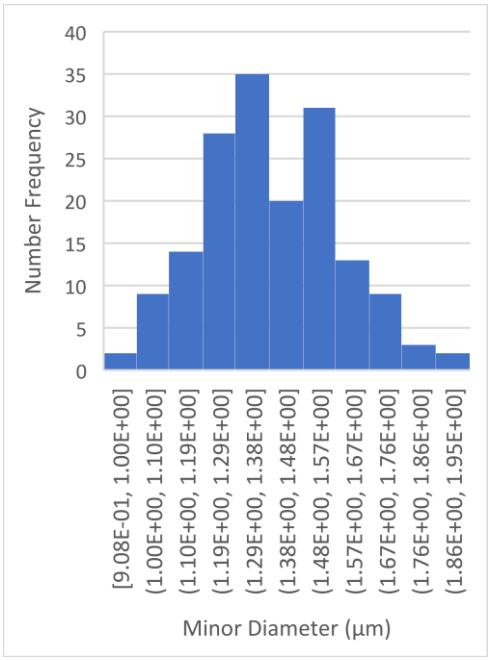

Figure 4-5*: Measured number frequency of the major and minor cell diameters for Nannochloropsis Oculata*

4.2.2 Description of the experimental measurements

To determine the HG bulk scattering parameters required to model the algal suspension with **Zemax OpticStudio** we used an integrating sphere (Labsphere 3P-GPS-033-SL) of diameter 4 inches coupled with the spectroradiometer (Ocean Optics USB4000-XR1-ES) to analyze the radiation scattered by the algal suspension. The light sources were six lasers: *Laser Diode Module 4.4 mW laser (Thorlabs CPS405)*, *Laser Diode Module 4.5 mW laser (Thorlabs CPS450), Laser Diode Module 4.6 mW laser (Thorlabs CPS520), Helium-Neon 5 mW laser (Melles Griot GreNe Laser), Helium-Neon laser five mW laser (Linos Photonics, P.N.040634),* and *Laser Diode Module 4.6 mW laser (Thorlabs CPS670F),* each providing a continuous laser beam, respectively, at the wavelength 401 nm, 456.7 nm, 523 nm, 543.5 nm, 632.8 nm, 675.7 nm.

In this work, we shined the light produced by the lasers onto a cuvette with microalgae suspension. The cuvette had a capacity of 4 ml and a thickness of 10 mm (cod. n. 67.745, Sarstedt). After being partly reflected, scattered, and absorbed from the cuvette with the algal

suspension, the laser beam was detected from an Integrating Sphere (IS). So, an integrating sphere, coupled with a spectroradiometer, which on the other hand was connected to the PC, was placed after the cuvette with the algal suspensions. The measurements we performed are normal-hemispherical measurements since light rays after the algal suspension enter inside the integrating sphere and get diffused due to the diffuse white reflective coating of the walls of the integrating sphere. Therefore, the detector, which detects the diffused light, is placed perpendicular to the light rays entering the IS.

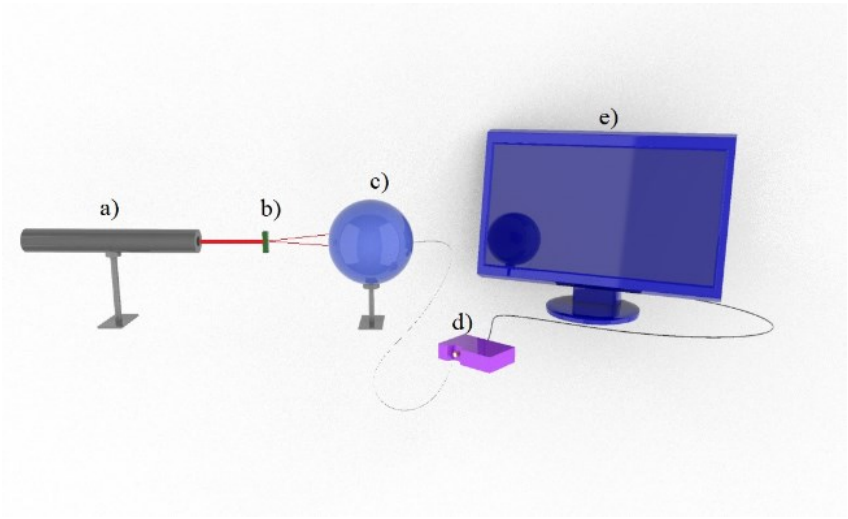

Figure 4-6*: Sketch of the experimental setup used to measure the transmitted light: laser (a), cuvette with microalgal suspension (b), integrating sphere (c), spectroradiometer (d), pc (e)*

We varied the distance between the cuvette and the entering port of the Integrating Sphere, measuring like this the transmitted power of light within different solid angles.

.

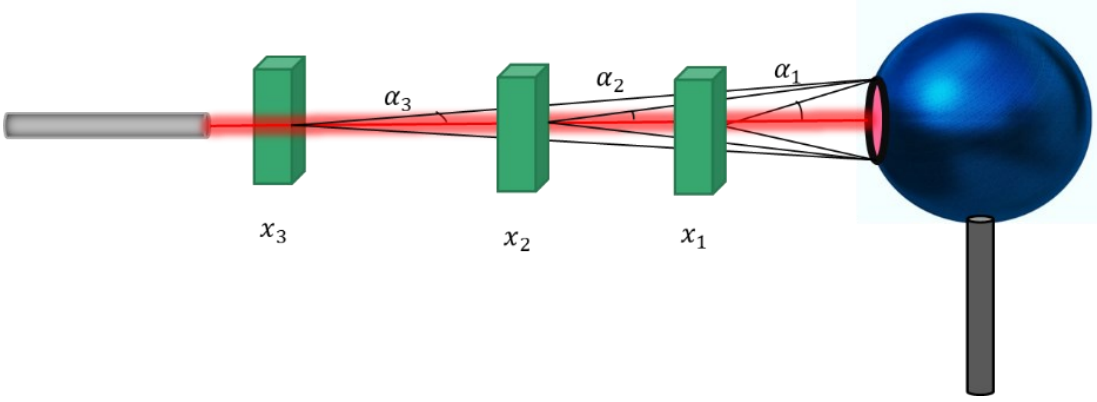

Figure 4-7: *Schematic representation of the cuvette positions (x1, x2, x3) with respect to the entering port of the integrating sphere*

This way, for each position x of the cuvette, we measured the power collected by the integrating sphere, $P(\alpha)$, within the corresponding solid angle:

$$\Omega = \int_0^{\alpha} 2\pi \sin(\alpha)\, d\alpha \qquad 4\text{-}2$$

Based on the literature [34,49], we choose the Henyey-Greenstein phase function to describe light scattering from the algal suspension.

But we must point out that what we measured from this experiment was not the HG phase function itself but the integral of the HG phase function. Indeed, the integral of the HG function would give the normalized scattered power as a function of the polar angle α:

$$HG_{int}(\alpha) = \int_0^{2\pi} \int_0^{\alpha} g(\alpha) sin\alpha \;\; d\alpha \;\; d\varphi = \frac{g^2-1}{2g} \left(\frac{1}{\sqrt{1+ g^2 -2gcos\,\alpha}} + \frac{1}{1-g} \right) \qquad 4\text{-}3$$

Properties of Equation 4-3: $HG(0) = 0$ and $HG(180°) = 1$.

We carried out the experiment described in this section for six different wavelengths of the source of light impinging in the cuvette with the algal suspension and for six different concentrations of the suspension: 0.21 g/l, 0.34 g/l, 0.62 g/l, 0.77 g/l, 0.96 g/l, and 1.26 g/l. The measurements of the transmitted power were taken for 18 different distances of the double cuvette – IS. Depending on these distances, the angle α took values that varied from 5° to 89.9°.

During the experiment, we periodically mixed the suspension to avoid sedimentation. Therefore, we assumed that the microorganisms were well mixed and randomly oriented in the data analysis.

4.2.3 Determination of Henyey-Greenstein bulk scattering parameters within Zemax OpticStudio software

The experiment described in paragraph 4.2.2 has been simulated via the Optical Design Program, **Zemax OpticStudio.**

We modeled the laser with a *Source Ray. A Source Ray* is a point that emits rays along specified direction cosines [138]. The power and the wavelength of the light emitted by the *Source Ray* were set according to the laser's power and wavelength in the experiment we were simulating.

The cuvette with the algal suspension was modeled with a *Rectangular Volume,* a six-sided solid for which the user can determine its dimensions and the material. Its dimensions were set equal to the dimensions of the cuvette: *(10 × 10 × 45) mm*. Meanwhile, the material of the *Rectangular Volume* was chosen *Sea Water,* and its transmission values were calculated from the absorption coefficients of the *Sea Water* provided by the *Handbook of Optics* [139]. The bulk scattering from the algal suspension, as mentioned earlier, was modeled utilizing the DLL in the **Zemax OpticStudio** package: ***Henyey-Greenstein-bulk.DLL.***

The entry port of the integrating sphere has been modeled with a *Detector Surface*, an object that stores energy data from NSC source rays that strike it. Its dimensions were set equal to the dimensions of the IS aperture, and its material was chosen transparent. The number of the *Detector Surfaces* set in the simulation was equal to the number of different positions of the cuvette with algal suspension with respect to the aperture of the IS. They were placed so that the distance between them and the *Rectangular Volume* was equal to the distance cuvette – IS during the measurements.

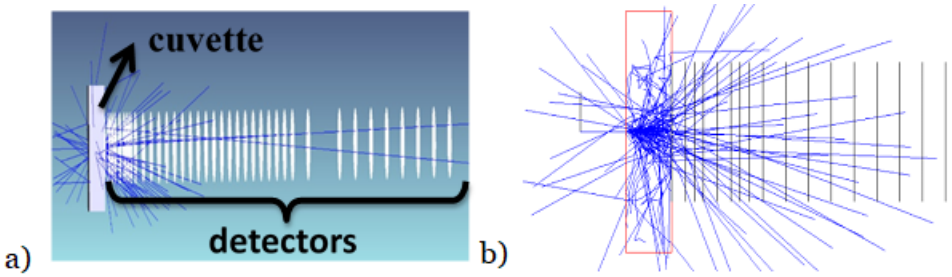

Figure 4-8*: Shaded model of the simulation, where it is represented the cuvette and the detectors placed at specified distances from the cuvette. b) The 3D Layout of the simulation represents the scattered rays from the microalgal suspension and the detectors used to determine the parameters of the model.*

Before running the simulation, we needed to set the parameters of the HG bulk scattering model for the algal suspension for which we took the measurements: *Mean Path*, *Transmission,* and *asymmetry parameter, g*. On the other hand, these are precisely the parameters that we intended to determine via this method. For this purpose, we wrote a Macro to variate the bulk parameters, and via an optimization method, we chose the triplets that best described the measured data. Based on the literature, the asymmetry parameter for the algal suspension is characterized by values greater than 0.97 [33,34,140,141]. For this reason, while variating the parameters, for g, it was set the constrain $0.96 < g < 1$. On the other hand, it is important to underline that mean path and transmission don't represent the

true physical values of the algal suspension, but the triplet (*Mean Path*, *Transmission,* and *asymmetry parameter, g)* model very well the absorption and scattering of light from the algal suspension.

The number of *Analysis Rays* during the simulation was set 10^5 rays.

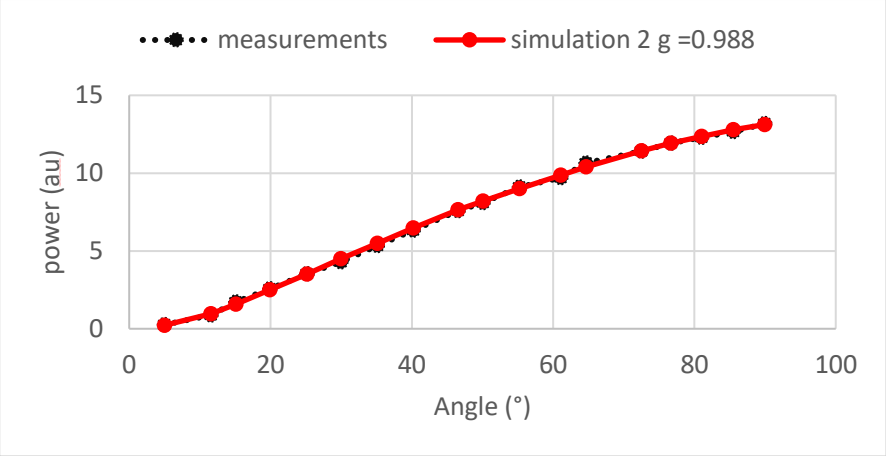

Figure 4-9: *Plot of the transmitted power as a function of the polar angle: the measured data (black) and simulated data (red). The wavelength of the source* $\boldsymbol{\lambda}$ *= 543 nm and the concentration of the suspension 0.77 g/l. The parameters of the bulk scattering that lead to these results are g = 0.988, mean free path 0.23 mm, and transmittance 0.995.*

Figure 4-9 shows the measured power transmitted from the cuvette with the algal suspension as a function of the polar angle (black) and the simulated transmitted power (red) using the HG bulk parameters determined via the optimization method.

This figure shows a very good agreement between the transmitted power measured experimentally and the transmitted power simulated *on* **Zemax OpticStudio** (MAPE 3.07 %).

4.2.4 Validation of the method

We conducted a second experiment to validate the method we used to determine the HG bulk parameters that we will use to simulate the spectral distribution of light within a PBR containing the same sample of algal suspension we analyzed. For this reason, we measured the transmitted power from an algal suspension (the same for which we determined the HG bulk parameters earlier) of 34 mm thickness.

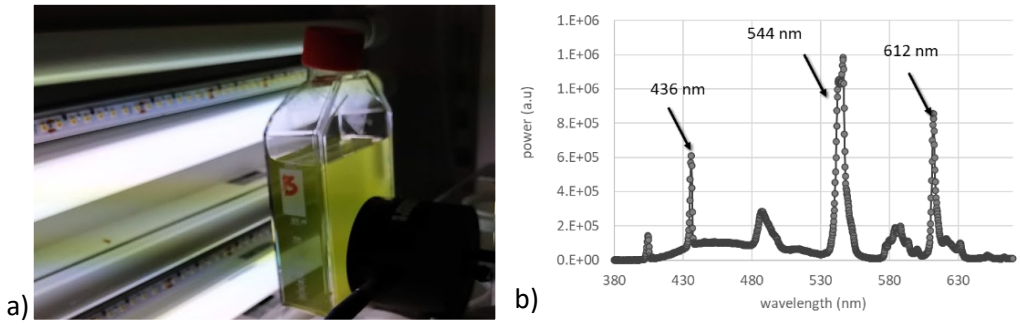

Figure 4-10: *a) Measurements of light transmitted from a 34 mm thick flask filled with algal suspension; b) Spectrum of the incident light in the algal suspension*

On the other hand, this exact situation was simulated via **Zemax OpticStudio** software, utilizing HG bulk scattering with the parameters we have already found, as described in paragraph 4.2.3.

The light source used in this experiment was a Neon Tube, whose spectrum is shown in **Figure 4-10**. As can be seen from the figure, the spectrum is characterized by three peaks at the wavelengths: 436 nm, 544 nm, and 612 nm. Meanwhile, the HG bulk parameters were determined for 456 nm, 543 nm, and 633 nm. As a result, the comparison between the simulation and the measurement was made for these three sets of wavelengths: blue (436 nm vs. 456 nm), green (544 nm vs. 543 nm), and red (612 nm vs. 633 nm). Figure 4-11 shows that the measured data fall within the error bars of the simulated data.

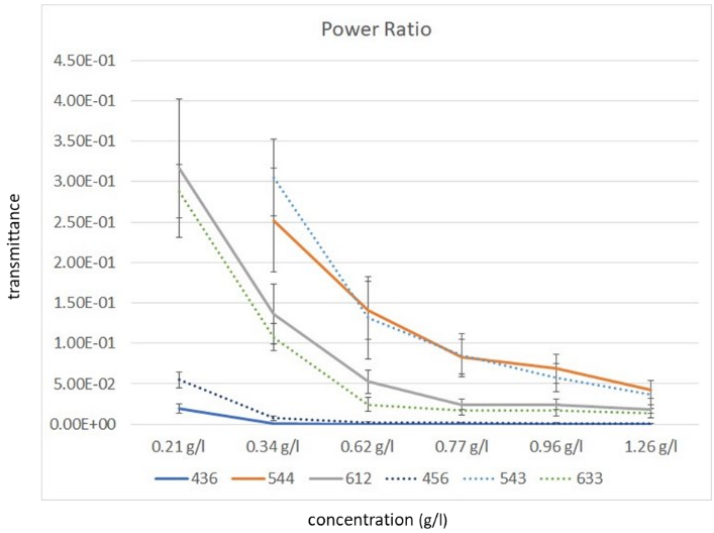

Figure 4-11: *Transmittance from an algal suspension of 34 mm thickness for different concentrations: solid lines (436 nm, 544 nm, and 612 nm) correspond to the measured data; dashed lines (456 nm, 543 nm, and 633 nm) correspond to simulated data.*

This result has been considered satisfying, and thus we followed this approach to model our photobioreactors.

4.3 Application of the simulation model to the PBR

4.3.1 Annular PBR

In the simulation, the construction of the PBR was done using objects of type *Cylinder Volume* and the *Boolean* operation of subtraction. As the name indicates, a *Cylinder Volume* is a rotationally symmetric volume defined by three parameters: the radius of the front circular face, the radius of the rear circular face, and the cylinder's length [138]. To this extent, we subtracted two *Cylinder Volumes* to create the inner tube and another two *Cylinder Volumes* to create the outer tube of the PBR. The dimensions of the *Cylinder Volumes* were set according to the dimensions of the annular PBR, and the material was chosen polymethyl methacrylate (PMMA), supported by the software. A fifth *Cylinder Volume* was used to model the algal suspension. As previously described, the material of the last *Cylinder Volume* was chosen Sea Water, and the transmission was calculated based on the absorption coefficients of the sea water found in the Handbook of Optics [139]. The scattering of light by algal suspension was modeled via the ***Henyey-Greenstein-bulk.DLL*** with the bulk parameters determined as explained in section 4.2.3.

The LEDs placed around the PBR were simulated by a source of type *Source Two Angle,* which may be a rectangular or elliptical surface that emits light into a cone with distinct angles in the X and Y directions [138]. We chose a rectangular spatial shape for the source, with dimensions equal to the ones of the LEDs: (1.35 x 1.35) mm for white and red LEDs and (0.75 x 0.83) mm for the blue LED. To set the properties of the *Source Two Angle* for each type of LED, we run several simulations to have the radiation pattern characteristics (normalized radiant power as a function of angle) of the simulated source similar to the ones of the LEDs. We chose an elliptical angular distribution with the angular distribution of rays uniform in angle space. Moreover, we set the X half-angle (the half-angle of the cone of rays in the XZ plane) and the Y half-angle (the half-angle of the cone of rays in the YZ plane) equal to 58° for the white and red LEDs as a similar radiation pattern characterizes them. We set the X half-angle and the Y half-angle equal to 68° for the blue LED. The power was set accordingly to the power of each LED.

The spectrum of the white LEDs was built by weighting the six laser wavelengths for which the HG bulk parameters were determined.

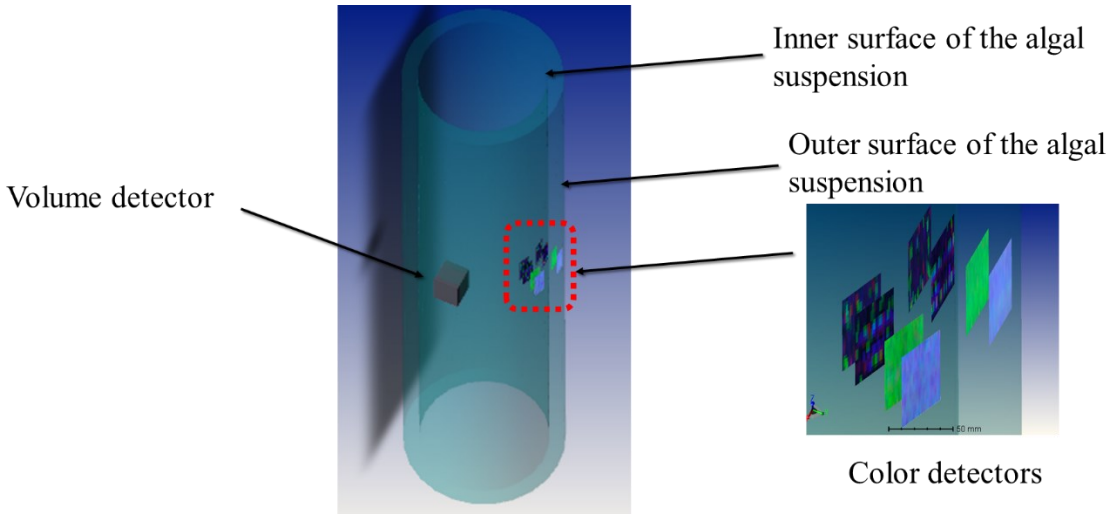

Figure 4-12*: Shaded model of the annular photobioreactor simulated*

We placed the first *Rectangular Detector* in air, 5 mm from the outer tube of the PBR, and the other detectors were placed within the algal suspension, at 5 mm from each other.

In **Figure *4-13*** is represented the photon flux density (PFD) as a function of the position for three different concentrations of the algal suspension: 0.34 g/l, 0.62 g/l, and 1.26 g/l. The value zero in the x-axis corresponds to the position of the PBR surface, and the negative value means the detector is placed in air, 5 mm away from the outer tube of the PBR. As the distance from the outer tube increases, the PFD decreases due to absorption. Furthermore, the rate of the decrease is faster for higher concentrations. These considerations are well-known and serve as a confirmation of the model's validity.

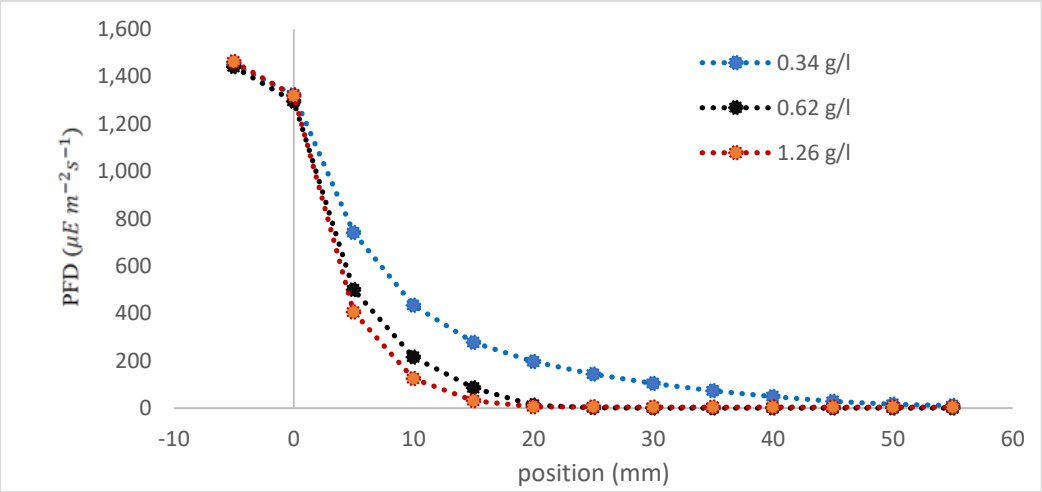

Figure 4-13: *PFD at different positions within the algal suspension for three different concentrations: 0.34 g/l, 0.62 g/l, 1.26 g/l*

Meanwhile, **Figure *4-14*** is shown the PFD, at different positions within the algal suspension, for six different wavelengths of the PAR, for a concentration of 0.34 g/l. It can be noticed that the initial number of the "blue" and "red" photons is greater than the number of "green" photons.

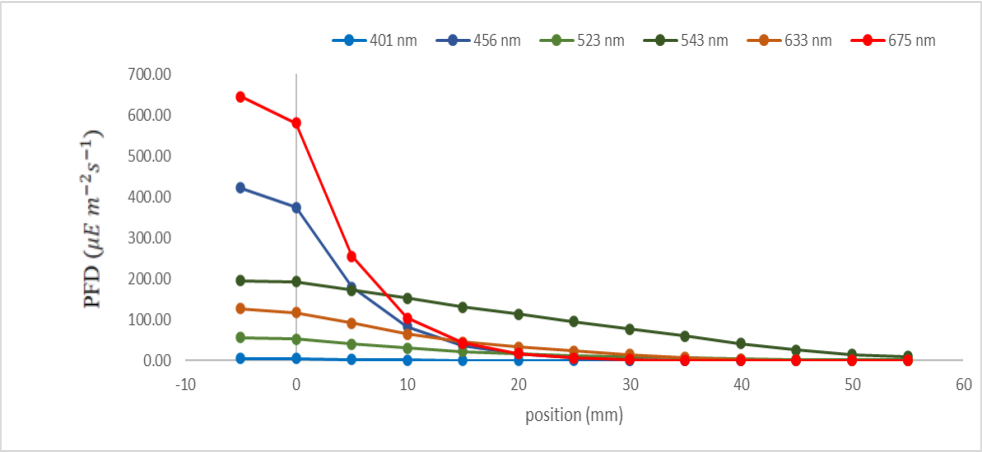

Figure 4-14: *The PFD for different wavelengths at different positions within the algal suspension. The concentration of the suspension during the simulation was 0.34 g/l.*

Moreover, the photon flux decrease rate with the increase of the distance from the outer tube of the PBR is greater for the wavelengths 675 nm and 456 nm than the other wavelengths. Therefore, we calculated the gradient of the decrease of the photon flux for the wavelengths 456 nm, 543 nm, and 675 nm representing the blue, green, and red parts of the PAR spectrum.

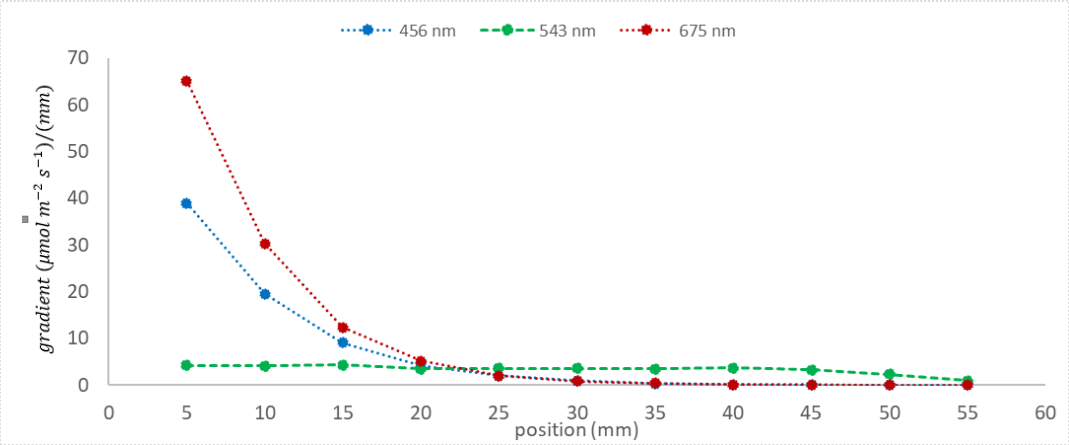

Figure 4-15: *Plot of the gradient of the decrease of the PFD within the algal suspension with the increase of the distance from the LEDs.*

The results in **Figure *4-15*** are consistent with the higher absorption coefficient of red and blue bands meanwhile, and green light features a lower absorption [141].

The change of the spectrum's shape of the light source within the algal suspension was also reported by [28,44].

Zemax OpticStudio software allowed us to visually investigate the change of the shape of the light spectrum during propagation within the algal suspension by using detector colors. These detectors can accurately display the color of the illumination. We placed four detector colors: detector one is placed in the air, 5 mm from the outer tube of the PBR, detector two is placed within the algal suspension, 5 mm from the outer tube of the PBR, detector three is placed within the algal suspension 5 mm from the inner tube of the PBR. Meanwhile, detector four is placed in the air, 5 mm from the inner tube of the PBR.

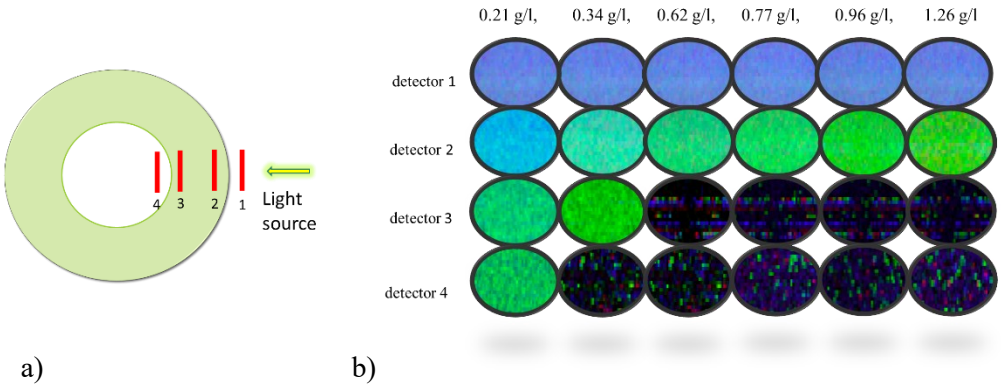

a) b)

Figure 4-16: *Detector colors to investigate the change of spectrum within the algal suspension visually: a) a schematic cross-section of the PBR where is also shown the position of the detectors, b) The color detectors at different concentrations of the algal suspension within the PBR*

The incident light on the outer tube of the PBR is provided by blue, red, and white LEDs simultaneously. As a result, the detectors placed in the air, just in front of the outer tube of the PBR, show a light blue color.

In the case of low concentrations, for example, 0.21 g/l, detector 2 shows a light blue color meanwhile detector 3, which is positioned deeper within the algal suspension, shows a green color. This evidences the fact that in the position of the detector 3 prevail green photons. Meanwhile, the photons corresponding to red and blue wavelengths have already been absorbed.

For higher concentrations, for example, 0.96 g/l, detector two placed 5 mm within the algal suspension shows a green color. So, blue and red photons are absorbed within 5 mm inside the algal suspension. On the other hand, detector three shows a black color which signifies the absence of photons.

From examining the detector colors, we concluded that green photons could travel deeper within the algal suspension without being absorbed, which agrees that the blue and red photons are characterized by higher extinction coefficients [141].

4.3.2 Multiple–tube PBR

The model, which calculates the spectral distribution of light within an algal suspension, was also applied to the multiple–tube PBR described in Chapter **3**. The first step in simulating light propagation within this PBR was building its model in **Zemax OpticStudio** software.

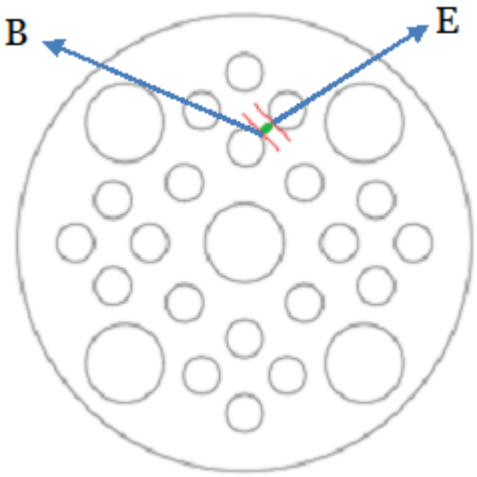

Figure 4-17: *The cross-section of the simulated photobioreactor.*

As also described in the simulation of the annular PBR, the algal suspension is modeled by a *Cylinder Volume* of radius 550 mm and of height 100 mm. The height of the simulated PBR was set not equal to the real height of the PBR because the light tubes provide a uniform illumination along the z-axis. On the other hand, this choice would decrease the number of calculations and as a result, also the simulation time. The material of the *Volume Cylinder* was set Sea Water, with the appropriate absorbing coefficients. The scattering and absorption from the algal suspension was modeled via the *Henyey-Greenstein-bulk.DLL.*

The light tubes were simulated using *Source Tube* objects which emit rays from the surface, and their power was set accordingly to the power at the surface of the tubes in the real situation.

In **Figure 4-18** is represented the photon flux density (PFD) at different positions between the points (B) and (E) (which are found on the surface of two light tubes) for different concentrations. As the distance from the light tube increases, the PFD decreases due to absorption. Furthermore, the rate of the decrease is faster for higher concentrations.

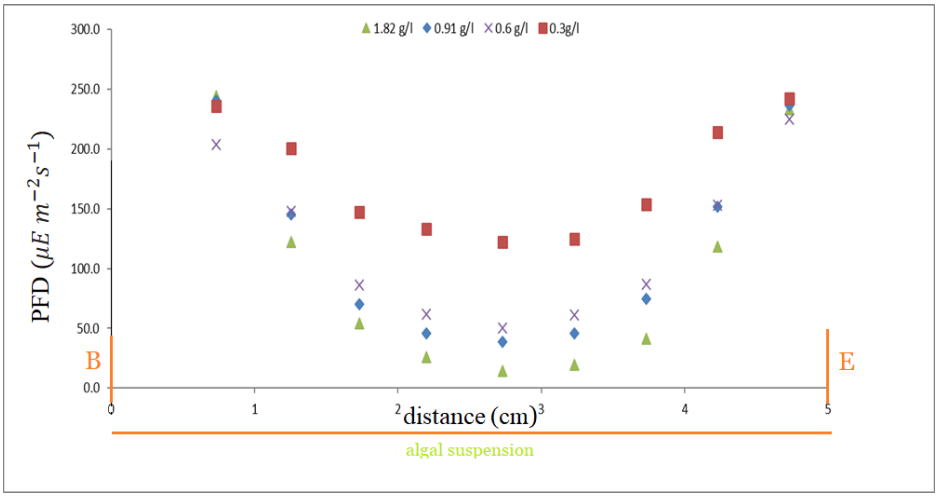

Figure 4-18: *PFD at different positions between points B and E within the photobioreactor for different concentrations.*

Meanwhile, in **Figure *4-19*** is shown the PFD, at different positions between points (B) and (E), for different wavelengths, and for an algal suspension of concentration 0.9 g/l.

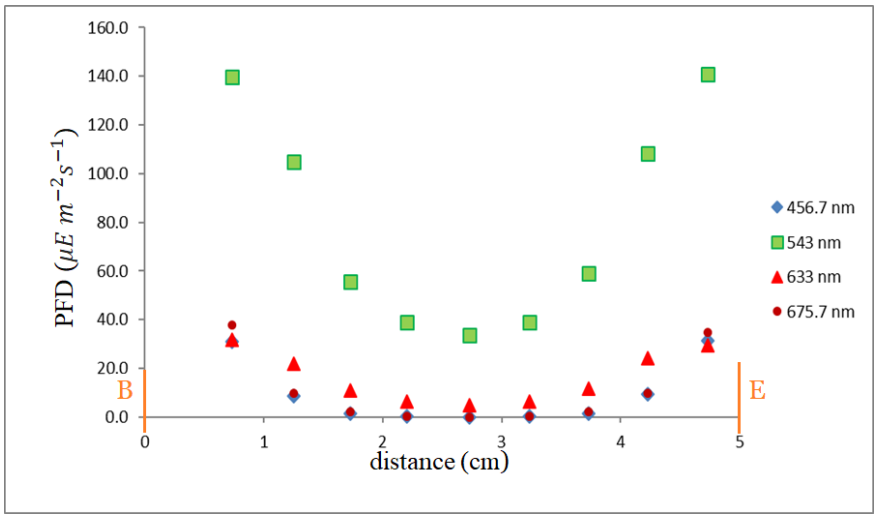

Figure 4-19: *The PFD for different wavelengths between points (B, E). The concentration of the solution during the simulation was 0.9 g/l.*

These results are consistent with the higher absorption coefficient of red and blue bands than green bands.

In conclusion, both simulations show that with the increase of concentration, the decrease of the light intensity within the algal suspension is higher. In addition, the red and blue photons are characterized by a faster absorption compared to green photons. However, green photons become important for the photosynthesis process in case of very high concentrations since they get absorbed too, and according to Emerson and Lewis [142], the drop of quantum yield for *Chlorella* (green microalgae), from red to green wavelength is from 0.09 to 0.066, so less than 30 %.

In the following chapter, after having introduced the floating sensor FloSen, we will turn back again to the results of this model as we will compare them with its measurements.

Chapter 5

Floating Sensor, FloSen

To ensure a high growth rate of the algal cells, the quantity and quality of light should be within appropriate levels at every point of the PBR. Until now, there have been developed sensors to monitor in real-time the turbidity or the concentration of the algal suspension [143,144]*, but not the light intensity. We designed a sensor that can float freely within the algal suspension to match this requirement, providing real-time information on the spectral irradiance, optical density, and the 3D position where the measurement was taken.*

5.1 FloSen, general description

The first prototype of the sensor has a cylindrical shape with a diameter equal to 24 mm and a height equal to 36.4 mm. FloSen is composed of two main boards connected with each other: the sensor's board and the power supply board.

On the power supply board is mounted a rechargeable Li-ion battery **(LP301012 031012)** with a capacity of 30mAh, four PV cells used to recharge the battery and a Low-Dropout Linear Regulator (LDO) used to provide a constant voltage of 2.5 volts to the main board.

On the main board are mounted four optical sensors (two on each side), a photo microsensor, a magnetometer, a Bluetooth module, and a microcontroller. The microcontroller, **PIC16(L)F18446,** is used as a signal processing and control center. The optical sensors are digital RGB sensors **(APDS-9253-001),** which measure light intensity in four bands of the light spectrum centered at 465 nm, 525 nm, 625 nm, and 850 nm. The Bluetooth module **(2608011024010_Proteus_II)** provides a point–to–point communication between the sensor and a PC supervisor. Meanwhile, the magnetometer **(LSM303D)** will

measure the magnetic field used to determine the position of the sensor inside the photobioreactor (PBR).

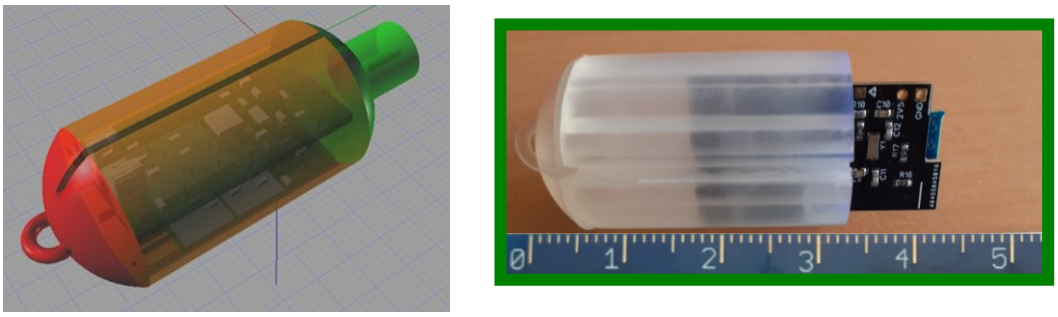

Figure 5-1: *The design of the PCB board inside its case (left) of the first prototype of FloSen; The picture of the PCB board of the first prototype of FloSen inside the transparent case*

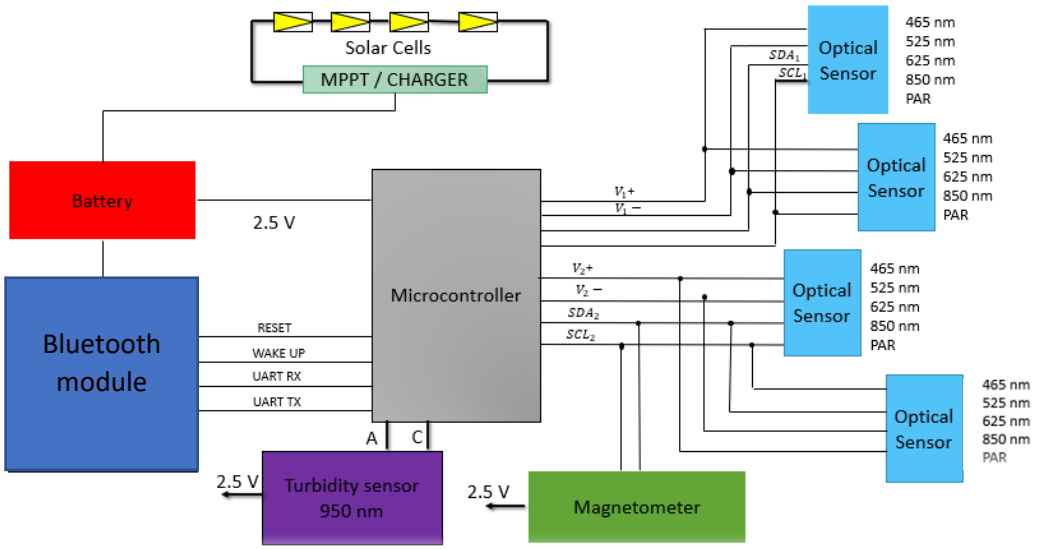

Figure 5-2: *The block diagram of the first prototype of the sensor*

The most important feature of this sensor is that it is designed to float freely inside the suspension and its position will be determined via a localization method.

The localization of the sensor is based on the measurement of a non-uniform magnetic field generated by a set of coils powered by a direct current.

A newly developed algorithm accomplishes the localization of the sensor based on a map connecting the hyperspace of the magnetic field measured from every single coil and the physical position of the sensor within the photobioreactor.

5.1.1 Optical sensors

As mentioned earlier, the optical sensor used to measure the spectral light intensity within the PBR is the digital RGB Sensor in a miniature package, having a length equal to 1.7 mm, width equal to 1.3 mm, and height equal to 0.6 mm. It can be configured as an Ambient Light Sensor (ALS) or as RGB+IR Sensor, as it uses four individual channels of red, green, blue, and IR.

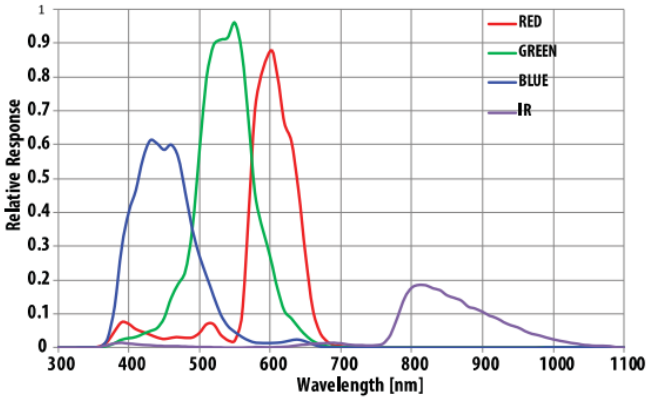

Figure 5-3: *Spectral response of the optical sensor (APDS-9253-001) [145].*

The sensor acquires a supply voltage in the range of 1.7 V to 3.6V, which is compatible with an I^2C interface. Moreover, it is characterized by a programmable integration time with a minimal value of 3.125 ms, a typical value of 50 ms, and a maximum of 400 ms.

Before choosing the APDS optical sensor, we carried out a few calculations to determine if the sensor would saturate in real conditions within a PBR. We wanted to calculate the number of counts that the sensor would measure for different integration times when the PFD was 500 $\frac{\mu mol\ photons}{m^2 s}$.

We supposed that the natural light collected by the Solar Lens Panels described in Chapter **2** was used to illuminate the photobioreactor, which on the other hand, was supposed to be a bubble column PBR, with a radius equal to 250 mm and height equal to 2000 mm. The spectrum of light out of the plastic optic fibers, measured in a day when the Direct Normal Irradiance (DNI) was equal to 659.4 $W/m^{2,}$ is shown in **Figure *5-4***.

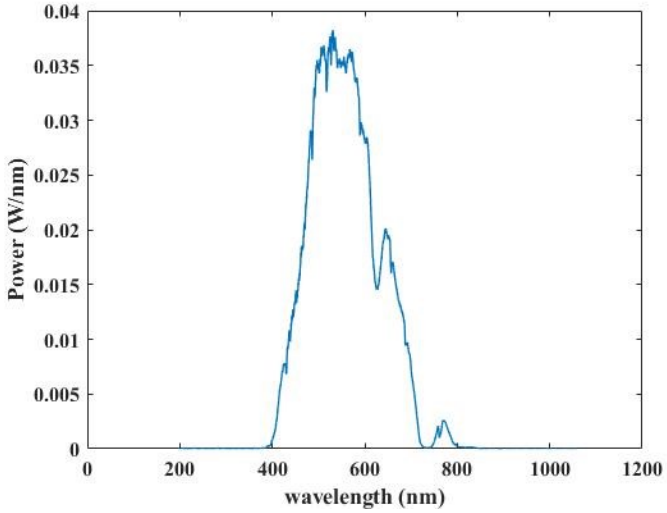

Figure 5-4: *Power out of the plastic optical fiber, collected by the Solar Lens Panel, DNI: 659.4 W/m²*

To this extent, we calculated the number of Plastic Optical Fibres needed to have 500 $\frac{\mu mol\ photons}{m^2 s}$ incident photons were 46. By multiplying the number of POFs with the spectrum of one POF and with the spectral response of the sensor for each channel, we found that the sensor would see a power equal to 2511 $\mu W/cm^2$ (125 $\frac{\mu mol\ photons}{m^2 s}$) in the red channel, 4573 $\mu W/cm^2$ (206 $\frac{\mu mol\ photons}{m^2 s}$) in the green channel and 1570 $\mu W/cm^2$ (63 $\frac{\mu mol\ photons}{m^2 s}$) in the blue channel. Using each channel's sensitivity for an integration time of 50 ms, reported from the datasheet of the sensors, we calculated the number of counts that would register each channel in these conditions as a function of the integration time.

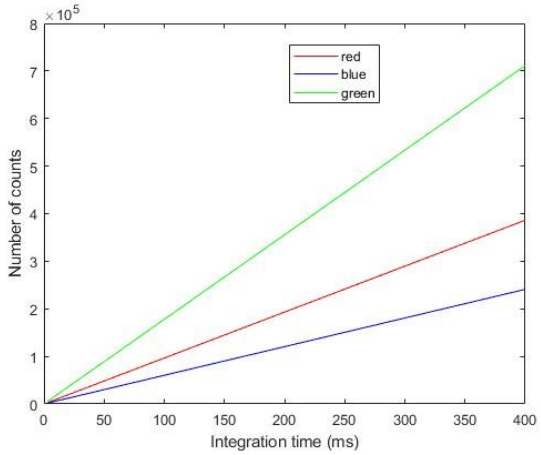

Figure 5-5: *Number of counts seen from each channel as a function of the integration time, for the light conditions explained in section 5.1.1*

The maximum resolution the user can choose for each channel is 20. As a result, the maximum number of counts each channel can read is 2^{20} = 10.48576 x 10^5 counts. Comparing this number with **Figure *5-5*** we can conclude that none of the channels saturate in the studied situation. Consequently, this sensor can be used for our purpose.

5.1.2 Photo microsensor

The photo microsensor is composed of an emitter which is an LED emitting light at 940 nm, and a detector to detect the emitted light. In the role of the detector is a phototransistor. The slot between the emitter and the detector has a width equal to 4 mm. To this extent, the light detected by the detector will decrease due to the algal suspension within the slot. The greater the algal suspension's optical density, the smaller the light intensity detected by the detector. The calibration of the photo microsensor will be shown in Chapter 6.

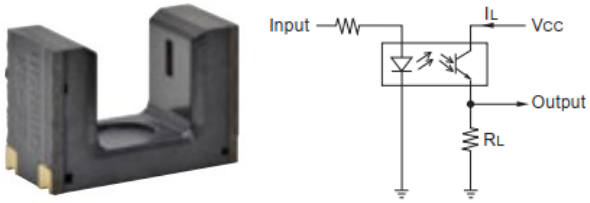

Figure 5-6: *Picture of the photo microsensor (left); Schematics of the photo microsensor (right) [146].*

5.1.3 Bluetooth module and Bluetooth Evaluation Board

The Bluetooth module (Proteus II) is a of type Bluetooth Low Energy 5.0 with a transmission velocity of 2 Mbit/s. It transmits the data in the ISM band 2.45 GHz and uses the UART serial interface.

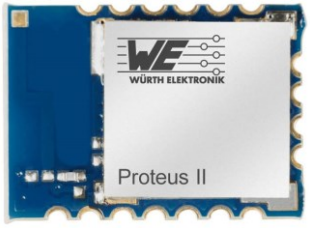

Figure 5-7: *The Bluetooth module (Proteus II) used in FloSen sensor*

In this project, we transmit the data from the Bluetooth (BT) module embedded in the PCB of FloSen to the *Evaluation Board*. The *Evaluation Board* is a board equipped with a BT module and can be connected to a PC's USB port. After being sent to the Evaluation board via BT communication, the data are transmitted via the serial port to the PC supervisor.

Figure 5-8: *Picture of the Evaluation Board*

5.2 The circuit of the sensor

In **Figure *5-9*** is represented the schematic circuit of the power supply Printed Circuit Board (PCB). Its main electronic components are an array of four PV cells (8x8) mm connected in series, a low power, low voltage, monolithic step-up converter (SPV1040), and a low-dropout, low-power linear voltage regulator (LDO). The choice of the LDO instead of a step down converter is done due to the small dimensions of the sensor's PCB. The charging of the battery is done by the solar cells via the booster converter, which steps up the voltage from its input to its output. The efficiency of SPV1040, in terms of power harvested from the cells and transferred to the output, is maximal in different environmental conditions due to the embedded MPPT algorithm.

Let's try to understand the function of the elements of this circuit. The capacitor's C1 role is to reduce the input voltage ripple. For the same reason, to reject the noise on MPP-SET input voltage, near this pin is placed the capacitor C2.

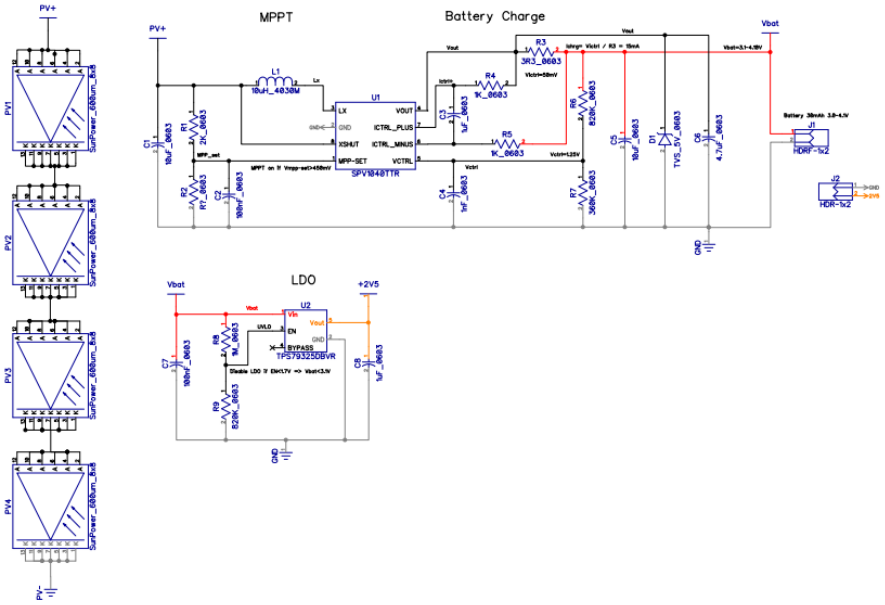

Figure 5-9*: Scheme of the electronic circuit of the power supply*

Xshut is an analog input, which shuts off all the internal circuits when it is low (smaller than 0.27 V). Since we connected this pin directly to the input voltage, it is evident that when the input voltage is smaller than 0.27 V, the circuit of the boost converter will be shut off. MPP-SET is an analog input that is connected to the input voltage via a divider of resistors, and its role is to track the MPPT of the cells. The inductor L2 makes possible the voltage step up. R3 is a resistor placed between the two analog input pins, ICTRL_PLUS and ICTRL_MINUS, in the output rail. Its function is to sense the output current flowing toward the load. Near to the input of these pins, a filter is placed to filter the noise, which is composed of the resistors R4, R5, and the capacitor C3. The capacitor C4 is placed near the analog input VCTRL to reject the noise sensed by this pin. The SPV1040 is a monolithic, high efficiency, low voltage, self-powered DC-DC converter that operates over a 0.3 V to 5.5 V DC input voltage range and provides a single output voltage. The device provides regulated output voltage and current by sensing the VCTRL feedback of the external resistor divider and the voltage drop on the external sense resistor Rs, respectively. The capacitors C5 and C6 are output capacitors placed to reduce the voltage ripple in the output. Meanwhile, the diode is placed to protect the load if the PV cell provides a current $I_{MP} > 0.5$ A.

In **Figure *5-10*** is represented the schematic circuit of the main PCB of the sensor. Its main components are the microcontroller (**PIC16(L)F18446),** four optical sensors **(APDS-9253-001), and** the Bluetooth module **(2608011024010_Proteus_II),** the turbidity sensor **(EE-SX1340),** and the magnetometer **(LSM303D).**

The microcontroller is of 8 bits, has 21 pins, and offers a low power mode. The microcontroller is powered by the power supply board with a voltage of 2.5 V, regulated by the LDO. Near to the input pin of the power-up of the microcontroller is placed a decoupling capacitor, C9.

The optical sensors have an I^2C interface, so they communicate with the microcontroller via I^2C communication. There are four optical sensors, all characterized by the same address. This is why we decided to use two different I^2C lines: I^2C1 and I^2C2, and two different power supply lines from the microcontroller to communicate with the sensors. Another solution to this problem could have been to use an I2C multiplexer, but we don't have to much space on the PCB for to many components. In **Figure *5-10*** can also be seen the pull-up resistors R12, R13, R14, and R15 needed for the two I^2C communications. Moreover, in this figure, it can also be seen the decoupling capacitors C13, C14, C15, and C16 are placed near the power-up pin of each sensor.

On the other hand, since the magnetometer has a different address, it can communicate with the microcontroller via one of the existing I^2Cs; in the concrete case, we have chosen I^2C2. The capacitors C21 and C22, placed near the magnetometer's power supply pin, are used to decouple low-frequency noise and high-frequency noise, respectively.

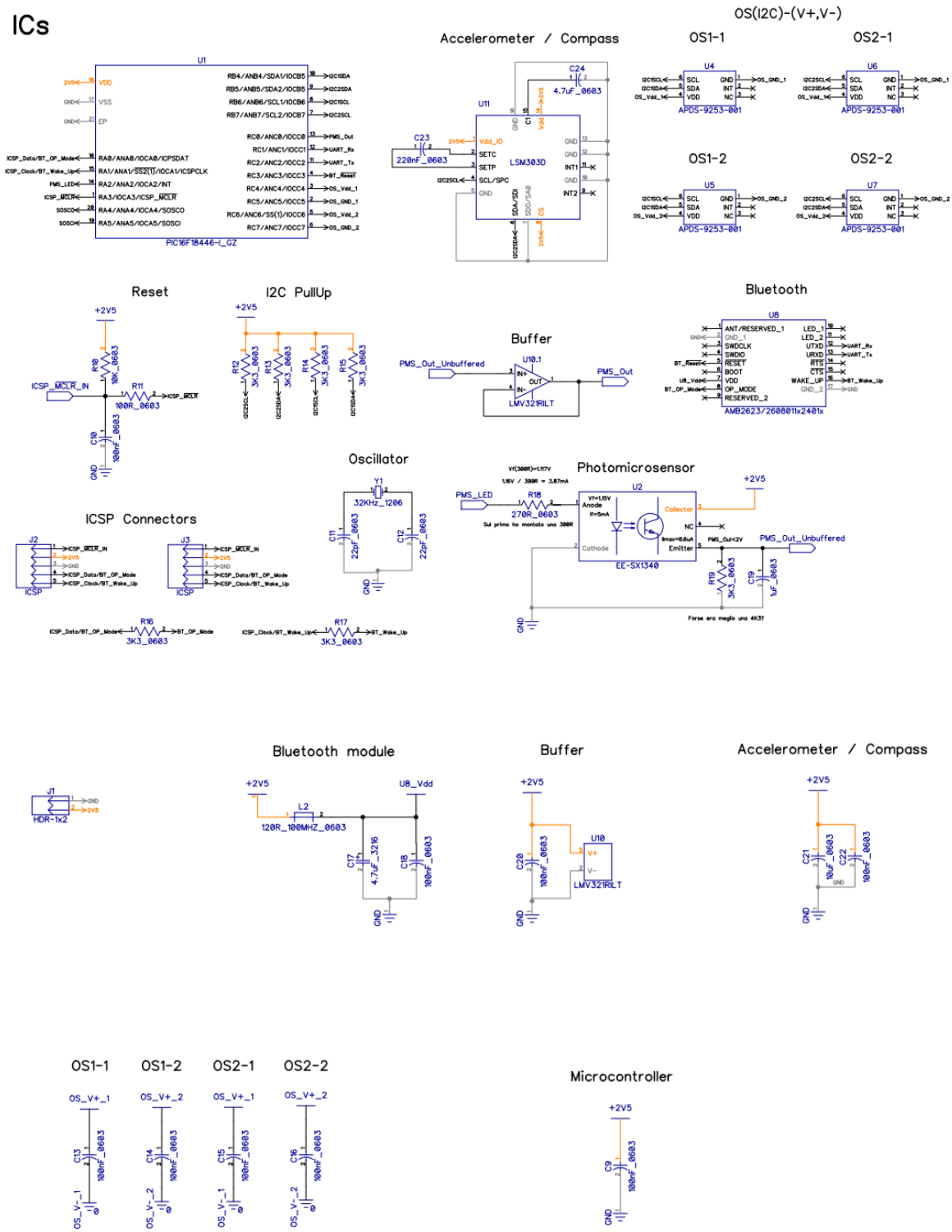

Figure 5-10: *Schematic circuit of the main board of FloSen*

Regarding the photo microsensor, a PWM signal with adjustable frequency is used to power up the LED. To sense the current flowing in the circuit of the LED, we placed a low-value resistor R18 near its anode. In the output of the photo microsensor, we have set the resistor R19 to sense the output voltage and the capacitor C19 to rectify the voltage since we are using a PWM signal for the LED. We will read the voltage out of the photo microsensor via the microcontroller's ADC. But the input impedance of the ADC is very small, equal to 10 KΩ, which being connected in parallel with R19 (on the other hand, both are in series with the resistor of the phototransistor) would decrease the output voltage. So, this way, the voltage measurement wouldn't be accurate. This is why the output voltage of the photo microsensor is firstly connected to a voltage follower, characterized by a very high input impedance, and then is sent to the microcontroller's ADC pin.
The Bluetooth module communicates with the microcontroller via the UART protocol. It is powered up directly from the microcontroller, and near the power supply input pin, two decoupling capacitors are placed to filter the low and high-frequency noise. Meanwhile, an inductor is also placed to smooth the changes in current.

5.3 The software

The software of FloSen was developed in **MPLAB X**, a freeware integrated development environment for the development of embedded applications on PIC. **MPLAB X** supports automatic code generation via the **MPLAB Code Configurator**, which was used in the first steps of the programming process to configure the microcontroller's inputs, outputs, and peripherals.
The peripherals of the microcontroller used in this software are *ADCC, EUSART1, FVR, MEMORY, PWM6, TMR0,* and *TMR1.* Indeed, the first line of the main function is related to the system initialization, i.e., the initialization of the microcontroller's peripherals. Next, since we will need interrupts to wake up the microcontroller and other peripherals from sleep, we enable the global and peripheral interrupts.
To outline, in the first place are taken 15 sets of measurements, one set each 4 seconds, by the optical sensors, photo microsensor, and the magnetometer embedded on the PCBs of FloSen. After that, the BT module is woken up. If it connects to the Evaluation Board, it sends out all the data measured so far; otherwise, after three failed attempts to connect, the BT module and the microcontroller are put to sleep for 5 minutes. Finally, after 5 minutes,

the microcontroller wakes up, and the BT module tries to connect. The BT module is sent to sleep temporarily if the connection doesn't fail. The measurement procedure starts from the beginning; otherwise, the BT module and the microcontroller are sent again to sleep for another 5 minutes.

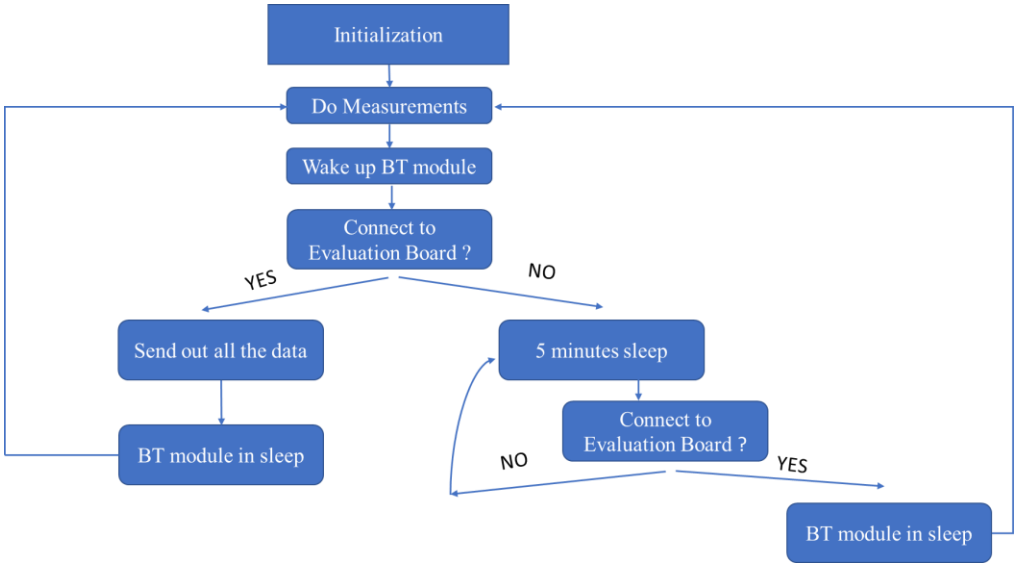

Figure 5-11: *Schematic of the steps carried out by the software written in MPLAB X*

Let's go more into details.

To reduce the board's power consumption, we aim to leave the BT module in sleep mode as much as possible. For this reason, every 4 s, we measure 70 quantities that correspond to the high and low part of the optical sensor data, magnetometer data, and photo microsensor. This way, every time we connect the BT module to the Evaluation Board, we send to the PC 15 vectors, each one containing 70 elements of 8 bits.

- Communication between the microcontroller and optical sensors

The microcontroller communicates with the optical sensors via the I^2C communication protocol. The speed of communication is set at 100 kHz. The prototype of the functions used to read data from the sensors and to write data to the sensors are respectively:

uint8_t ***I2C2Read*** *(uint8_t address, uint8_t *reg, uint8_t reg_len, uint8_t *data, uint8_t data_len);*
uint8_t ***I2C2Write*** *(uint8_t address, uint8_t *reg, uint8_t reg_len, uint8_t *data, uint8_t data_len);*

So, the information we need to provide are the sensor's address we want to interact with, the address of the register and the length of the register (in byte) we want to read or write to, and

the name and the length of the variable (in byte) where we need to write or read data from. The same communication protocol is also used to communicate the magnetometer with the microcontroller.

- Communication between the microcontroller and the BT module

The communication between the microcontroller and the BT module is handled by the serial communication interface (SCI) called Enhanced Universal Asynchronous Receiver Transmitter (EUSART). As mentioned earlier, EUSART is a peripheral of the microcontroller, and it was configured via the MCC. Since in this communication participates one master (the microcontroller) and one slave (the BT module), we choose the asynchronous mode and set the communication speed equal to 115200 baud, and the communication speed of the BT module is configured as 115200 baud.
The MCC generated file regarding EUSART, called eusart1.c is composed of several functions that we use in the main code of the FloSen, from which we can mention:

1. bool EUSART1_is_tx_ready(void);
2. bool EUSART1_is_rx_ready(void);
3. void EUSART1_Write(uint8_t txData);
4. uint8_t EUSART1_Read(void);

The output of the first function is a Boolean whose value is determined from a logical AND (&&) between the EUSART Transmit Interrupt Flag (TX1IF) bit of register PIR3 and the TXEN control bit of register TX1STA. TX1IF takes the value one if the EUSART transmit buffer contains at least one unoccupied space; meanwhile, it enables the transmission when TXEN is set to one. So, if the output is true, then EUSART1 is ready to write; otherwise, we should wait.
In the same way, the output of the second function is a Boolean whose value is determined from the value of the EUSART Receive Interrupt flag bit of register PIR3. When this bit has the value 1, the EUSART receive buffer is not empty, so EUSART1_Read() function can be used.
After sending a command to the BT module, we wait for its answer, which in some cases takes more time than in the other cases. As a result, the EUSART1_Read() function generated from the MCC was modified by introducing a timeout.

The microcontroller's commands to the BT module are predefined and can be divided into three groups: requests, confirmations, indications, and responses. The format of the commands is given in the table below:

Start signal	Command	Length	Payload	CS
0x02	1 Byte	2 Byte	Length Bytes	1 Byte

To this extent, when the microcontroller wants to send a message to the BT module via EUSART, the message should always start with the starting signal, 0x02. Then, the last element of the message should be 1 Byte which is calculated as a byte-wise XOR combination of all preceding Bytes, including the start signal.

- Measurements of the optical density from the micro photosensor

The Fixed Reference Voltage (FVR), the Analog to Digital Converter and the Pulse Width Modulator (PWM) are three peripherals of the microcontroller that are used to measure the data by the photo microsensor.

PWM6 is a scheme that provides power to the LED of the photo microsensor by switching quickly between fully ON and fully OFF states, so its signal is practically a square wave. Duty cycle is a term used to describe the amount of time the signal is ON / OFF, and it is expressed in percentage: 0 % fully OFF; 100 % fully ON. To specify the period of the PWM6, TIMER2 was used, which is an 8-bit timer. Another essential property of the PWM6 is the resolution, which determines the number of available duty cycles for a given period. For example, we have chosen a 9 – bit resolution, which results in 512 discrete duty cycles. The output of the photo microsensor will be a voltage (inverse proportional to the algal concentration) which will be sent to the ADC of the microcontroller that allows the conversion of this analog signal to a 12-bit binary representation. As a positive voltage reference to make the conversion, we chose FVR 1.024 V and VSS as a negative voltage reference. FVR is a stable voltage reference with selectable output levels: 1.024 V, 2.048 V, and 4.096 V.

To measure the photo microsensor’s output without saturating, we have written a simple function via which we change the duty cycle of the PWM6, depending on the concentration of the algal suspension.

5.4 The localization method

The most important feature of the FloSen sensor is that it is designed to float freely within a photobioreactor, and the measurements of the light intensity will be sent out via Bluetooth communication. It was also developed a localization method to localize the position of the sensor during the measurements.

A standard method to localize the magnetic field's position is based on a system composed of a three-axis magnetic field generated by three orthogonal coils and a three-axis sensor [147–149]. However, the use of several excitation coils requires a large amount of power [150]. Tadayon [150] instead, in the method that he developed, used a single-coil and two low-power sensors. He used an optimization algorithm to determine the position of the sensor. In all methods mentioned above, the AC signals are used to excite the magnetic field. Meanwhile, Shirai and Hashimoto [151] have developed a lateration-angulation hybrid method using a single anchor coil, DC magnetic field, and a MEMS sensor.

In the method developed during this thesis, we used three sequential anchor coils placed in parallel along the height of the PBR. The coils are exited using DC signals, and the magnetic field generated is measured via the MEMS magnetometer **(LSM303D).** This way, every point of the space inside the algal suspension is characterized by the spatial coordinates (ρ, Z) and the triplet of the magnetic field (B_1, B_2, B_3). We aimed to express $[\rho, Z] = f(B_1, B_2, B_3)$.

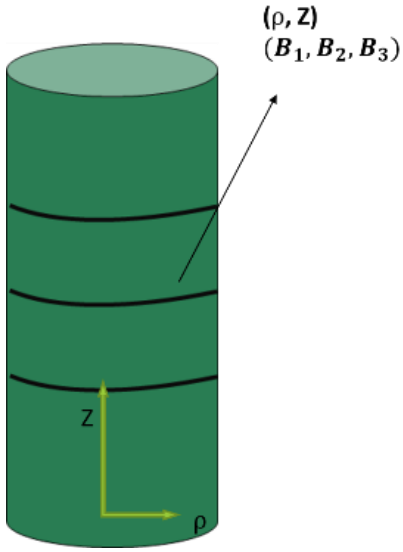

Figure 5-12: *Schematic representation of the three coils placed along the height of the PBR*

5.4.1 Analytical approach

The components of the magnetic field generated by a loop wire expressed in cartesian coordinates are given as below [152]:

$$B_x = \frac{C\ x\ z}{2\ \alpha^2\ \beta\ \rho^2}\ [\ (a^2 + r^2)E(k^2) - \alpha^2 K(k^2)] \quad 5\text{-}1$$

$$B_y = \frac{C\ y\ z}{2\ \alpha^2\ \beta\ \rho^2}\ [\ (a^2 + r^2)E(k^2) - \alpha^2 K(k^2)] \quad 5\text{-}2$$

$$B_z = \frac{C}{2\ \alpha^2\ \beta}\ [\ (a^2 - r^2)E(k^2) + \alpha^2 K(k^2)] \quad 5\text{-}3$$

Where, a is the radius of the coil, so it is constant, and:

$r^2 = x^2 + y^2 + z^2; \rho^2 = x^2 + y^2\ ; \alpha^2 = a^2 + r^2 - 2a\rho; \beta^2 = a^2 + r^2 + 2a\rho$

$k = 1 - \frac{\alpha^2}{\beta^2} = \frac{4\ a\ \rho}{(a+\rho)^2 + z^2}; C = \frac{\mu_0\ I}{\pi}$

$K(k)$ – the complete elliptic integral of the first kind

$E(k)$ – the complete elliptic integral of the second kind

Substituting the relations above in Equation 5-3, we may write the module of the magnetic field as a function of the ρ and z:

$$\mathrm{B}(\rho,\mathrm{z}) = \frac{C}{2\ \alpha^2\beta}\left\{\frac{z^2}{\rho^2}\ [(a^2 + \rho^2 + z^2)E(k) - ((a - \rho)^2 + z^2)K(k)]^2 + [(a^2 - \rho^2 - z^2)E(k) + ((a - \rho)^2 + z^2)K(k)]^2\right\}^{\frac{1}{2}} \quad 5\text{-}4$$

The algal solution will be confined in the region $0.15\ m \le \rho \le 0.2\ m$, of the photobioreactor. That's why we are interested in studying the magnetic field in that region. As a result, we are using a series expansion of the complete elliptic integrals at $k = 1$ [153].

$$K(k) \approx -\frac{1}{2} log(1-k)\left(1 - \frac{k-1}{4} + \frac{9}{64}\ (k-1)^2\right) + log(4) + \frac{1}{4}\ (1 - log(4))(k-1) + \frac{3}{128}\ (6\ log(4) - 7)(k-1)^2 \quad 5\text{-}5$$

$$E(k) \approx 1 + \frac{k-1}{4}\left(-2\,log(4) + 1 + \frac{24\,log(2)-13}{16}(k-1) - \frac{3(5\,log(2)-3)}{16}(k-1)^2\right) + log(1-k)\frac{k-1}{4}\left(1 + \frac{3(1-k)}{8} + \frac{15}{64}(1-k)^2\right) \quad 5\text{-}6$$

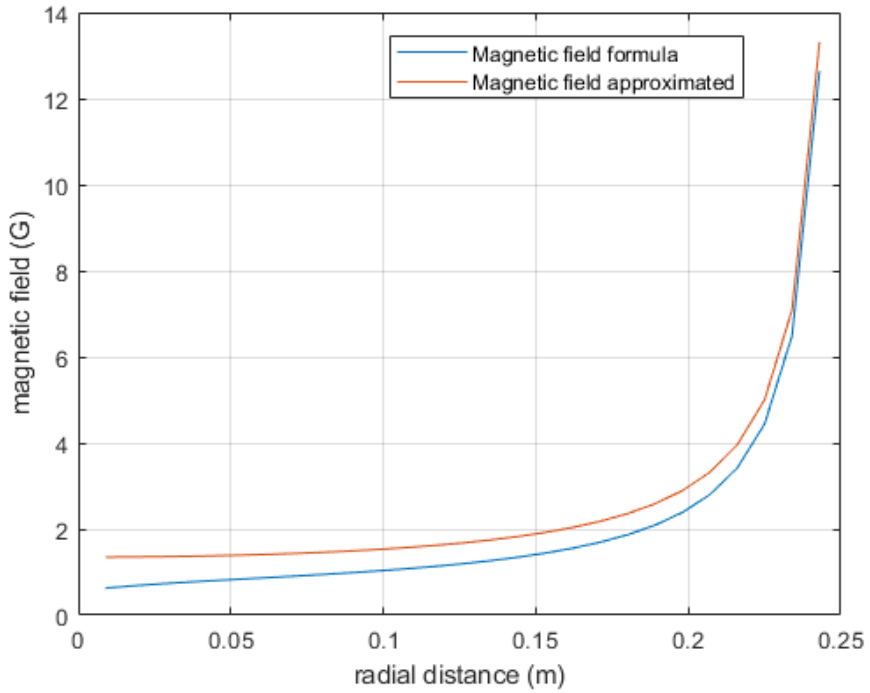

Figure 5-13: *The module of the magnetic field as a function of radial distance ρ, in the plane of the wire: calculated using the value of complete elliptic integrals provided by MATLAB (blue line); calculated using the Taylor expansion of the complete elliptic integrals at k = 1(red line).*

Further, we corrected the approximated magnetic field in the region $0.15\,m \leq \rho \leq 0.2\,m$, by introducing an offset to reduce the absolute error at a value smaller than ten mGauss. The range of accuracy of the sensor we are using is 20 mGauss.

The offset as a function of z was fitted in a polynomial of the third order:

$$\text{Ofs (z)} = 0.3509\,z^3 - 0.04642\,z^2 - 0.1046\,z + 0.01814 \quad 5\text{-}7$$

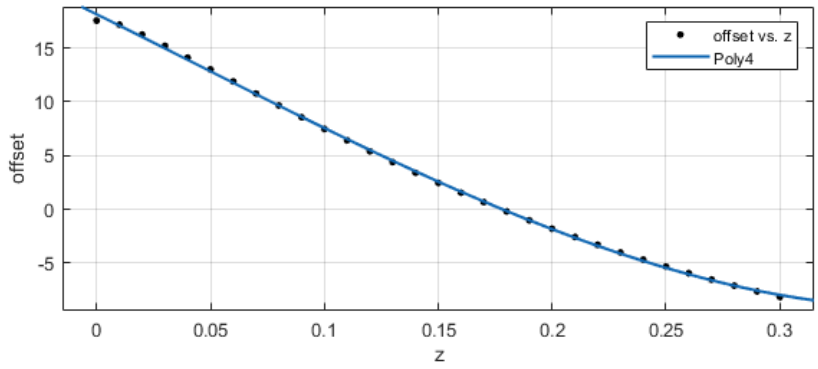

Figure 5-14: *The fitting of the offset as a function of the z*

As a result, the formula of the magnetic field as a function of (ρ, z), on which we are interested, is:

$$B(\rho,z) = \frac{C}{2\,\alpha^2\beta}\left\{\frac{z^2}{\rho^2}\left[(a^2+\rho^2+z^2)E(k) - ((a-\rho)^2+z^2)K(k)\right]^2 + \left[(a^2-\rho^2-z^2)E(k) + ((a-\rho)^2+z^2)K(k)\right]^2\right\}^{\frac{1}{2}} + 0.3509\,z^3 - 0.04642\,z^2 - 0.1046\,z + 0.01814 \quad \text{5-8}$$

Where K(k) and E(k) are given from equations 5-5 and 5-6, respectively, a is the radius of the wire, constant and $k = \frac{4\,a\,\rho}{(a+\rho)^2+z^2}$.

So, this way, we are describing every point (ρ, z) of the space by the modules:

$B_1 = f(\rho, z + z_1)$

$B_2 = f(\rho, z + z_2)$

$B_3 = f(\rho, z + z_3)$

Where, z_1, z_2, z_3 are constants that depend in the position of the coil along the height of the PBR.

Since it is not possible to calculate the inverse, $(\rho, z) = f^{-1}(B_1, B_2, B_3)$, in closed form. As a result, we focused on the fingerprint-based method, which estimates the position by finding the most similar data between the previously measured (or numerically calculated in our case) data with the data measured by the sensor.

5.4.2 Fingerprint-based method

To develop and test the localization method, we used a cylindrical tube to mock up the photobioreactor with the coils placed along its height. The cylinder has a height of 650 mm, an inner radius of 250 mm, and a width of 1.9 mm. The coils were constructed using a copper wire of diameter 0.8 mm. They are composed of 30 windings, placed in 3 layers with ten windings each. The radius of each layer of windings is: R_1 = 251.91 mm, R_2 = 252.81 mm, and R_3 = 253.71 mm. The coils are placed at a distance of 200 mm, between each other, along the height of the mock-up.

Figure 5-15: *The mock-up of the photobioreactor, with the coils place at a z = 0 mm (bottom coil), z = 200 mm (middle coil), z = 402 mm (upper coil).*

The magnetic field generated by a single coil was simulated within MATLAB, starting from an existing code that calculates numerically the magnetic field generated by a wire using the Biot-Savart law [154]. This code was modified based on the superposition principle.

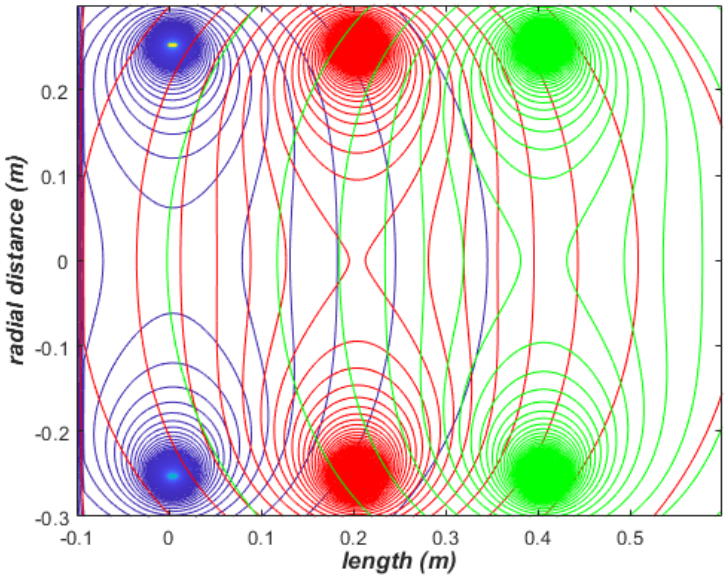

Figure 5-16: *The contour plot of the simulated magnetic field by the three coils.*

Every point (ρ, Z) inside the photobioreactor is characterized by the modules of the magnetic field and the Z components ($\boldsymbol{B_{1i}}, \boldsymbol{B_{2i}}, \boldsymbol{B_{3i}}, \boldsymbol{B_{z1i}}, \boldsymbol{B_{z2i}}, \boldsymbol{B_{z3i}}$). We have developed an algorithm to determine the position by comparing the magnetic field's calculated values with the magnetic field's measured value at a certain point within the photobioreactor.

Let's say the measured values at a certain point within the PBR are: ($\boldsymbol{B_{1m}}$, $\boldsymbol{B_{2m}}$, $\boldsymbol{B_{3m}}$, $\boldsymbol{B_{z1m}}$, $\boldsymbol{B_{z2m}}$, $\boldsymbol{B_{z3m}}$). Next, we calculate the Euclidian distances between the measured point and the calculated points, and after that, we search the position (ρ, Z), corresponding to the minimal Euclidian distance.

$$(\rho, Z) \xrightarrow{min} (\sqrt{(B_{1i} - B_{1m})^2 + (B_{2i} - B_{2m})^2 + (B_{3i} - B_{3m})^2 + (B_{z1i} - B_{z1m})^2 + (B_{z2i} - B_{z2m})^2 + (B_{z3i} - B_{z3m})^2})$$

5.4.3 Evaluation of expected error in position determination

Before being tested in real conditions, the method for determining the sensor's position was simulated to evaluate the expected error in position determination.

First, we simulated within MATLAB software the magnetic field generated by each coil placed in different positions: z = 0 mm, z = 200 mm, and z = 402 mm along the height of the mock-up (**Figure *5-15***). Then, the magnetic field values are calculated at every point of the space of the PBR having a radius 150 mm < R < 250 mm and height 0 < H < 410 mm, moving with steps of 0.9 mm. This way, we generated six matrixes: B_1, B_2, B_3, B_{1z}, B_{2z}, and B_{3z}, containing the module of the magnetic field and the Z component of the magnetic field generated from each coil.

In the next step, we generated a pair (y,z), whose value is chosen randomly from the domain of indexes of B_1 (B_2, B_3, B_{z1}, B_{z2}, B_{z3},). Let's call the point (y,z) starting point. For this randomly generated position, we find the corresponding values of the simulated magnetic field. Finally, we add an error with a gaussian distribution, characterized by an std of 20 mG and a mean of 0 mG. The values of magnetic field B_{r1}, B_{r2}, B_{r3}, B_{Zr1}, B_{Zr2}, and B_{Zr3} generated in this way represent the experimental values of the magnetic field.

For each randomly generated value of the magnetic field, we calculated the Euclidean distance in the magnetic field space:

$$D = \sqrt{(B_1 - B_{1m})^2 + (B_2 - B_{2m})^2 + (B_3 - B_{3m})^2 + (B_{z1} - B_{z1m})^2 + (B_{z2} - B_{z2m})^2 + (B_{z3} - B_{z3m})^2} \quad 5\text{-}9$$

D – represents a matrix with the same dimensions as the B_1 (B_2, B_3, B_{z1}, B_{z2}, B_{z3}). The minimal value of D will correspond to the point in (B1, B2, B3, Bz1, Bz2, Bz3) space that is nearer to the randomly generated point (Br1, Br2, Br3, Bzr1, Bzr2, Bzr3).

Let's call the landing point the point (Y, Z) corresponding to set (B1, B2, B3, Bz1, Bz2, Bz3) that minimizes Euclidian distance D with the experimental points. Then, the error in

position determination will be equal to the absolute difference between the starting point and the landing point.

We simulated 20000 starting points and for each of them, we determined the landing point and the error in mm.

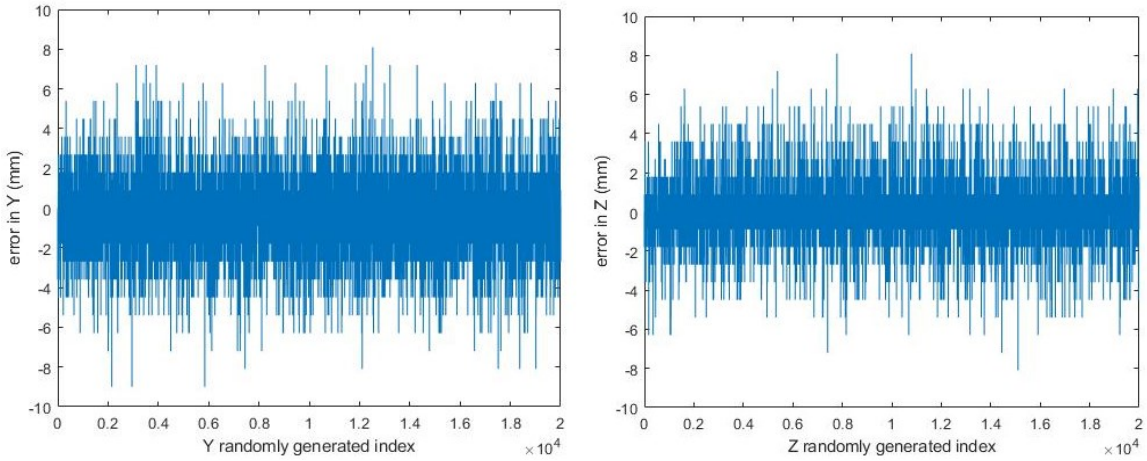

Figure 5-17: *Error in the radial direction of the PBR (left); Error along the height of the PBR (right)*

Figure ***5-17*** shows that this localization method forecasts the determination of the sensor's position with an error always smaller than 10 mm, as in the radial, so along the Z direction of the PBR.

Moreover, we called error starting points, the starting point for which the error in position determination was greater than 3 mm.

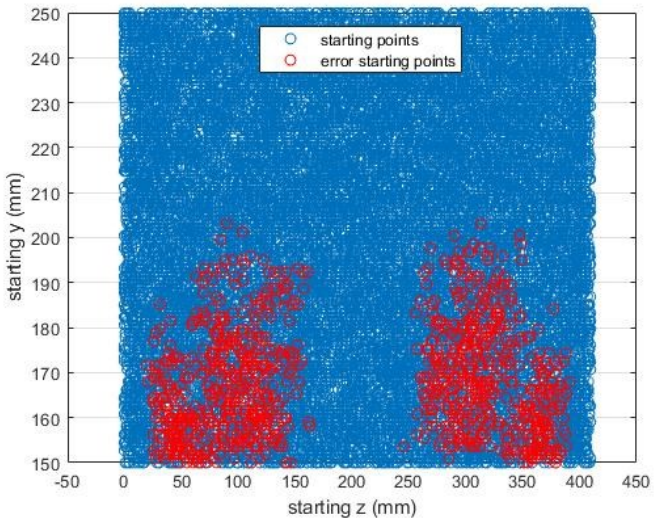

Figure 5-18*: Plot of the starting points (blue circles) and the error starting points (red circles)*

From ***Figure 5-18*** can be seen that in the region near to the central coil, at a height 150 < H < 250 mm, the error is always smaller or equal to 3 mm.

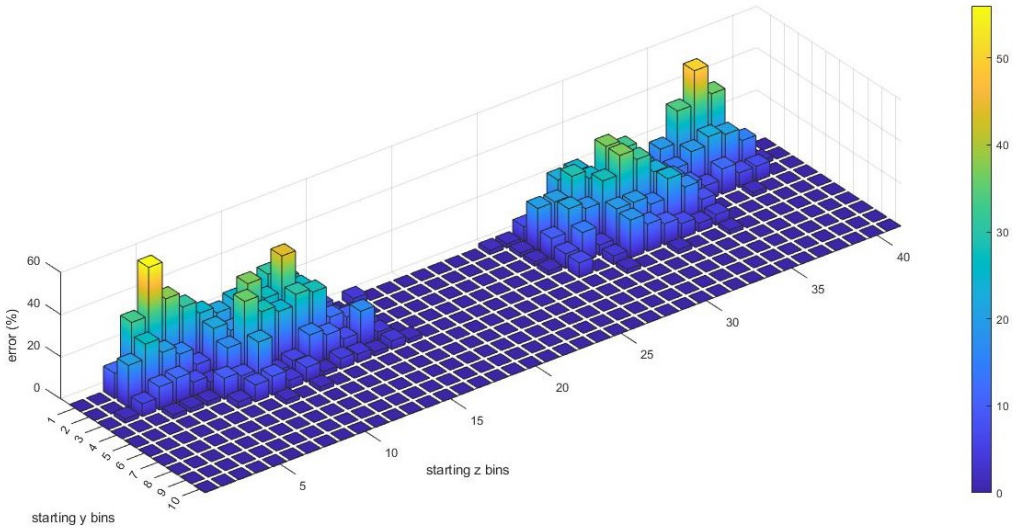

Figure 5-19: *Plot of the percentage of error starting points*

We divided the space where we calculated the magnetic field into bins of dimensions (10 x 10) mm, and for each bin, we calculated the percentage of the points with an error greater than 3 mm. As seen from the previous graph, the bins near the central coil are characterized by a 0 % error; meanwhile, few bins near external coils are characterized by an error up to 50 %. This is not a good result, and more work should be done to reduce the error.

5.5 Calibration of the photo microsensor

As stated in section 5.1.2, the photo microsensor operates at the wavelength of 940 nm. However, in a major part of the cases, the OD measurements to monitor the algal growth are taken at 750 nm outside PAR to avoid absorption from the pigments and, as a result, to consider only the scattering by the algal cell [117]. Therefore, since 940 nm is outside the PAR region, we propose this wavelength to monitor the algal growth, as it has also been used before by Yarnold to monitor biomass growth.

The first step in the calibration of the photo microsensor was determining the set-up time needed to measure reliable data. The integration time is the time during which the LED should be powered to have a constant output voltage. For this reason, we took several

measurements of the output voltage (measured by ADC), changing the integration time every time. The output voltage is constant when the ratio between the reading of the ADC (the output voltage in count) and the duty cycle remains constant.

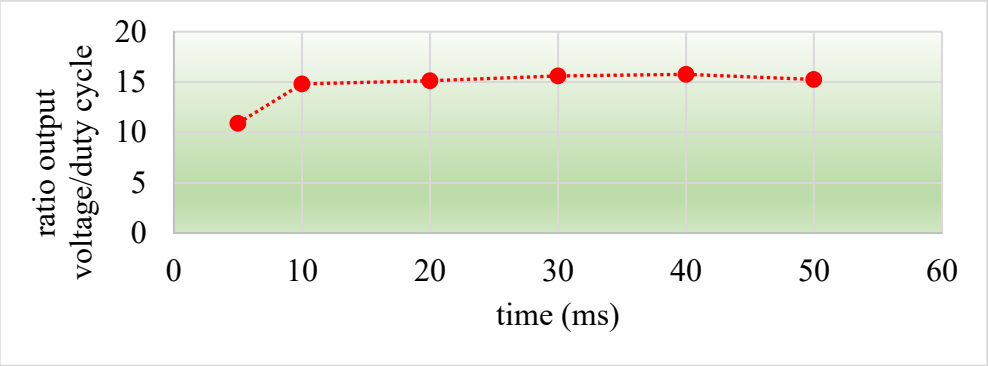

Figure 5-20: *Plot of the ratio between the output voltage (counts) and the duty cycle of the PWM6*

Figure 5-20 shows that starting from an integration time of 10 ms, the ratio between the output voltage (counts) and the duty cycle of the PWM6 can be considered constant. As a result, in future experiments, we set the integration time to 20 ms, as we wanted a value to be high enough to have accurate data, but at the same time, as small as possible to reduce the power consumption of the circuit.

The calibration of the photo microsensor was carried out after the sensor was encapsulated within the plastic case.

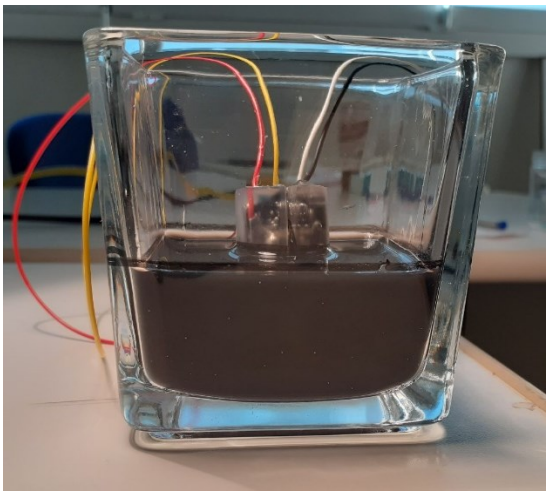

Figure 5-21: *Picture of the FloSen immersed inside the ink suspension. The wires seen in the picture are to check the measurement by the ADC, but they will be removed eventually.*

For this experiment, we used the suspension of different concentrations of black ink. The suspensions were prepared by diluting the ink in water. The optical density of these

suspensions was first measured using a spectrophotometer. And then, the data were compared with the optical density calculated from the photo microsensor's data. As a reference, in the measurements with the spectrophotometer was used water. The relation calculated the optical density using the photo microsensor:

$$OD = - \frac{log_{10} \left(\frac{V}{V_0}\right)}{d}, \qquad 5\text{-}10$$

V_0 is the output voltage of the photo microsensor when it is immersed in water. V is the output voltage of the photo microsensor when it is immersed in ink suspension and d (expressed in cm) is the gap, outside the case, between the emitter and the detector.

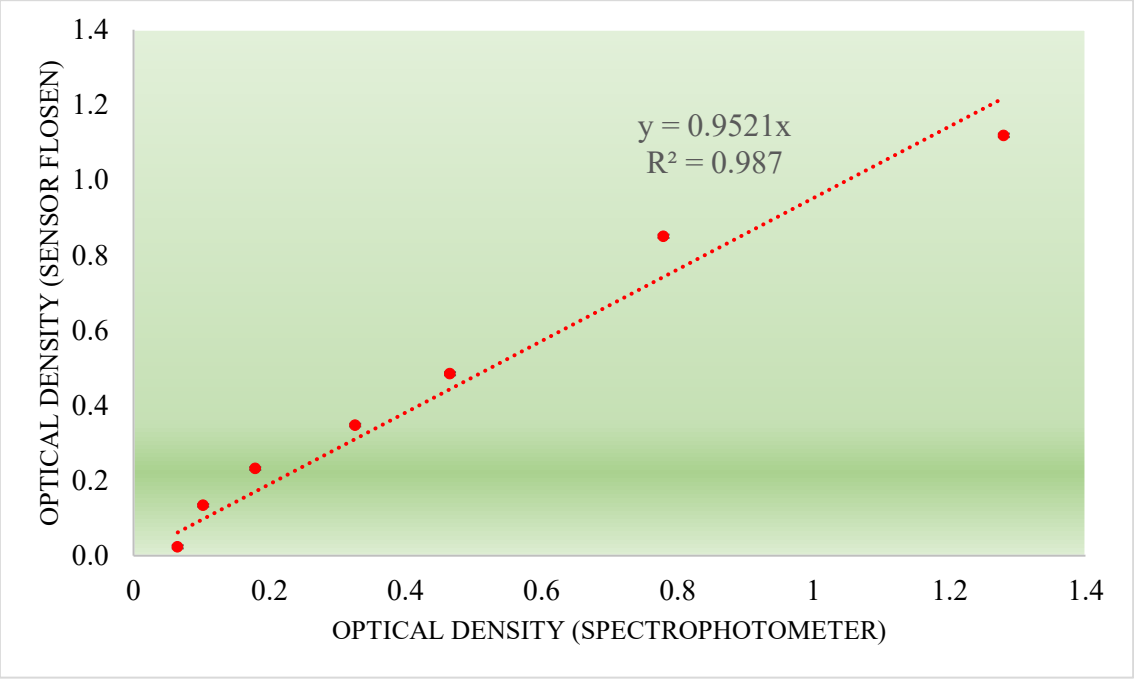

Figure 5-22: *Plot of the optical density OD measured with the sensor FloSen as a function of the optical density measured with the spectrophotometer*

Figure 5-22 shows that the slope of the regression line is 0.9521 and the Y-intercept is 0, so there is a linear relation between the OD values measured with the spectrophotometer and the values measured with FloSen. However, since the slope coefficient is not 1, a calibration of the sensor is needed before using it. It can be seen that the goodness of the fit, R^2, calculated as the sum of the squared deviations of the original data from the mean, is 0.987; the fit is good. The average error of the measured OD was 0.004.

5.6 Optical sensors measurements

The measurements in the experiment described in section 4.2.4 were carried out using the PAR sensor and the sensor FloSen. As a result, the transmitted power was calculated for all the three wavelengths of FloSen: 470 nm, 550 nm, and 610 nm. To this extent, the simulation was used in the function of our sensor, so we compared the transmitted power from the algal flask obtained from the simulation with the transmitted power measured with FloSen.

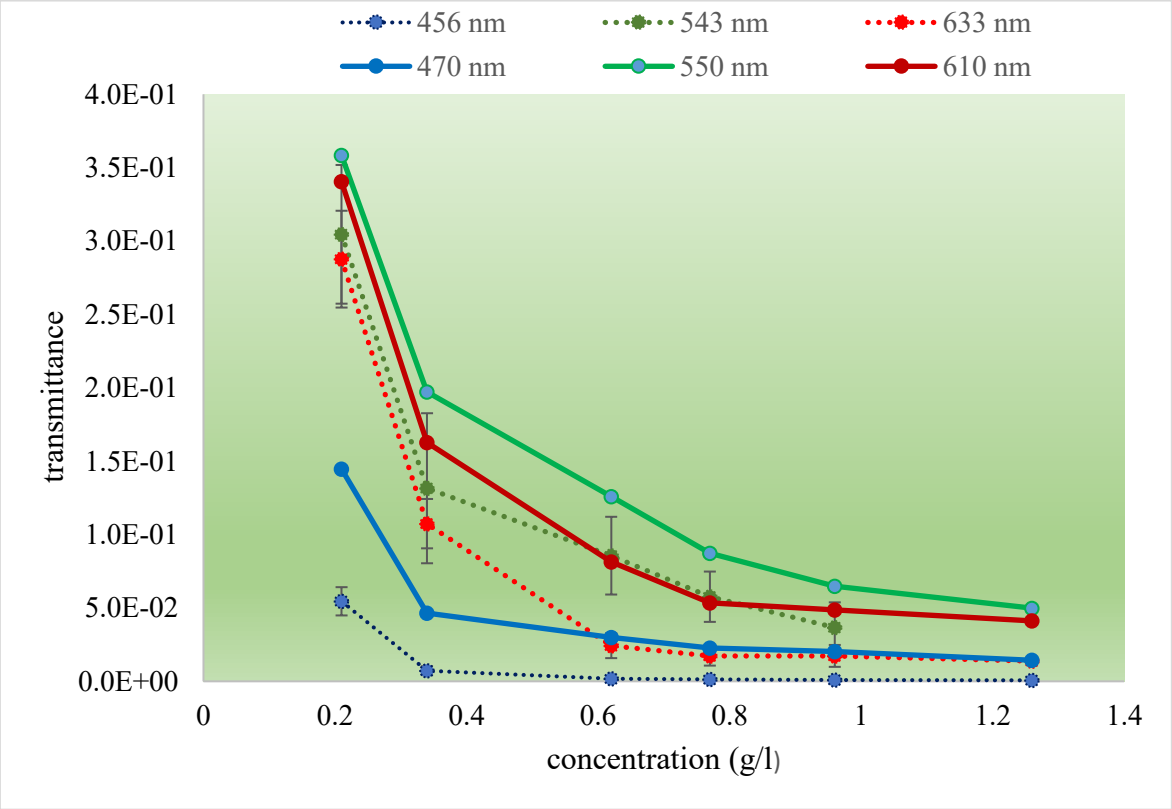

Figure 5-23: *Plot of the transmittance as a function of concentration obtained from the simulation (dashed lines) and from the measurements of FloSen (solid lines)*

Since the wavelengths we are comparing are not equal, there is some discrepancy between the simulated and measured data.

5.7 Localization algorithm data

Before testing the localization algorithm, the characterization of the magnetic field generated by each coil has been done. To this extent, the magnetic field generated by each coil along the height of the mock-up, at a constant distance from the center, has been measured by the MEMS sensor. Then, the data were calibrated via a calibration curve that was found using an optimization. So, the calibration curve has the form:

$$B_{corrected} = a\ x\ B^3_{measured} + b\ x\ B^2_{measured} + c\ x\ B^1_{measured} + d$$

Where, a = 0.000104, b = 0.018889, c = 0.941402 and d = 0.

In ***Figure 5-24*** is shown the plot of the magnetic field as a function of the height of the mock-up for the measured data via MEMS sensor and for the calculated data via MATLAB.

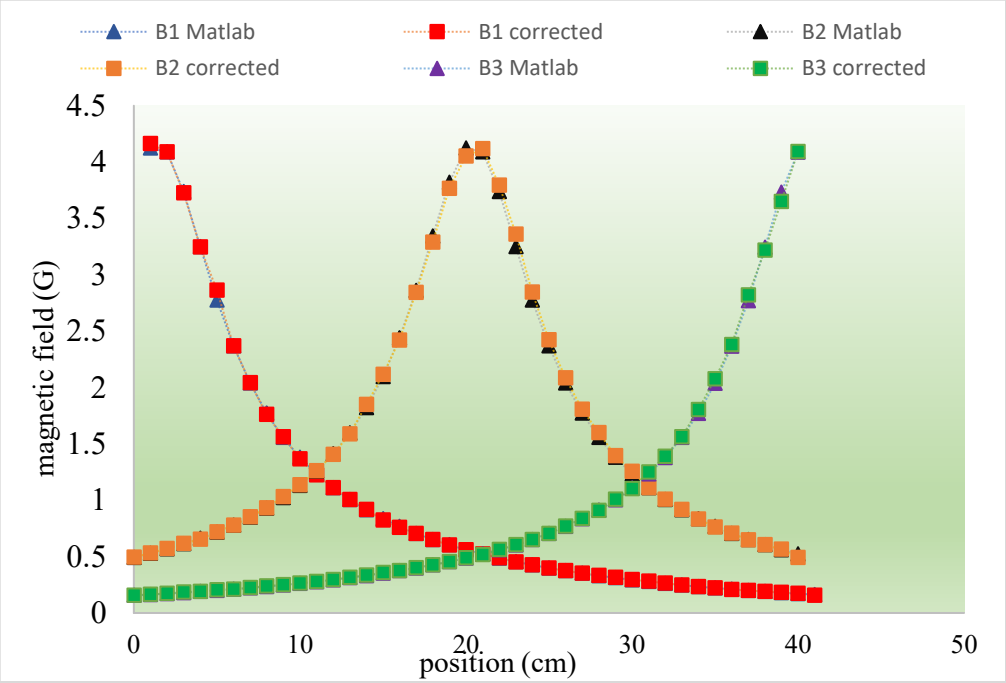

Figure 5-24: *Plot of the magnetic field as a function of the height of the mock – up at a radial distance of 0.2392 m*

To estimate the goodness of the measurements by the MEMS sensor, the relative error with respect to the simulated data via MATLAB was calculated. ***Figure 5-25*** shows that the relative error for a major part of the points is less than 2 %.

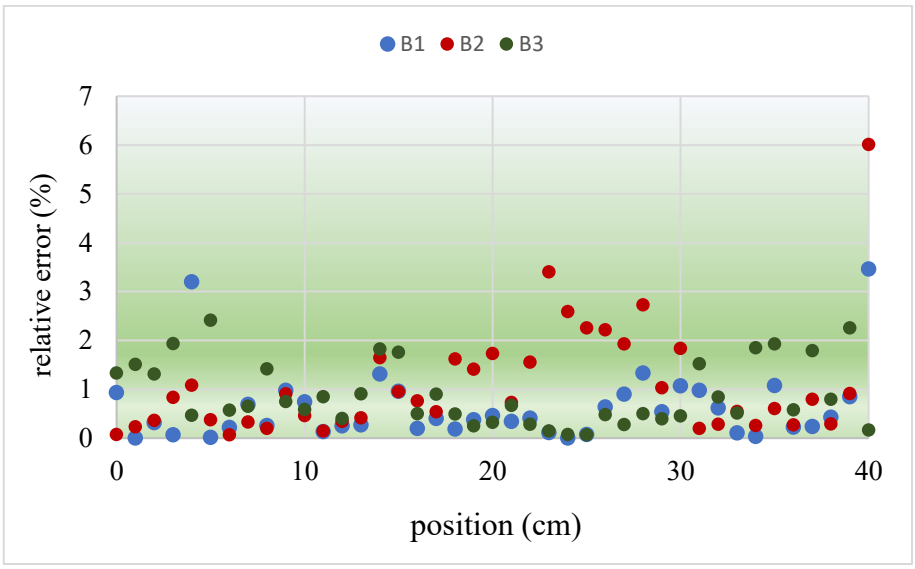

Figure 5-25: *Plot of the relative error of the magnetic field measured along the height of the mock–up*

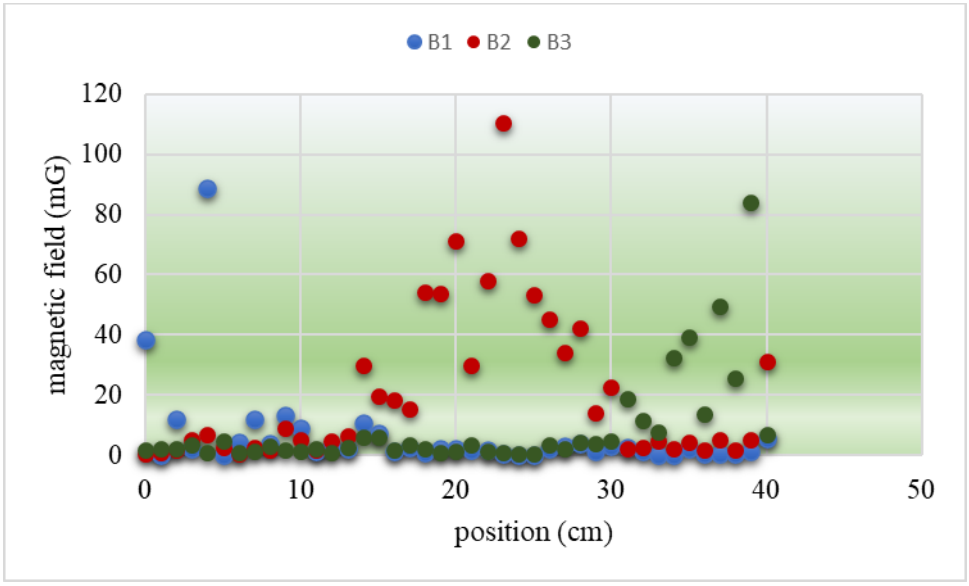

Figure 5-26: *Plot of the absolute error of the magnetic field measured with reference to the MATLAB generated values*

In ***Figure 5-26*** is plotted the absolute error of the measured magnetic field with reference to the calculated values via MATLAB as a function of the position. The magnetic field generated by the second coil is characterized by values greater than 20 mG. In the simulations carried out in Chapter 5, we accepted an error of less than 20 mG, according to which the position error would be less than 3 mm. So, from these measurements, we can say that the error in the position might be greater than 3 mm in some cases.

Conclusions

This thesis work was developed as part of a project aiming to optimize algal growth for large-scale CO_2 bio-fixation. The project was a collaboration between Biosyntex Srl, Eni spa, and the University of Ferrara.

In the framework of this project, we studied light distribution inside the photobioreactors (PBRs) and developed a model to simulate the spectral light distribution inside an algal suspension within the **OpticStudio ZEMAX** software.

One of the points highlighted during this project was the importance of monitoring the volumetric light distribution inside the algal suspension.

On the other hand, the study was also focused on the research to develop a floating sensor (FloSen) to measure the spectral irradiance of light inside the algal suspension.

The most important feature of this sensor is that it is designed to float freely inside the suspension, and its position will be determined via a localization method.

The method we studied to localize the sensor was based on measuring a non-uniform magnetic field generated by a set of coils powered by a DC. The sensor localization is carried out by an algorithm based on a map connecting the hyperspace of the magnetic field measured from every single coil and the physical position of the sensor within the photobioreactor. From the first set of measurements, the maximal error in the position determination was 1 cm. This result is promising as a first result, but more work needs to be done to reduce it to a value smaller than 3 mm.

The first prototype of the sensor (FloSen 1.0) has a cylindrical shape with a diameter equal to 24 mm and a height equal to 36.4 mm. The diameter of the PCB should be as small as possible (smaller than the actual value was not possible since there was no place to put all the components) because the gradient of the light intensity changes fast in the radial direction due to absorption from the algal suspension. FloSen is composed of two main boards connected with each other: the sensor's board and the power supply board.

On the power supply board is mounted a rechargeable Li-ion battery (LP301012 031012) with a capacity of 30mAh, four PV cells which will be used to recharge the battery, and a

Low-Dropout Linear Regulator (LDO) used to supply a constant voltage of 2.5 volts to the main board.

On the mainboard are mounted four optical sensors (two on each side), a photo microsensor, a magnetometer, a Bluetooth module (BT), and a microcontroller. We have placed two optical sensors on each side (at the corner of the board) for the same reason mentioned before: the gradient of the light intensity along the radial direction of the PBR is very high. Consequently, two sensors on each side would help measure and create a map of the light intensity distribution with smaller gridlines within the PBR. We are using the microcontroller (PIC16(L)F18446) as a signal processing and control unit. The optical sensors are digital RGB sensors (APDS-9253-001), which measure light intensity in four bands of the light spectrum centered at 470 nm, 550 nm, 610 nm, and 810 nm. We have chosen the first three wavelengths according to the absorption spectrum of the green microalgae. It is characterized by two peaks in the blue and red region and a minimum in the green region. The Bluetooth module (2608011024010_Proteus_II) provides a point–to–point communication between the sensor and a PC supervisor.

Meanwhile, the magnetometer (LSM303D) will measure the magnetic field and the acceleration. After we download the data, we analyze them within MATLAB software. To this extent, we will use the value of the output voltage saved from the photo microsensor to find the optical density of the algal suspension. Further, we will use the values of the magnetic field and acceleration within the localization algorithm to find the position of the sensor for each measurement of the light intensity from the optical sensors. We can create a map of the light distribution within the photobioreactor.

The software of FloSen 1.0 was developed in MPLAB X, which is a freeware integrated development environment for the development of embedded applications on PIC. After developing the software, we conducted different tests on the connection of the BT module, reconnection of the BT module, the lifespan of the battery, and reduction of the power consumption of the sensor. One of the results of these tests was related to the fact that communication via BT module was not possible when the sensor was within the suspension, at distances greater than 300 mm from the outer wall of the PBR, as the water absorbs in the band of 2.45 GHz, in which BT module works.

As a result, we have also designed the PCB of FloSen 2.0. We use a single PCB with dimensions (18x100) mm in this version. We needed to place the BT module and cells at the upper part of the sensor. This way, we can leave the BT module outside of the water, at the top of the PBR, and communication will be possible also when the sensor is deep within the

suspension. On the other hand, this way, the charging of the sensor can also be feasible as the incident light at the top of the PBR has a greater intensity with respect to the intensity within the suspension.

Moreover, the fact that the length of the sensor is 18 mm in the radial direction allows us to use only one sensor on each side of the PCB.

We have designed the next release of the floating sensor - FloSen 2.0 - to measure the battery's voltage and the charging current, which are significant quantities for the user to know during the operation of the sensor. Based on these quantities, the user can decide if the sensor is being charged within the reactor or if we need to take it outside and charge it. Further work needs to be done to develop FloSen 2.0 software and test the algorithm for the sensor localization within the algal suspension.

This work has applications also outside the bioreactors field. It can be used to monitor the physical quantities of the wastewater treatment process like temperature, turbidity and conductivity. Conductivity measurements are essential to monitoring the process of wastewater treatment as its changes are related to phosphorus and nitrogen removal [155].

Appendix

A. The code used to assess the error using the algorithm for the localization of the sensor.

```
clear all;
close all;
sigma = 0.020; %Gauss, used to introduce the randomly distributed error
max_B = 10;    %the maximum value of B measured by our sensor
zzz1 = 0;  %expressed in m; the starting position in the z direction
(along the height of the PBR), where the magnetic field is calculated
zzz2 = 0.41;   %expressed in m;
yyy1 = 0.15;% the region in y direction where I study the problem (m)
yyy2 = 0.25;% the region in y direction where I study the problem (m)
size_randi_z = 20000; % the number of randomly generated points
size_randi_y = 20000; % the number of randomly generated points


distance_greater = 3; % expressed in mm, the difference between the
starting point and the landing point

load('Ra_1_z0_0.mat')
load('Ra_2_z0_0.mat')
load('Ra_3_z0_0.mat')
s=0.0009;
yp(1:667) = -0.3:s:0.3; % Y-coordinates of the plane
zp(1:778) = -0.1:s:0.6;% Z-coordinates of the plane

% load the magnetic field created by the wire positioned at z = 0.222 m:
10 of
% radius Ra1, 10 of radius Ra2, 10 of radius Ra3
load('Ra_1_z0_2.mat')
load('Ra_2_z0_2.mat')
load('Ra_3_z0_2.mat')

% load the magnetic field created by the wire positioned at z = 0.424m:
10 of
% radius Ra1, 10 of radius Ra2, 10 of radius Ra3
load('Ra_1_z0_402.mat')
load('Ra_2_z0_402.mat')
load('Ra_3_z0_402.mat')

% Calculate the magnetic field generated by the wire of 30 turns at
% position z = 0
Bzero = BRa_1_z0_0 + BRa_2_z0_0 + BRa_3_z0_0;
% Calculate the magnetic field generated by the wire of 30 turns at
% position z = 0.222 m

Bzero_two = BRa_1_z0_2 + BRa_2_z0_2 + BRa_3_z0_2;
Bzero_four = BRa_1_z0_402 + BRa_2_z0_402 + BRa_3_z0_402;

BZzero_zero = BZRa_1_z0_0 + BZRa_2_z0_0 + BZRa_3_z0_0;
BZzero_two = BZRa_1_z0_2 + BZRa_2_z0_2 + BZRa_3_z0_2;
```

```
%BZzero_three = BZRa1_z0_3 + BZRa2_z0_3 + BZRa3_z0_3;
BZzero_four = BZRa_1_z0_402 + BZRa_2_z0_402 + BZRa_3_z0_402;
%BZzero_six = BZRa1_z0_6 + BZRa2_z0_6 + BZRa3_z0_6;

%BYzero_two = BYRa_1_z0_2 + BYRa_2_z0_2 + BYRa_3_z0_2;
%BYzero_three = BYRa1_z0_3 + BYRa2_z0_3 + BYRa3_z0_3;
%BYzero_four = BYRa_1_z0_4 + BYRa_2_z0_4 + BYRa_3_z0_4;
%BYzero_six = BYRa1_z0_6 + BYRa2_z0_6 + BYRa3_z0_6;

Br1 = zeros(1,size_randi_y);
Br2 = zeros(1,size_randi_y);
Br3 = zeros(1,size_randi_y);
minimum_distance = zeros(1,size_randi_y);
r_idx_minimum_distance = zeros(1,size_randi_y);
c_idx_minimum_distance = zeros(1,size_randi_y);

% Calculate the magnetic field generated by the wire of 30 turns at
% position z = 0
Bzero = BRa_1_z0_0 + BRa_2_z0_0 + BRa_3_z0_0;
% Calculate the magnetic field generated by the wire of 30 turns at
% position z = 0.3 m
%Bzero_three = BRa_1_z0_3 + BRa_2_z0_3 + BRa_3_z0_3;
% Calculate the magnetic field generated by the wire of 30 turns at
% position z = 0.6 m
%Bzero_six = BRa_1_z0_6 + BRa_2_z0_6 + B_Ra3_z0_6;
Bzero_two = BRa_1_z0_2 + BRa_2_z0_2 + BRa_3_z0_2;
Bzero_four = BRa_1_z0_402 + BRa_2_z0_402 + BRa_3_z0_402;
% I find the indexes in order to retrieve the magnetic field in space
% (r,z): ([0.15, 0.25], [0.009, 0.6])
BZzero_zero = BZRa_1_z0_0 + BZRa_2_z0_0 + BZRa_3_z0_0;
BZzero_two = BZRa_1_z0_2 + BZRa_2_z0_2 + BZRa_3_z0_2;
%BZzero_three = BZRa1_z0_3 + BZRa2_z0_3 + BZRa3_z0_3;
BZzero_four = BZRa_1_z0_402 + BZRa_2_z0_402 + BZRa_3_z0_402;

indzz = find(zp <= zzz1);
idz = indzz(end);
indzz2 = find(zp <= zzz2);
idz2 = indzz2(end);
indy1 = find(yp <= yyy1);
idy1 = indy1(end);
indy2 = find(yp <= yyy2);
idy2 = indy2(end);

%Find the magnetic field generated by the three coils B1 - the field
%generated by the coil positioned at z = 0 m, B2 - the field generated by
%the coil positioned at z = 0.3 m, B3 - the field generated by the coil
%positioned at z = 0.6 m.

B1 = Bzero(idy1:idy2,idz:idz2);
B2 = Bzero_two(idy1:idy2,idz:idz2);
B3 = Bzero_four(idy1:idy2,idz:idz2);
BZ1 = BZzero_zero(idy1:idy2,idz:idz2);
BZ2 = BZzero_two(idy1:idy2,idz:idz2);
BZ3 = BZzero_four(idy1:idy2,idz:idz2);
%BY1 = BYzero_zero(idy1:idy2,idz:idz2);
%BY2 = BYzero_three(idy1:idy2,idz:idz2);
%BY3 = BYzero_six(idy1:idy2,idz:idz2);
% the vector of the Y - axis (radial position), Z - axis (position along
% the height of the PBR
[mm,nn]=size(B1);
Y = yp(idy1:idy2);
```

```
Z = zp(idz:idz2);

% Randomly generate 100 values of the indexes of z position  and 100
values
% of the indexes of y position. z takes values from 1 to 657 because the
% indexes of Z vector are from 1 to 657 and the same for Y
z = randi([1 nn],size_randi_z,1);
y = randi([1 mm],size_randi_y,1);

% find B1,B2,B3 at the points y,z we generated randomly above and add a
% randam error of std = 3mG
%Find the minimal distance between magnetic field generated randomly and
%the magnetic field we have simulated
%Find the coordinates of B1,B2,B3 that have the minimal distance from
%Br1,Br2, Br3.
sig = 0.02;

x = linspace(-0.07,0.07,size_randi_y);

f=zeros(1,length(x));


for i = 1:size_randi_y

f(i) = (1/(sig*sqrt(2*pi)) .* exp(-((x(i))^2 / (2*(sig)^2))))/1000;

end

for i = 1:size_randi_y

    ra1 = randi(size(f));
    ra2 = randi(size(f));
    ra3 = randi(size(f));
    ra4 = randi(size(f));
    ra5 = randi(size(f));
    ra6 = randi(size(f));

        Br1(i)  = B1(y(i),z(i)) + f(ra1) ;
        Br2(i)  = B2(y(i),z(i)) + f(ra2);
        Br3(i)  = B3(y(i),z(i)) + f(ra3);
        BZr1(i) = BZ1(y(i),z(i)) + f(ra4);
        BZr2(i) = BZ2(y(i),z(i)) + f(ra5);
        BZr3(i) = BZ3(y(i),z(i)) + f(ra6);
        %BYr1(i) = BY1(y(i),z(i)) + (sigma*rand(1,1) );
        %BYr2(i) = BY2(y(i),z(i)) + (sigma*rand(1,1) );
        %BYr3(i) = BY3(y(i),z(i)) + (sigma*rand(1,1) );
        distance  = sqrt(((B1 - Br1(i)).^2 + (B2 - Br2(i)).^2 + (B3 -
Br3(i)).^2) + (BZ1 - BZr1(i)).^2 + (BZ2 - BZr2(i)).^2 + (BZ3 -
BZr3(i)).^2);
        minimum_distance(i) = min(distance(:));
        [r_idx_minimum_distance(i), c_idx_minimum_distance(i)] = find
(distance == minimum_distance(i));
end
% plot the difference between Y_landing and Y_starting.
figure(1)
plot((Y(r_idx_minimum_distance)-Y(y))*1000)
ylabel('difference between Y of the triple point and Y random (mm)')
xlabel('Y randomly generated index')
```

```
% plots the difference between Z_landing and Z_starting
figure(2)
plot((Z(c_idx_minimum_distance)- Z(z))*1000)
ylabel('difference between Z of the tripe point and Z random (mm)')
xlabel('Z randomly generated index')

% the position in YZ space of the starting point
starting_y = Y(y);
starting_z = Z(z);
% plot the position of starting z and starting y in YZ space expressed in
% mm
figure(3)
plot( starting_z*1000,starting_y*1000,'o')
xlabel('starting z (mm)')
ylabel('starting y (mm)')
grid on

%*-*-*-*-*-*-*-*-*-*-*-*-*-*-*-*-*-*-*-*-*-*-*-*-*-*-*-*-*-*-*-*-*-*-*-*-*-
*-*-*-*-*-*-*-*-*-*-*-*-*-*-*-*-
%*-*-*-*-*-*-*-*-*-*-*-*-*-*-*-*-*-*-*-*-*-*-*-*-*-*-*-*-*-*-*-*-*-*-*-*-*-
*-*-*-*-*-*-*-*-*-*-*-*-*-*-*-*-
%*-*-*-*-*-*-*-*-*-*-*-*-*-*-*-*-*-*-*-*-*-*-*-*-*-*-*-*-*-*-*-*-*-*-*-*-*-
*-*-*-*-*-*-*-*-*-*-*-*-*-*-*-*-


% 1. Find the difference between the landing point and the starting point
difference_Y = Y(r_idx_minimum_distance) - Y(y);
difference_Z = Z(r_idx_minimum_distance) - Z(y);
% 2. find the indexes of the difference vector at which the difference
between
% the landing and starting point is greater than distance_greater;
 idy_greater = find (abs(difference_Y)*1000 >= distance_greater);
 idz_greater = find (abs(difference_Z)*1000 >= distance_greater);
 % 3. Find the position of the starting Z and starting Y which are
 % charcterized by a difference greater than distance_greater with
respect
 % to landing z and landing y
 starting_y_greater = Y(y(idy_greater));
 starting_z_greater = Z(z(idz_greater));
 % the difference between starting and landing points at y and z found
 % above
 difference_Y_greater = difference_Y(idy_greater)*1000;
 difference_Z_greater = difference_Z(idy_greater)*1000;
 kk=size(starting_y_greater);
 kkk = size(starting_y);
 percentage_greater_distance = kk(1,2)/kkk(1,2) * 100;

% plot the position of the starting y and starting z in YZ space
expressed
% in mm and then plot with red circles the position of starting y and
% starting z that are charactrized by a difference with landing z and
% landing y greater than a certain variable called difference_greater

figure(4)
plot( starting_z*1000,starting_y*1000,'o')
hold on
plot( starting_z_greater*1000,starting_y_greater*1000,'or')
xlabel('starting z (mm)');
ylabel('starting y (mm)');
grid on
```

```
%*-*-*-*-*-*-*-*-*-*-*-*-*-*-*-*-*-*-*-*-*-*-*-*-*-*-*-*-*-*-*-*-*-*-*-*-
*-*-*-*-*-*-*-*-*-*-*-*-*-*-
%*-*-*-*-*-*-*-*-*-*-*-*-*-*-*-*-*-*-*-*-*-*-*-*-*-*-*-*-*-*-*-*-*-*-*-*-
*-*-*-*-*-*-*-*-*-*-*-*-*-*-
%*-*-*-*-*-*-*-*-*-*-*-*-*-*-*-*-*-*-*-*-*-*-*-*-*-*-*-*-*-*-*-*-*-*-*-*-
*-*-*-*-*-*-*-*-*-*-*-*-*-*-

%histogram of the starting y greater than distance_greater events per bin
figure(5)
YEdges = 0.15:0.01:yyy2;
counts = histogram(starting_y_greater, YEdges);
critical_points_y = counts.BinCounts;
xlabel('starting y (m)')
ylabel('number of error starting y per bin')
grid on

%histogram of the starting y events in each bin
figure (6)
counts = histogram(starting_y, YEdges);
starting_points_y = counts.BinCounts;
xlabel('starting y (m)')
ylabel('number of starting points y per bin')
grid on

%histogram of the percentage of starting y greater than the
distance_greater events
figure(7)
percentage_y = round((critical_points_y./starting_points_y)*100);
bar(percentage_y)
xlabel('starting y bins')
ylabel('(error y / starting y) per bin (%)')

%-0-0-0-0-0-0-0-0-0-0-0-0-0-0-0-0-0-0-0-0-0-0--0-0-0-0-0-0-0-0-0-0-0--0-
0-0-0-0-0-0-0-0-0-0--0-0-0-0-0-0-0-0-0-0-0--
%-0-0-0-0-0-0-0-0-0-0-0-0-0-0-0-0-0-0-0-0-0-0--0-0-0-0-0-0-0-0-0-0-0--0-
0-0-0-0-0-0-0-0-0-0--0-0-0-0-0-0-0-0-0-0-0--

%histogram of the starting z greater than distance_greater events per bin

figure(8)
ZEdges = (0:0.01:zzz2);
counts1 = histogram(starting_z_greater,ZEdges);
critical_points_z = counts1.Values;
xlabel('starting z (m)')
ylabel('number of error starting z per bin')
grid on

%histogram of the starting z per bin
figure(9)
counts2 = histogram(starting_z,ZEdges);
starting_points_z = counts2.Values;
xlabel('starting z (m)')
ylabel('number of starting z per bin')

percentage_z = round((critical_points_z./starting_points_z)*100);

figure(11)
bar(percentage_z);
xlabel('starting z bins')
ylabel('(error z / starting z) for each bin (%)')
```

```
grid on

%-0-0-0-0-0-0-0-0-0-0-0-0-0-0-0-0-0-0-0-0-0-0-0-0-0-0-0-0-0-0-0-0-0-0-0-
0-0-
%-0-0-0-0-0-0-0-0-0-0-0-0-0-0-0-0-0-0-0-0-0-0-0-0-0-0-0-0-0-0-0-0-0-0-0-
0-0-
%-0-0-0-0-0-0-0-0-0-0-0-0-0-0-0-0-0-0-0-0-0-0-0-0-0-0-0-0-0-0-0-0-0-0-0-
0-0-
%-0-0-0-0-0-0-0-0-0-0-0-0-0-0-0-0-0-0-0-0-0-0-0-0-0-0-0-0-0-0-0-0-0-0-0-
0-0-



%2d histogram of starting y and starting z events for each bin

figure(12)
N1 = histogram2(starting_y,starting_z, YEdges, ZEdges);
starting_yz = N1.Values;
xlabel('starting y (m)')
ylabel('starting z (m)')
zlabel('number of starting points per bin')



%2d histogram of error starting y and error starting z events for each
bin

figure(13)
N2 = histogram2(starting_y_greater,starting_z_greater, YEdges, ZEdges);
critical_yz = N2.Values;
xlabel('starting y (m)')
ylabel('starting z (m)')
zlabel('number of error points per bin')

%percentage of error starting y and starting z events per bin
percentage_yz = round((critical_yz./starting_yz)*100);

% 3d plot of error starting y and starting z events per bin
% bin 1 in y direction correspond of 0.15 m
% bin 10 corresponds to 0.25 m
figure(14)
b = bar3(percentage_yz);
xlabel('starting z bins ')
ylabel('starting y bins')
zlabel('error (%)')
grid on
for k = 1:length(b)
    zdata = b(k).ZData;
    b(k).CData = zdata;
    b(k).FaceColor = 'interp';
end

% Find the landing position (to have it) :)

landing_y = Y(r_idx_minimum_distance);
landing_z = Z(r_idx_minimum_distance);

% the values of the magnetic field at the starting points which are
% characterized by a greater difference than greater_distance with the
% landing points
starting_B1_greater=B1(y(idy_greater),z(idz_greater));
```

```
starting_B2_greater=B2(y(idy_greater),z(idz_greater));
starting_B3_greater=B3(y(idy_greater),z(idz_greater));
[iddy, iddz] = find (starting_B1_greater >= max_B | starting_B2_greater
>= max_B | starting_B3_greater >= max_B );
cc = size(Y(y(idy_greater(iddy))));
percentage_greater_distance_and_B = cc(1,2)/kkk(1,2) * 100;


starting_B1=B1(y,z);
starting_B2=B2(y,z);
starting_B3=B3(y,z);
[iddy_only, iddz_only] = find (starting_B1 >= 8 | starting_B2 >= 8 |
starting_B3 >= 8 );
cc_only = size(Y(y((iddy_only))));
ccc_only = size(Y(y));
percentage_greater_B = cc_only(1,2)/3*ccc_only(1,2) * 100;

figure(4)
hold on
plot(Z(z(idz_greater(iddz)))*1000,Y(y(idy_greater(iddy)))*1000,
'oblack');
legend('starting points','error starting points', 'error with module >
8G')
grid on
figure(10)
plot(Z(z((iddz_only)))*1000,Y(y((iddy_only)))*1000, 'om');
xlabel('starting z (mm)');
ylabel('starting y (mm)');
grid on
```

Acknowledgments

Would like to thank you dott.ssa E. C., S. P., and E. S. for giving light to the darkest period of my life so far, that happened to be these three years of the PhD.

Thank you also to prof. Donato Vincenzi for supervising my work.

Bibliography

1. IEA, *Global Energy and CO2 Status Report* (2019).
2. J. C. M. Pires, "COP21: The algae opportunity?," Renew. Sustain. Energy Rev. **79**, 867–877 (2017).
3. M. G. Saad, N. S. Dosoky, M. S. Zoromba, and H. M. Shafik, "Algal Biofuels: Current status and key challenges," Energies **12**, 1920 (2019).
4. M. Faried, M. Samer, E. Abdelsalam, R. S. Yousef, Y. A. Attia, and A. S. Ali, "Biodiesel production from microalgae: Processes, technologies and recent advancements," Renew. Sustain. Energy Rev. (2017).
5. A. Abbaszaadeh, B. Ghobadian, M. R. Omidkhah, and G. Najafi, "Current biodiesel production technologies: A comparative review," Energy Convers. Manag. 138–148 (2012).
6. T. L. Chew and S. Bhatia, "Catalytic processes towards the production of biofuels in palm oil and oil palm biomass-based biorefinery," Bioresour. Technol. **99**, 7911–7922 (2008).
7. I. M. Atadashi, M. K. Aroua, and A. Abdul Aziz, "Biodiesel seperation and purification: A review," Renew. Energy **36**, 437–443 (2011).
8. Priya, P. S. Deora, Y. Verma, R. A. Muhal, C. Goswami, and T. Singh, "Biofuels: An alternative to conventional fuel and energy source," Mater. Today Proc. (2021).
9. Y. A. Saddiki, M. Mofijur, P. S. Kumar, S. F. Ahmed, A. Inayat, F. Kusumo, I. A. Badruddin, T. M. Y. Khan, L. D. Nghiem, H. C. Ong, and T. M. I. Mahlia, "Microalgae biomass as a sustainable source for biofuel, biochemical and biobased value-added products: An integrated biorefinery concept," Fuel **307**, (2021).
10. N. S. M. Aron, K. S. Khoo, K. W. Chew, P. L. Show, W.-H. Chen, and T. H. P. Nguyen, "Sustainability of the four generations of biofuels – A review," Int. J. Energy Res. (2020).
11. C. R. Chilakamarry, A. M. M. Sakinah, and A. W. Zularisam, "Opportunities of biodiesel industry waste conversion into value-added products," Mater. Today Proc. (2021).
12. S. J. Judd, F. A. O. Al Momani, H. Znad, and A. M. D. Al Ketife, "The cost benefit of algal technology for combined CO2 mitigation and nutrient abatement," Renew. Sustain. Energy Rev. **71**, 379–387 (2017).
13. Y. Chisti, "Biodiesel from microalgae," Biotechnol. Adv. **25**, 294–306 (2007).
14. J.-S. Chang, T. C. Ling, S. P. Loke, and C.-Y. Chen, "Photobioreactors," in *Current Developments in Biotechnology and Bioengineering*, First (Elsevier, 2017), pp. 313–352.
15. M. Janssen, J. Tramper, L. Mur R, and R. H. Wijffels, "Enclosed Outdoor Photobioreactors: Light Regime, Photosynthetic Efficiency, Scale-up and Future Prospects," Biotechnol. Bioeng. **81**, 193–210 (2003).
16. C. Posten, "Design principles of photo-bioreactors for cultivation of microalgae," Eng. Life Sci. **9**, 165–177 (2009).
17. C.-G. Lee and B. Palsson, "High-Density Algal Photobioreactors Using Light-Emitting Diodes," Biotechnol. Adv. **44**, 1161–1167 (1994).
18. S. Baer, M. Heining, P. Schwerna, R. Buchholz, and H. Hübner, "Optimization of spectral light quality for growth and product formation in different microalgae using a continuous photobioreactor," Algal Res. **14**, 109–115 (2016).
19. A. Melis, "Photosystem-II damage and repair cycle in chloroplasts: what modulates the rate of photodamage in vivo?," Trends Plant Sci. **4**, 130–135 (1999).

20. C. Michael, M. del Ninno, M. Gross, and Z. Wen, "Use of wavelength-selective optical light filters for enhanced microalgal growth in different algal cultivation systems," Bioresour. Technol. **179**, 473–482 (2015).
21. M. Morita, Y. Watanabe, and H. Saiki, "Investigation of Photobioreactor Design for Enhancing the Photosynthetic Productivity of Microalgae," Biotechnol. Bioeng. **69**, 693–698 (2010).
22. L. Rammana, I. Rawat, and F. Bux, "Light enhancement strategies improve microalgal biomass productivity," Renew. Sustain. Energy Rev. **80**, 765–773 (2017).
23. C. Cho, K. Nam, Y. H. Seo, K. Kim, Y. Park, J.-I. Han, and J.-Y. Lee, "Study of optical configurations for multiple enhancement of microalgal biomass production," Sci. Rep. (2019).
24. E. G. Nwoba, D. A. Parlevliet, D. W. Laird, K. Alameh, and N. R. Moheimani, "Light management technologies for increasing algal photobioreactor efficiency," Algal Res. **39**, (2019).
25. A. P. Carvalho, S. O. Silva, J. M. Baptista, and F. X. Malcata, "Light requirements in microalgal photobioreactors: An overview of biophotonic aspects," Appl. Microbiol. Biotechnol. (2011).
26. G. A. Ifrim, M. Titica, L. Boillereaux, and S. Caraman, "Feedback linearizing control of light-to-microalgae ratio in artificially lighted photobioreactors," 12th IFAC Symp. Comput. Appl. Biotechnol. (2013).
27. C. L. Garzòn-Castro, J. A. Cortès-Romero, J. Arcos-Legarda, and E. Tello, "Optimal decision curve of light intensity to maximize the biomass concentration in a batch culture," Biochem. Eng. J. **123**, 57–65 (2017).
28. L. Pottier, J. Pruvost, J. Deremetz, J.-F. Cornet, J. Legrand, and C. G. Dussap, "A Fully Predictive Model for One-Dimensional Light Attenuation by Chlamydomonas reinhardtii in a Torus Photobioreactor," Biotechnol. Bioeng. **91**, (2005).
29. J. F. Cornet, C. G. Dussap, and G. Dubertret, "A Structured Model for Simulation of Cultures of the Cyanobacterium Spirulina platensis in Photobioreactors: I. Coupling Between Light Transfer and Growth Kinetics," Biotechnol. Bioeng. **40**, 817–825 (n.d.).
30. M. F. Modest, *Radiative Heat Transfer*, Second (Academic Press, 2003).
31. L. Pilon and R. Kandilian, "Interaction Between Light and Photosynthetic Microorganisms," Adv. Chem. Eng. **48**, 107–149 (2016).
32. L. Pilon, H. Berberoglu, and R. Kandilian, "Radiation transfer in photobiological carbon dioxide fixation and fuel production by microalgae," J. Quant. Spectrosc. Radiat. Transf. **112**, 2639–2660 (2011).
33. H. Berberoglu, L. Pilon, and A. Melis, "Radiation characteristics of Chlamydomonas reinhardtii CG125 and its truncated chlorophyll antenna transformants tla1, tlaX and tla1-CW+," Int. J. Hydrog. Energy **33**, 6467–6483 (2008).
34. R. Kandilian, A. Soulies, J. Pruvost, B. Rousseau, J. Legrand, and L. Pilon, "Simple method for measuring the spectral absorption cross-section of microalgae," Chem. Eng. Sci. **146**, 357–368 (2016).
35. E. Lee, R.-L. Heng, and L. Pilon, "Spectral optical properties of selected photosynthetic microalgae producing biofuels," J. Quant. Spectrosc. Radiat. Transf. **114**, 122–135 (2013).
36. L. Pottier, J. Pruvost, J. Deremetz, J.-F. Cornet, J. Legrand, and C. G. Dussap, "A Fully Predictive Model for One-Dimensional Light Attenuation by Chlamydomonas reinhardtii in a Torus Photobioreactor," Biotechnol. Bioeng. **91**, 570–582 (2005).
37. J. Dauchet, S. Blanco, and J. F. Cornet, "Calculation of the radiative properties of photosynthetic microorganisms," J. Quant. Spectrosc. Radiat. Transf. **161**, 60'84 (2015).
38. C. F. Bohren and D. R. Huffman, *Absorption and Scattering of Light by Small Particles* (John Wiley & Sons, 1998).

39. A. Quirantes and S. Bernard, "Light-scattering methods for modelling algal particles as a collection of coated and/or nonspherical scatterers," J. Quant. Spectrosc. Radiat. Transf. **100**, 315–324 (2006).
40. C. McHardy, G. Luzi, C. Lindenberger, J. R. Agudo, A. Delgado, and C. Rauh, "Numerical analysis of the effects of air on light distribution in a bubble column photobioreactor," Algal Res. **31**, 311–325 (2018).
41. M.-J. Li, Z.-X. Tong, Z.-J. Zhou, D. Huang, and R.-L. Wang, "A numerical model coupling bubble flow, light transfer, cell motion and growth kinetics for real timescale microalgae cultivation and its applications in flat plate photobioreactors," Algal Res. **44**, (2019).
42. C. McHardy, T. Horneber, and C. Rauh, "Spectral simulation of light propagation in participating media by using a lattice Boltzmann method for photons," Appl. Math. Comput. (2017).
43. C. McHardy, G. Luzi, J. R. Agudo, A. Delgado, and C. Rauh, "Hybrid Numerical Simulation of Fluid Flow and Light Distribution in a Bubble Column Photobioreactor," Photooptics 304–311 (2017).
44. B. Kong and R. D. Vigil, "Simulation of photosynthetically active radiation distribution in algal photobioreactors using a multidimensional spectral radiation model," Bioresour. Technol. **158**, 141–148 (2014).
45. J. M. Heinrich, I. Niizawa, F. A. Botta, A. R. Trombert, and H. A. Irazoqui, "Analysis and Design of Photobioreactors for Microalgae Production I: Method and Parameters for Radiation Field Simulation," Photochem. Photobiol. 938–951 (2012).
46. H. Berberoglu, J. Yin, and L. Pilon, "Light transfer in bubble sparged photobioreactors for H2 production and CO2 mitigation," Int. J. Hydrog. Energy 2273–2285 (2007).
47. L. G. Henyey and J. L. Greenstein, "DIFFUSE RADIATION IN THE GALAXY," Astrophys. J. **93**, 70–83 (1941).
48. C. Mobley and E. Boss, "Ocean Optics," http://www.oceanopticsbook.info/view/scattering/the_henyeygreenstein_phase_function.
49. H. Berberoglu, P. Gomez, and L. Pilon, "Radiation Characteristics of Botryococcus braunii, Chlorococcum littorale, and Chlorella sp. used for CO2 fixation and biofuel production," J. Quant. Spectrosc. Radiat. Transf. (2009).
50. R. Sayre, "Microalgae: The Potential for Carbon Capture," Bioscience **60**, (n.d.).
51. N. S. Lewis and D. G. Nocera, "Powering the planet: Chemical challenges in solar energy utilization," PNAS **104**, (2006).
52. D. S. Battisti and R. Naylor, "Historical Warnings of Future Food Insecurity with Unprecedented Seasonal Heat," Science **323**, (2009).
53. J. Pruvost and J.-F. Cornet, "10 Knowledge models for the engineering and optimization of photobioreactors," in *Microalgal Biotechnology: Potential and Production*, C. Posten and C. Walter, eds. (DE GRUYTER, 2012).
54. S. Aiba, "Growth kinetics of photosynthetic microorganisms," in *Microbial Reactions*, Advances in Biochemical Engineering/Biotechnology (Springer Berlin Heidelberg, 1982), Vol. 23, pp. 85–156.
55. J.-F. Cornet, C. G. Dussap, and J.-B. Gros, "Kinetics and energetics of photosynthetic micro-organisms in photobioreactors," in *Bioprocess and Algae Reactor Technology, Apoptosis*, Advances in Biochemical Engineering Biotechnology (Springer Berlin Heidelberg, 1998), Vol. 59, pp. 153–224.
56. J.-F. Cornet and C.-G. Dussap, "A Simple and reliable formula for assessment of maximum volumetric productivities in photobioreactors," Biotechnol. Prog. **25**, 424–435 (2009).
57. H. Takache, G. Christophe, J.-F. Cornet, and J. Pruvost, "Experimental and theoretical assessment of maximum productivities for the microalgae Chlamydomonas reinhardtii in two different geometries of photobioreactors," Biotechnol. Prog. NA-NA (2009).
58. J. Dauchet, S. Blanco, J.-F. Cornet, and R. Fournier, "Calculation of the radiative properties of photosynthetic microorganisms," J. Quant. Spectrosc. Radiat. Transf. **161**, 60–84 (2015).

59. M. D. Guiry, "How many species of algae are there?," Phycol. Soc. Am. (2012).
60. T. M. Mata, A. A. Martins, and N. S. Caetano, "Microalgae for biodiesel production and other applications: A review," Renew. Sustain. Energy Rev. **14**, 217–232 (2010).
61. A. Lehmuskero, M. S. Chauton, and T. Bostrom, "Light and photosynthetic microalgae: A review of cellular- and molecular- scale optical processes," Prog. Oceanogr. **168**, 43–56 (2018).
62. A. Richmond, *Handbook of Microalgal Culture: Biotechnology and Applied Phycology* (1988).
63. C. B. Field, M. J. Behrenveld, J. T. Randerson, and P. Falkowski, "Primary Production of the Biosphere: Integrating Terrestrial and Oceanic Components," Science **281**, (1998).
64. Y. Li, M. Horsman, B. Wang, N. Wu, and christopher Q. Lan, "Effects of nitrogen sources on cell growth and lipid accumulation of green alga Neochloris oleoabundans," Appl Microbiol Biotechnol **81**, (2008).
65. Y. Li, M. Horsman, N. Wu, C. Q. Lan, and N. Dubois-Calero, "Biofuels from Microalgae," Biotechnol. Prog. **0**, 0–0 (2008).
66. A. B. M. S. Hossain, A. Salleh, A. N. Boyce, P. chowdhury, and M. Naqiuddin, "Biodiesel Fuel Production from Algae as Renewable Energy," Am. J. Biochem. Biotechnol. **4**, 250–254 (2008).
67. Q. Hu, M. Sommerfeld, E. Jarvis, M. Ghirardi, M. Posewitz, M. Seibert, and A. Darzins, "Microalgal triacylglycerols as feedstocks for biofuel production: perspectives and advances," Plant J. **54**, 621–639 (2008).
68. L. Rodolfi, G. Chini Zittelli, N. Bassi, G. Padovani, N. Biondi, G. Bonini, and M. R. Tredici, "Microalgae for oil: Strain selection, induction of lipid synthesis and outdoor mass cultivation in a low-cost photobioreactor," Biotechnol. Bioeng. **102**, 100–112 (2009).
69. J. N. Rosenberg, G. A. Oyler, L. Wilkinson, and M. J. Betenbaugh, "A green light for engineered algae: redirecting metabolism to fuel a biotechnology revolution," Curr. Opin. Biotechnol. **19**, 430–436 (2008).
70. P. M. Schenk, S. R. Thomas-Hall, E. Stephens, U. C. Marx, J. H. Mussgnug, C. Posten, O. Kruse, and B. Hankamer, "Second Generation Biofuels: High-Efficiency Microalgae for Biodiesel Production," BioEnergy Res. **1**, 20–43 (2008).
71. K. Tsukahara and S. Sawayama, "Liquid Fuel Production Using Microalgae," J. Jpn. Pet. Inst. **48**, 251–259 (2005).
72. E. Stephens, I. L. Ross, Z. King, J. H. Mussgnug, O. Kruse, C. Posten, M. A. Borowitzka, and B. Hankamer, "An economic and technical evaluation of microalgal biofuels," Nat. Biotechnol. **28**, 126–128 (2010).
73. A. Melis, "Solar energy conversion efficiencies in photosynthesis: Minimizing the chlorophyll antennae to maximize efficiency," Plant Sci. **177**, 272–280 (2009).
74. P. T. Pienkos and A. Darzins, "The promise and challenges of microalgal-derived biofuels," Biofuels Bioprod. Biorefining **3**, 431–440 (2009).
75. K. M. Weyer, D. R. Bush, A. Darzins, and B. D. Willson, "Theoretical Maximum Algal Oil Production," BioEnergy Res. **3**, 204–213 (2010).
76. M. Packer, "Algal capture of carbon dioxide; biomass generation as a tool for greenhouse gas mitigation with reference to New Zealand energy strategy and policy," Energy Policy **37**, 3428–3437 (2009).
77. A. Bhowmik and L. Pilon, "Can spherical eukaryotic microalgae cells be treated as optically homogeneous?," J. Opt. Soc. Am. A **33**, 1495 (2016).
78. A. E. Solovchenko, "Physiological role of neutral lipid accumulation in eukaryotic microalgae under stresses," Russ. J. Plant Physiol. **59**, 167–176 (2012).
79. R. Razeghifard, ed., *Natural and Artificial Photosynthesis: Solar Power as an Energy Source* (Wiley, 2013).
80. J. J. Eaton-Rye, B. C. Tripathy, T. D. Sharkey, and Govindjee, eds., *Photosynthesis: Plastid Biology, Energy Conversion and Carbon Assimilation*, Advances in Photosynthesis and Respiration No. v. 34 (Springer, 2012).

81. M. Babin, C. S. Roesler, J. J. Cullen, and UNESCO, eds., *Real-Time Coastal Observing Systems for Marine Ecosystem Dynamics and Harmful Algal Blooms: Theory, Instrumentation and Modelling*, Oceanographic Methodology Series (UNESCO Publishing, 2008).
82. S. W. Jeffrey, S. W. Wright, and M. Zapata, "Microalgal classes and their signature pigments," in *Phytoplankton Pigments*, S. Roy, C. Llewellyn, E. S. Egeland, and G. Johnsen, eds. (Cambridge University Press, 2011), pp. 3–77.
83. H. Begum, F. MD. Yusoff, S. Banerjee, H. Khatoon, and M. Shariff, "Availability and Utilization of Pigments from Microalgae," Crit. Rev. Food Sci. Nutr. **56**, 2209–2222 (2016).
84. M. Huber, "Algae Research and Supply," Algae Res. Supply (n.d.).
85. T. Mirkovic, E. E. Ostroumov, J. M. Anna, R. van Grondelle, Govindjee, and G. D. Scholes, "Light Absorption and Energy Transfer in the Antenna Complexes of Photosynthetic Organisms," Chem. Rev. **117**, 249–293 (2017).
86. V. Vecchi, S. Barera, R. Bassi, and L. Dall'Osto, "Potential and Challenges of Improving Photosynthesis in Algae," Plants **9**, 67 (2020).
87. N. Nelson and C. F. Yocum, "STRUCTURE AND FUNCTION OF PHOTOSYSTEMS I AND II," Annu. Rev. Plant Biol. **57**, 521–565 (2006).
88. K. Maxwell and G. N. Johnson, "Chlorophyll fluorescence—a practical guide," J. Exp. Bot. **51**, 659–668 (2000).
89. M. Jonasz and G. R. Fournier, "Refractive indices and morphologies of aquatic particles," in *Light Scattering by Particles in Water* (Elsevier, 2007), pp. 447–558.
90. E. Aas, "Refractive index of phytoplankton derived from its metabolite composition," J. Plankton Res. **18**, 2223–2249 (1996).
91. Lord Rayleigh, "X. *On the electromagnetic theory of light*," Lond. Edinb. Dublin Philos. Mag. J. Sci. **12**, 81–101 (1881).
92. J. W. Strutt, "XV. *On the light from the sky, its polarization and colour*," Lond. Edinb. Dublin Philos. Mag. J. Sci. **41**, 107–120 (1871).
93. C. F. Bohren and D. R. Huffman, *Absorption and Scattering of Light by Small Particles* (Wiley-VCH, 2004).
94. H. C. van de Hulst, *Light Scattering by Small Particles.* (Dover Publications, 2012).
95. M. Kerker, *The Scattering of Light and Other Electromagnetic Radiation*, Physical Chemistry No. 16 (Academic Press, 1969).
96. C. R. Wylie and L. C. Barrett, *Advanced Engineering Mathematics*, 5th ed (McGraw-Hill, 1982).
97. W. Wiscombe, *Mie Scattering Calculations: Advances in Technique and Fast, Vector-Speed Computer Codes* (UCAR/NCAR, 1979), p. 3355 KB.
98. W. J. Wiscombe, "Improved Mie scattering algorithms," Appl. Opt. **19**, 1505 (1980).
99. G.-G. Siu and L. Cheng, "Mie solution of light scattering from spheres of radii up to 80λ with digit-array method," J. Opt. Soc. Am. B **19**, 1922 (2002).
100. H. Du, "Mie-scattering calculation," Appl. Opt. **43**, 1951 (2004).
101. R.-J. Zhu, J. Wang, and G.-F. Jin, "Mie scattering calculation by FDTD employing a modified Debye model for Gold material," Optik **116**, 419–422 (2005).
102. T. Grosges, A. Vial, and D. Barchiesi, "Models of near-field spectroscopic studies: comparison between Finite-Element and Finite-Difference methods," Opt. Express **13**, 8483 (2005).
103. A. L. Aden and M. Kerker, "Scattering of Electromagnetic Waves from Two Concentric Spheres," J. Appl. Phys. **22**, 1242–1246 (1951).
104. T. Kaiser and G. Schweiger, "Stable algorithm for the computation of Mie coefficients for scattered and transmitted fields of a coated sphere," Comput. Phys. **7**, 682 (1993).
105. L. Kai and P. Massoli, "Scattering of electromagnetic-plane waves by radially inhomogeneous spheres: a finely stratified sphere model," Appl. Opt. **33**, 501 (1994).
106. J. E. Hansen, "Exact and Approximate Solutions for Multiple Scattering by Cloudy and Hazy Planetary Atmospheres," J. Atmospheric Sci. **26**, 478–487 (1969).

107. V. M. Petnikova, V. V. Shuvalov, and E. V. Tret'akov, "Multiple-scattering Henyey-Greenstein phase function and fast path-integration," Proc. SPIE **6727**, (2007).
108. "Pfeiffer and Chapman - 2008 - Successive order, multiple scattering of two-term .pdf," (n.d.).
109. S. Johnsen and E. A. Widder, "The Physical Basis of Transparency in Biological Tissue: Ultrastructure and the Minimization of Light Scattering," J. Theor. Biol. **199**, 181–198 (1999).
110. A. Bricaud and A. Morel, "Light attenuation and scattering by phytoplanktonic cells: a theoretical modeling," Appl. Opt. **25**, 571–580 (1986).
111. M. Jonasz and Georges Fournier, *Light Scattering by Particles in Water: Theoretical and Experimental Foundations.* (Elsevier Science, 2011).
112. A. Bricaud, A.-L. Bédhomme, and A. Morel, "Optical properties of diverse phytoplanktonic species: experimental results and theoretical interpretation," J. Plankton Res. **10**, 851–873 (1988).
113. V. Lucarini, ed., *Kramers-Kronig Relations in Optical Materials Research*, Springer Series in Optical Sciences No. v. 110 (Springer, 2005).
114. H. Qi, Z.-Z. He, F.-Z. Zhao, and L.-M. Ruan, "Determination of the spectral complex refractive indices of microalgae cells by light reflectance-transmittance measurement," Int. J. Hydrog. Energy **41**, 4941–4956 (2016).
115. X. Li, L. H. Liu, and J. M. Zhao, "Optical extinction characteristics of three biofuel producing microalgae determined by an improved transmission method," Particuology (2017).
116. G. Johnsen, A. Bricaud, N. Nelson, B. B. Prézelin, and R. R. Bidigare, "In vivo bio-optical properties of phytoplankton pigments," in *Phytoplankton Pigments*, S. Roy, C. Llewellyn, E. S. Egeland, and G. Johnsen, eds. (Cambridge University Press, 2011), pp. 496–537.
117. M. Chioccioli, B. Hankamer, and I. L. Ross, "Flow Cytometry Pulse Width Data Enables Rapid and Sensitive Estimation of Biomass Dry Weight in the Microalgae Chlamydomonas reinhardtii and Chlorella vulgaris," PLoS ONE **9**, e97269 (2014).
118. H. R. Gordon and T. Du, "Light scattering by nonspherical particles: Application to coccoliths detached from Emiliania huxleyi," Limnol. Oceanogr. **46**, 1438–1454 (2001).
119. G. C. Pomraning, *The Equations of Radiation Hydrodynamics*, Dover ed., 1. publ., unabridged republ (Dover Publications, 2005).
120. A. Schuster, "Radiation Through a Foggy Atmosphere," Astrophys. J. **21**, 1 (1905).
121. E. A. Milne, "Thermodynamics of the Stars," in *Handbuch der Astrophysik*, G. Eberhard, A. Kohlschütter, H. Ludendorff, E. A. Milne, A. Pannekoek, S. Rosseland, and W. Westphal, eds. (Springer Berlin Heidelberg, 1930), pp. 65–255.
122. A. S. Eddington, *The Internal Constitution of the Stars*, Cambridge Science Classics (Cambridge University Press, 1988).
123. V. Kourganoff, *Basic Methods in Transfer Problems* (Dover Publications, 1963).
124. B. Davison, *Neutron Transport Theory* (Oxford University Press, 1958).
125. R. L. Murray, *Nuclear Reactor Physics* (Prentice Hall, 1957).
126. P. J. Coelho, "Discrete ordinates and finite volume methods," (n.d.).
127. J. R. Howell, M. P. Mengüç, and R. Siegel, *Thermal Radiation Heat Transfer*, Sixth edition (CRC Press, Taylor & Francis Group, 2016).
128. J. M. Heinrich, I. Niizawa, F. A. Botta, A. R. Trombert, and H. A. Irazoqui, "Analysis and Design of Photobioreactors for Microalgae Production I: Method and Parameters for Radiation Field Simulation: Photochemistry and Photobiology," Photochem. Photobiol. **88**, 938–951 (2012).
129. R. Kandilian, J. Pruvost, A. Artu, C. Lemasson, J. Legrand, and L. Pilon, "Comparison of experimentally and theoretically determined radiation characteristics of photosynthetic microorganisms," J. Quant. Spectrosc. Radiat. Transf. **175**, 30–45 (2016).
130. H. G. Weller, G. Tabor, H. Jasak, and C. Fureby, "A tensorial approach to computational continuum mechanics using object-oriented techniques," Comput. Phys. **12**, 620 (1998).

131. C. L. Teo, M. Atta, A. Bukhari, M. Taisir, A. M. Yusuf, and A. Idris, "Enhancing growth and lipid production of marine microalgae for biodiesel production via the use of different LED wavelengths," Bioresour. Technol. **162**, 38–44 (2014).
132. J. Malapascua, C. Jerez, M. Sergejevová, F. Figueroa, and J. Masojídek, "Photosynthesis monitoring to optimize growth of microalgal mass cultures: application of chlorophyll fluorescence techniques," Aquat. Biol. **22**, 123–140 (2014).
133. B. Tamburic, M. Szabó, N.-A. T. Tran, A. W. D. Larkum, D. J. Suggett, and P. J. Ralph, "Action spectra of oxygen production and chlorophyll a fluorescence in the green microalgae Nannochloropsis oculata.," Bioresour. Technol. **169**, 320–327 (2014).
134. M. Faried, M. Samer, E. Abdelsalam, R. S. Yousef, Y. A. Attia, and A. S. Ali, "Biodiesel production from microalgae: Processes, technologies and recent advancements," Renew. Sustain. Energy Rev. **79**, 893–913 (2017).
135. D. Sieg, "Making algae biodiesel at home," (n.d.).
136. B. Wang, C. Q. Lan, and M. Horsman, "Closed photobioreactors for production of microalgal biomasses," Biotechnol. Adv. **30**, 904–912 (2012).
137. K. Ojamae, "Growth physiology and photsynthetic performance of green microalgae mass culture grown in a thin -layer cascade," (2011).
138. *Zemax Optical Design Program, User's Manual* (2011).
139. M. Bass, G. Li, E. Van Stryland, C. M. DeCusatis, J. M. Enoch, V. Lakshminarayana, C. McDonald, and V. N. Mahajan, *Handbook of Optics*, Third (McGraw-Hill Companies, 2010), Vol. IV.
140. C. Y. Ma, J. M. Zhao, L. H. Liu, and L. Zhang, "Growth-dependent radiative properties of Chlorella vulgaris and its influence on prediction of light fluence rate in photobioreactor," J. Appl. Phycol. (2018).
141. R. Kandilian, E. Lee, and L. Pilon, "Radiation and optical properties of Nannochloropsis oculata grown under different irradiances and spectra," Bioresour. Technol. **137**, 63–73 (2013).
142. R. Emerson and C. M. Lewis, "The Dependence of the Quantum Yield of Chlorella Photosynthesis on Wavelength of Light," Am. J. Bot. **30**, (1943).
143. R. Christian Barbosa, J. Soares, and M. Arêdes Martins, "Low-cost and versatile sensor based on multi-wavelengths for real-time estimation of microalgal biomass concentration in open and closed cultivation systems," Comput. Electron. Agric. **176**, 105641 (2020).
144. B. T. Nguyen and B. E. Rittmann, "Low-cost optical sensor to automatically monitor and control biomass concentration in microalgal cultivation," Algal Res. **32**, 101–106 (2018).
145. Broadcom, *Digital RGB Sensor* (https://www.broadcom.com/products/optical-sensors/ambient-light-photo-sensors/apds-9253-001).
146. Omron, *Photomicrosensor (Transmissive) EE-SX1340* (https://omronfs.omron.com/en_US/ecb/products/pdf/en-ee_sx1340.pdf).
147. F. Raab, E. Blood, T. Steiner, and H. Jones, "Magnetic Position and Orientation Tracking System," IEEE Trans. Aerosp. Electron. Syst. **AES-15**, 709–718 (1979).
148. J. B. Kuipers, "SPASYN-an electromagnetic relative position and orientation tracking system," IEEE Trans. Instrum. Meas. **29**, 462–466 (1980).
149. C. Hu, S. Song, X. Wang, M. Q.-H. Meng, and B. Li, "A Novel Positioning and Orientation System Based on Three-Axis Magnetic Coils," IEEE Trans. Magn. **48**, 2211–2219 (2012).
150. P. Tadayon, G. Staude, and T. Felderhoff, "3D position estimation using a single coil and two magnetic field sensors," in *2015 37th Annual International Conference of the IEEE Engineering in Medicine and Biology Society (EMBC)* (IEEE, 2015), pp. 6712–6715.
151. R. Shirai and M. Hashimoto, "DC Magnetic Field Based 3D Localization With Single Anchor Coil," IEEE Sens. J. **20**, 3902–3913 (2020).
152. J. Simpson, J. Lane, C. Immer, and R. Youngquist, "Simple Analytic Expressions for the Magnetic Field of a Circular Current Loop," (2003).

153. Wolfram, "Introduction to EllipticE" WOLFRAM Res. (https://functions.wolfram.com/introductions/PDF/EllipticE.pdf).
154. S. Rao, "Magnetic field of a Circular current loop using Biot Savart's Law," (2020).
155. E. Levlin, "Conductivity measurements for controlling municipal wastewater treatment," Proc. Pol.-Swed.-Ukr. Semin. 51–62 (2010).